



HAL
open science

Anisotropic PCL electrospun scaffolds for soft tissue engineering: Elaboration, morphological and mechanical properties

Hugues Mondésert

► **To cite this version:**

Hugues Mondésert. Anisotropic PCL electrospun scaffolds for soft tissue engineering: Elaboration, morphological and mechanical properties. Material chemistry. Université Grenoble Alpes [2020-..], 2020. English. NNT: 2020GRALI011 . tel-02628521

HAL Id: tel-02628521

<https://theses.hal.science/tel-02628521v1>

Submitted on 26 May 2020

HAL is a multi-disciplinary open access archive for the deposit and dissemination of scientific research documents, whether they are published or not. The documents may come from teaching and research institutions in France or abroad, or from public or private research centers.

L'archive ouverte pluridisciplinaire **HAL**, est destinée au dépôt et à la diffusion de documents scientifiques de niveau recherche, publiés ou non, émanant des établissements d'enseignement et de recherche français ou étrangers, des laboratoires publics ou privés.

THÈSE

Pour obtenir le grade de

DOCTEUR DE L'UNIVERSITE GRENOBLE ALPES

Spécialité : 2MGE : Matériaux, Mécanique, Génie civil,
Electrochimie

Arrêté ministériel : 25 mai 2016

Présentée par

Hugues MONDÉSERT

Thèse dirigée par **Frédéric BOSSARD**, Professeur de
Universités, Université Grenoble Alpes
et codirigée par **Denis FAVIER**, Professeur des Universités,
Université Grenoble Alpes

préparée au sein du **Laboratoire Rhéologie et Procédés**
dans **l'École Doctorale I-MEP2 - Ingénierie - Matériaux,
Mécanique, Environnement, Energétique, Procédés,
Production**

**Élaboration par electrospinning et
caractérisation de scaffolds anisotropes de
polycaprolactone dédiés à l'ingénierie des tissus
mous**

**Anisotropic polycaprolactone electrospun
scaffolds for soft tissue engineering:
Elaboration, morphological and mechanical
properties**

Thèse soutenue publiquement le **10 Février 2020**,
devant le jury composé de :

Monsieur Daniel GRANDE

DR CNRS, Lab. ICMPE, Paris-Est (Président)

Madame Anne HÉBRAUD

MCF, Lab. ICPEES, Strasbourg (Rapporteur)

Monsieur Yves CHEMISKY

Professeur, Institut I2M, Bordeaux (Rapporteur)

Monsieur Claude VERDIER

DR CNRS, Lab. LIPhy, Grenoble Alpes (Examineur)

Monsieur Denis FAVIER

Professeur, Lab. TIMC-IMAG, Grenoble Alpes (Directeur de thèse)

Monsieur Frédéric BOSSARD

Professeur, Lab. Rhéologie et Procédés, Grenoble Alpes (Directeur de thèse)



Abstract

Tissue engineering technology requires porous biomaterials (scaffolds) which have to mimic as closely as possible the morphology and anisotropic mechanical properties of the native tissue to substitute. Electrospinning process is a promising technique to produce interconnected fibrous scaffolds with high porosity and surface-to-volume ratio that resemble extraordinarily to natural connective tissues. Anisotropic fibrous scaffolds fabricated by template-assisted electrospinning are investigated in this study. Fibers of electrospun Polycaprolactone (PCL) were successfully arranged spatially into honeycomb or square structures by using well-shaped 3D micro-architected metal collectors. Fibrous scaffolds present 2 to 4 mm wide patterns with low and high fiber density areas. Tensile test experiments were carried out to analyze mechanical behaviors of these new fibrous scaffolds. Honeycomb patterned mats showed significantly different mechanical properties along the two orthogonal axis directions probing the anisotropic character of the fabricated scaffolds. A finite element model was developed, based of simple geometries of the elementary patterns, in order to reproduce the experimental tensile measurements. Numerical approach has proved relationships between microstructure and mechanical behaviors of electrospun patterned scaffolds. This new versatile method to produce architected porous materials, adjustable to several polymers and structures, will provide appealing benefits for soft regenerative medicine application and the development of custom-made scaffolds.

Résumé

L'ingénierie tissulaire repose sur l'utilisation de biomatériaux poreux « scaffolds » pouvant imiter au plus proche les propriétés anisotropes des tissus du vivant. Le procédé d'électro-filage est une technique aujourd'hui bien connue pour élaborer des matériaux fibreux à grande porosité. Leurs propriétés caractéristiques (grand rapport surface/volume, inter-connectivité des pores) et leur forte ressemblance à la morphologie fibreuse des tissus biologiques font de ces matériaux un environnement idéalement attractif pour les cellules. Cette étude vise à produire par electrospinning des biomatériaux structurés dédiés à la reconstruction des tissus mous. Des membranes fibreuses à morphologies anisotropes ont été fabriquées par electrospinning. Les fibres de polycaprolactone (PCL) furent collectées avec succès sur des collecteurs microstructurés, formant une membrane architecturée avec des mailles en forme de nid d'abeille ou carrée. La caractérisation mécanique de ces membranes a mis en évidence des propriétés distinctes en fonction des directions d'élongation. Un modèle éléments finis a finalement été développé dans le but de reproduire les tests expérimentaux de traction. Partant d'une géométrie élémentaire simple afin de reconstruire la structure des scaffolds, les résultats numériques reflètent l'important caractère mécanique des membranes electrospinnées en lien avec leur microstructure.

Remerciements

C'est en temps de confinement que je trouve enfin le calme nécessaire à la rédaction de ces remerciements. Ces lignes ont été rédigées sereinement post soutenance, et seront les derniers mots pour clôturer ce mémoire de trois ans. Je dédie cet ouvrage à toutes ces personnes, qui ont animé et animé ma vie, ces personnes que j'ai rencontrées, aimées et avec qui j'ai tant partagées pendant ces dernières années.

J'exprime tout d'abord une profonde gratitude et mes sincères remerciements à ceux qui m'ont accompagné et guidé dans ce travail scientifique. Je remercie *Frédéric Bossard*, pour m'avoir ouvert les portes de ce projet, pour la confiance et l'écoute qu'il m'a accordé. Je remercie *Denis Favier*, pour avoir su me rediriger, me remotiver et donner un nouvel élan numérique à cette thèse. J'ai grandement apprécié ta simplicité, ta pédagogie, ton honnêteté scientifique et cet amour de l'aventure et des montagnes que je partage avec toi.

J'adresse mes sincères remerciements aux membres de mon jury : *Daniel Grande*, *Anne Hébraud*, *Yves Chemisky* et *Claude Verdier* qui ont accepté d'examiner, rapporter et évaluer mes travaux de thèse.

Je remercie très chaleureusement tous ceux qui m'ont aidé et accompagné au sein du laboratoire Rhéologie et Procédés. Je remercie *Mohamed Karrouch* pour son sérieux, sa gentillesse et les belles microstructures 3D conçues avec précision. Merci *Frédéric Hugenell*, pour ton soutien et ces longues discussions scientifiques et musicales. Merci pour toutes ces « jams » à la MINP, ces concerts, Frank Zappa et ces polyrythmies qui te font des nœuds au cerveau. Merci à ces journées vertes du laboratoire, à *Frédéric Pignon*, à *Jean-Robert Clermont* et leur interprétation si singulière de la bossa d'Ipanema. Je remercie généreusement Louise Infuso et Sylvie Garofalo pour leur disponibilité et leur enthousiasme journalier (et pour ces nombreuses recettes de cuisine du confinement). Je remercie également *Eric Faivre*, *Didier Blésès*, *Vincent Verdoot*, *Antoine Naillon* pour ces longs trails épuisants, *Denis Roux* pour sa bonne humeur et son engouement du sport, *Hélène Gaillard* pour ces précieux conseils de rhéométrie, *Guillaume Maitrejean* pour ses midis à espace vertical.

Je souhaite remercier particulièrement le bureau de l'ambiance, n°369 (je crois), où l'élite internationale du laboratoire de Rhéologie et Procédés a séjourné. Merci au « flemmard » *Ouattara*, pour tes retentissants soupirs, tes rires, tes moqueries et ce sourire du quotidien. Merci de m'avoir nommé successeur au poste de capitaine de la team « RhéoMaster », même si tu t'en es mordu les doigts par la suite. Merci *Djo Moctar*, roi de la danse, caïd africain, futur président du Sénégal. J'ai considérablement apprécié nos longues pauses café, où tu m'enseignais les rudiments Walof au soleil, et ces soirées de travail acharné à fuir l'alarme de 20h30. Merci *Pinto*, mon *David* qui m'a fait découvrir les festivités colorées de Grenoble, merci pour ces discussions intenses lors des interminables pauses café de l'après repas. Merci *Mohamad*, mon fidèle co-bureau d'en face, dont j'ai tant apprécié la sereine présence tout au long de ces trois ans. Merci *Medhi* pour ces derniers mois de partage du bureau, durant lesquelles tu as réussi extraordinairement à me divertir avec tes idées saugrenues. Merci à *Diego*, le « mec » qui aura dynamisé ma 3ème année de thèse, qui a ravivé le plaisir quotidien des pauses gourmandes, des guacamoles épicés, du Zacapa, qui a su me supporter quotidiennement

en période compliquée de rédaction, puis de confinement. Je ne te remercierai sans doute pas assez pour ta bonne humeur, ton entrain journalier, toujours prêt pour une petite excursion impossible en montagne. Ces nombreuses courses à se casser les genoux en Chartreuse ou Belledonne, à se geler les pieds dans la neige, à prendre nos selfies osés en haut de la montagne avant de commencer notre journée de travail au LRP. Merci *Louis*, pour m'avoir tenu compagnie scientifiquement, m'avoir transmis ta niaque et pour avoir partagé nos doutes sur la capricieuse machine d'électrospinning, tout en comparant la médiocrité de nos membranes structurés.

J'adresse mes sincères remerciements aux doctorants, postdoctorants du laboratoire: *Amélie, Alice, Mathilde, Adriana, William, Essa, Martinien et Justin Bieber, Héloïse, Anais, Antoine*. Merci *Ayoub* pour m'avoir, toujours au moment le plus opportun, tiré de force de mon écran en me jetant un jeton de café à la figure. Deuxième pensée particulière à *Clément (+Jenny)* et son rire communicatif et ses délicieux rhums arrangés.

Je tiens à remercier également mon deuxième laboratoire d'accueil, TIMC-imag, et toutes les personnes que j'ai côtoyées dans ce deuxième refuge scientifique. Merci à *Christopher Masri*, qui m'a accueilli à bras ouverts dans le petit bureau, qui m'a fait découvrir les joies de la simulation sous ANSYS et initié à « BlaBleBliBloBlu » LaTeX.

J'aimerais dédicacer cet ouvrage à ma famille. Cette belle famille que j'adore tant, qui a été présente du début à la fin de ma thèse. Merci à mes parents et mes deux frérots adorés. Merci *Maman* pour tout l'amour débordant que tu nous portes à nous trois, pour ta tendresse, ces couleurs vives, et cette constante préoccupation qui nous pousse à donner la meilleure version de nous-même. Merci *Papa*, pour ta générosité, ton amour et ta justesse, ton éducation, ta culture, ta curiosité, ainsi que ta colère du « matin sans café » que tu m'as transmise. Merci à *Greg*, pour notre jeunesse sportive, ta rigueur rythmique et ses longues parties de ping-pong. Tu resteras ma plus grande influence malgré nos belles différences. Je remercie mon petit grand frère *Étienne*, pour sa présence et soutien de tous les instants, pour avoir supporté mes humeurs, pour ces beaux moments partagés à Grenoble ou en Australie, pour ton beau caractère, tes convictions et ta culture considérable qui ne cesseront de me surprendre. A ma chère *Mémé*, de qui j'ai hérité bien des choses, de son caractère ou de sa passion des cartes. Merci d'être venue en personne à ma soutenance et d'avoir fait face à mon extrême pâleur. Merci à *Grand-mère* pour m'avoir soutenu, m'avoir conté les exploits de mon arrière-grand-père qui m'a légué son prénom et son gout de l'aventure.

De grands remerciements à mon entourage, mes connaissances et amis qui ont contribué sans probablement le savoir à l'aboutissement de ce projet de vie.

Merci à ces deux compagnons de vie, à ce grand fou de *Victor* et cet impertinent blondinet de *Sébastien*. Merci d'être toujours aussi c*, de me redonner le sourire rien qu'en regardant vos têtes ahuries ou en repensant à nos stupides aventures. Un grand merci pour m'avoir offert cette belle voie de calcaire sur les flancs de notre cher Crussol, où je vais pouvoir perfectionner ma technique des doigts. Merci à la *Candice*, merci pour tes abondantes œuvres d'art dessinés avec soin dans mon cahier de labo, tes rires si particuliers et communicatifs, ces grasses fondues du pays avec beaucoup trop d'ail, ce pliage intempestif de corde et pour tous ces nombreux moments de bonheur partagé tout au

long de ces trois années. Merci à *Gabriel* et *Cas*, pour ces road trips à la découverte des merveilles de l'étranger, ces pauses estivales qui ont été bien essentielles à l'obtention de mon diplôme. Merci *Samer*, pour ces mardi soirs à La Bobine, pour tous ces instants de partage et de rire. Je remercie aussi *Kevin* pour son assurance sans faille, le *Black Beat Blue Band* pour ces instants musicaux mémorables, *Alma* et *Marjolaine* pour cette magnifique coloc trop proche du Loco Mosquito, *Beata* et *Maciek* pour ces délicieuses vodkas, *Mariem* pour son chocolat qui va droit au cœur, les *Martins* et les *Ginves* pour ces éclats de rire effrénés.

J'aimerais enfin adresser une dernière et forte pensée envers la personne qui m'aura le plus soutenu. Je te remercie toi, je remercie Grenoble et cette thèse de nous avoir fait nous rencontrer, à ce doux soir d'Aperomix. L'adorable *Pescolina* qui m'a merveilleusement épaulé sur la fin capricieuse de thèse, qui a chassé de nombreux doutes et fait en sorte que "tout aille pour le mieux qu'il soit possible dans le meilleur des mondes". Merci *Elena*.

Contents

1. Electrospun materials for soft tissue regeneration applications. Elaboration techniques, morphological and mechanical properties.....	3
1.1. Tissue engineering and its scaffolds.....	3
1.1.1. Tissue engineering: a definition	3
1.1.2. Biological tissue in the human.....	4
1.1.3. PCL fibers as scaffolds for tissue engineering	5
1.2. Conventional electrospinning.....	9
1.2.1. Electrospinning in our time	9
1.2.2. Theory and set up.....	10
1.2.3. Electrospinning parameters	11
1.2.3.1. Solution parameters.....	11
1.2.3.2. Processing parameters	15
1.2.3.3. Environmental parameters.....	17
1.3. Structuration of fibrous materials in electrospinning	19
1.3.1. Self-assembling: Dimpled/ honeycomb membrane.....	19
1.3.2. Aligned fibers.....	20
1.3.2.1. Rotating collectors.....	20
1.3.2.2. Gap collectors or parallel plates.....	21
1.3.2.3. Centrifugal electrospinning	22
1.3.3. 3D templates	23
1.3.3.1. Grids/wire nets.....	23
1.3.3.2. Protrusion templates.....	25
1.4. Mechanical properties of electrospun membranes	28
1.4.1. Natural tissues.....	28
1.4.2. Random and aligned electrospun membranes	30
1.4.3. Patterned membranes	32
1.5. Conclusion.....	34
2. Structuration of electrospun PCL membranes for soft tissue engineering	35
2.1. Electrospinning.....	35
2.1.1. Polymer solution.....	35
2.1.2. Electrospinning Set up.....	36

2.1.3.	Characterization techniques.....	37
2.2.	Random fibers	37
2.3.	Aligned fibers	38
2.3.1.	Rotating collectors.....	38
2.3.2.	Average Fiber Diameter and degree of alignment	38
2.3.3.	Porosity assessment	40
2.4.	Structured membranes	42
2.4.1.	3D collectors.....	42
2.4.2.	Architected materials	43
2.4.2.1.	Honeycomb patterned scaffolds	43
2.4.2.2.	Square patterned scaffolds	48
2.4.2.3.	Other shaped scaffolds.....	51
2.5.	Conclusion.....	52
3.	Characterization of the mechanical behavior of electrospun architected scaffolds.....	53
3.1.	Tensile test Set-up	53
3.1.1.	Sample preparation.....	53
3.1.2.	Uni-axial tensile test equipment	56
3.1.3.	Local-deformation monitoring.....	57
3.1.4.	Determination of nominal Stress	58
3.1.4.1.	Difficulty to measure 3D membrane thickness	58
3.1.4.2.	Estimation of nominal stress	59
3.1.5.	Definition of global and local strains.....	60
3.2.	Preliminary tests	62
3.2.1.	Influence of the sample width.....	62
3.2.2.	Relaxation.....	63
3.2.3.	Cyclic tensile tests	65
3.3.	Mechanical behavior of scaffolds under monotonic tensile loading.....	68
3.3.1.	Raw, Random and Aligned scaffolds	68
3.3.2.	Honeycomb scaffolds	70
3.3.2.1.	Nominal stress assessment	70
3.3.2.2.	Local strains investigation	71
3.3.3.	Square scaffolds	73

3.3.3.1.	Nominal Stress assessment	73
3.3.3.2.	Local strains investigation	75
3.3.4.	Honeycomb batch B: where is anisotropy?.....	76
3.4.	Conclusion.....	78
4.	Modelling of mechanical behavior of structured scaffolds: a finite element approach.....	79
4.1.	Finite element mechanical model.....	79
4.1.1.	General approach.....	79
4.1.2.	Meshing.....	81
4.1.3.	Properties of constitutive materials.....	82
4.2.	Modelling of Honeycomb scaffolds.....	83
4.2.1.	Model 1: isotropic materials	83
4.2.1.1.	Global behavior	83
4.2.1.2.	Analysis of honeycomb sample in D_1 direction	84
4.2.1.3.	Analysis of honeycomb sample in D_2 direction	87
4.2.1.4.	Analysis of the local transversal cell deformation.....	88
4.2.2.	Model 2: orthotropy for aligned fibers zones	89
4.2.2.1.	Orthotropic model.....	89
4.2.2.2.	Global behavior	91
4.2.2.3.	Analysis of honeycomb sample in D_1 direction	92
4.2.2.4.	Analysis of honeycomb sample in D_2 direction	94
4.2.2.5.	Analysis of the local transversal cell deformation.....	94
4.2.3.	Conclusion	95
4.3.	Influence of electrospinning process on anisotropic behavior of honeycomb scaffolds ..	96
4.3.1.	New geometric model of honeycomb scaffolds.....	96
4.3.2.	Experimental validation.....	97
4.3.3.	Numerical model with fibers in the central zone.....	98
4.4.	Modelling of square scaffolds	99
4.4.1.	Geometric model.....	99
4.4.2.	Global behavior	100
4.4.3.	Global behaviors of square scaffolds without secondary bridges	103
4.4.4.	Analysis of the local transversal deformation of the cell	104
4.4.5.	Conclusion	105

4.5. Conclusion numerical simulation.....	105
5. General conclusion	107
6. References	109
7. List of figures.....	121
8. List of tables.....	127

General introduction

Progress in advanced material science and engineering has marked the beginning of the 21st century. Among different sciences, nanotechnology has taken the lead on the fabrication of novel materials with micro to nanometer scales conceiving smaller, lighter, tougher, smarter and cheaper materials. Elaboration of 3D structures made of polymer fibers has been developed intensely these last previous years. Nowadays, techniques to fabricate fibers such as drawing, template synthesis, phase separation or electrospinning have contributed to enlarge the panel of available nanoporous materials [1], [2]. Electrospinning is one of the most promising technique to shape scaffolds in terms of low cost, simplicity and versatility of the process. Membrane science made by electrospinning has reached a recent peak of activities due to the plethora of trendy applications that offers the technology such as textile protection, hi-tech clothes, cosmetics, packaging, sensors, filtration, fuel cell batteries, drug delivery and tissue engineering. Industrial market has been developed incredibly with creation of diverse companies specialized in electrospinning in and outside Europe (*IME-Netherlands, Bioinicia-Spain, Inocure-Czech Republic, TongLiTech-China, Electropunra-Singapore, eSPin-USA*).

Such interest is driven by the extraordinary properties of electrospun membranes. They offer superior mechanical properties compared to the bulk such as high porosity, high surface-to-volume ratio, good interconnectivity of the pores, which make them very popular. Regenerative medicine is one the main applications in which electrospun membranes are used. Tissue engineering requires new tools, sophisticated materials, which can properly interact with a biological environment. Electrospinning offers great fibrous materials, which resemble extraordinarily to connective tissues. Thereby, cells are able to colonize and proliferate inside the intricate network of fibers that mimics the natural extra cellular matrix. Electrospun membranes possess all set of required biomaterial properties to be used as temporarily scaffolds.

Electrospinning was intensively used last decades to produce nanofibers. Nevertheless, fiber structuration at a macro scale is not fully controlled. Strong bending instabilities induced by the high applied voltage triggers a random deposition of the fibers. Complexity of the techniques, sensitivity to environmental parameters and solution parameters involved make the production and reproducibility of the method critical. Fabrication frustration is often encountered in the community to the point that some scientists suggest that *“Electrospinning is an art rather than a science”* - “Marc Simonet” (EUPOC2019 conference, Como, Italy). Most of the constructs adopt an isotropic morphology with a random fiber organization. Moreover, fibers usually create thin membranes of a few hundreds of micrometers. Creating more organized constructs with defined macrostructures remains a big challenge in electrospinning. We are looking nowadays to fully reconstruct with great accuracy 3D components with fibers. Goal is making evolved electrospinning from a membrane to 3D printing scaffold technology.

In this study, we aimed to improve and contribute to the electrospinning science by structuring scaffolds to mimic in a better way natural tissues. Polycaprolactone (PCL) was employed as biodegradable and biocompatible materials to create electrospun fibers. In this work, macrostructures

were induced by micro-structured templates designed to orientate and create anisotropic fibrous scaffolds. The objective of the study is to create innovative scaffolds by electrospinning with tunable mechanical properties for soft tissue regeneration applications.

The first chapter of this manuscript introduces the current technology of PCL electrospun scaffolds for tissue engineering. An overview of the electrospinning technique and its processing parameters is detailed following by a description of current advances in fiber structuration using electrospinning. The chapter will end by a discussion concerning the mechanical characterization of electrospun membranes.

The second chapter is dedicated to the development of structured PCL membranes by electrospinning. Fabrication method with the new designed micro-structured collectors are firstly introduced. Patterned scaffolds with honeycomb and square patterned are successively presented and their morphology thoroughly analyzed.

The chapter 3 is focused on the mechanical analysis of the electrospun membranes previously produced. Uniaxial tensile test with a local strain monitoring will assess the anisotropic behaviors of both scaffolds.

The last part of the thesis is dedicated to the elaboration of a finite element model of structured electrospun mats. Experimental mechanical tests are simulated via a numerical approach in order to reproduce axial tensile tests of the architected electrospun membranes. By predicting their mechanical behaviors to different stimuli, numerical simulation of electrospun scaffolds is a promising tool to design more efficient medical devices.

The work accomplished during this 3 years project has been carried between two laboratories of University Grenoble Alpes: Laboratoire Rhéologie et Procédés where membranes were produced by electrospinning and TIMC (Laboratoire Technique de l'Ingénierie Médicale et de la Complexité – Informatique, Mathématiques et Applications de Grenoble), more involved in mechanical testing and modeling of the scaffolds. This thesis work contributed as well as a part of a bigger research project (ANR BioScaff), with a third participating institute in Montpellier (IBMM-BA, Institut des Biomolécules Max Mousseron - Biopolymères Artificiels), focusing on polymer chemistry and biological cellular responds of the electrospun scaffolds.

1. Electrospun materials for soft tissue regeneration applications. Elaboration techniques, morphological and mechanical properties

This first chapter gives a broad introduction to tissue engineering and the use of fibrous scaffolds in regenerative medicine. After a short morphological description of natural tissues aimed to be replaced, we detail targeted properties of PCL scaffolds produced by electrospinning. In the second part of this chapter, the technique of electrospinning is presented with a description of setting parameters involved in the complex process of fiber formation. The third part gives an overview of the current methods to organize fibers in electrospinning. Finally, the last part is dedicated to mechanical characterization of electrospun fibrous membranes and the evaluation of anisotropic scaffold behaviors.

1.1. Tissue engineering and its scaffolds

1.1.1. Tissue engineering: a definition

Biomaterials have been playing a crucial role in modern regenerative medicine. Nowadays, new methods are developed to replace damaged, burned, partially or fully lost tissues following severe accidents. The latest study on severely burned people was done in 2004 by the World Health Organization, showing that nearly 11 million people worldwide required medical treatment after burn injuries [3]. New ways to improve soft tissue healing are needed to limit tragic injuries caused by burns.

Tissue engineering refers to a scientific field which aims to the development of biological substitutes capable of replacing diseased or damaged tissue in the human. The term was introduced in the late 1980s where the concept of applying engineering to the repair of natural tissues appears to revolutionize important areas of medicine [4]. It has been a real challenge these past last years to develop new tools for surgeons, especially in the domains of soft (skin, veins, arteries, whole organs) or hard tissue (bones, cartilages, tendons) replacements.

Tissue engineering implies the use of a scaffold, a structural material designed to substitute a damaged tissue [5]. These scaffolds are made of natural or synthetic materials, and can be implemented with proteins, growth factors or human cells to boost their bioactivity. The primary function of a scaffold is to provide a *temporary* mechanical support. Ideally, the artificial construct will be degraded or reabsorbed at the same rate of the new tissue regrowth. Thus, new naturally formed ECM will replace the artificial template in a controlled manner.

Scaffolds are not only inert synthetic structures. They are designed to be active materials which interact with the human body. Chemical and physical signals are transmitted to deliver cues to cells. New biomaterials for tissue regeneration are tailored with active molecules, peptides, growth and differentiation factors to mobilize cells [6].

Architecture of the scaffolds needs to foster mass transport of proteins and nutrients in order to encourage cell adhesion, proliferation and differentiation. Ultimately, artificial constructs would control the size and shape of the neo tissue. Scaffolds should be tridimensional matrices that replicate, as far as possible, a natural and friendly environment for cells and define a new artificial niche where a target tissue can develop.

A successful example of guided tissue regeneration can be pointed towards the work of Stephen Badylak [7]. He received in 2018 a Health Care Hero Award for its regenerative medicine works. Several individuals have experienced severe volumetric loss of muscle tissue in the extremities (arms and legs) due to traumatic events such as a bomb or a car accident. Drs Stephen Badlak and Peter Rubin used de-cellularized porcine bladders to recreate a friendly environment and spur new muscle growth. Spectacular recoveries were observed after a few months over 13 treated patients. Muscle tissues were successfully reconstructed leading to dramatic improvements on physical tests. Tremendous works still need to be done to fully reconstruct human tissues and design specific part of tissue replacements. Nevertheless, scaffolds to guide tissue regeneration is an effective approved method in medicine. Material science technologies, dedicated to recreate, are inspired from actual living organisms.

1.1.2. Biological tissue in the human

Designing suitable scaffolds for regenerative medicine requires a closely pairing between the 3D construct and properties of the native Extra Cellular Matrix (ECM).

The organic ECM refers to the network composed of extracellular macromolecules that provide a structural and biochemical environment for the cells. Biological systems consist of a meshwork of proteins, minerals and molecules at the submicron scale. ECM is composed of fibers, fibrils, riddles of collagen, gelatin or elastin forming a very complex architecture. Their structural properties highly depend on the body sites, which are deeply contrasting from skin tissues to cartilages or bones. **Figure 1.1 (a and b)** shows SEM images of natural porous structures present in the living body (fibers in a heart muscle and a layered structure of a lumbar-intervertebral disk) [8]. Collagen or elastin fibers in the connective tissues have diameters ranging from a few nanometers to a few micrometers. **Figure 1.2.c** illustrates the fibrous network of a loose connective tissue composed of collagen fibrils, elastin fibers, macrophages and fibroblasts [9]. Collagen fibers are abundant forming irregular bundles stained pink/red whereas elastin fibers are scattered, thin dark strands strained blue/purple. Most of the nuclei are from fibroblasts, strained as well, which makes them difficult to differentiate from

collagen fibers. Natural tissues constructs exhibit anisotropic properties and are complexly organized to fulfill a specific function in the human body. The next challenge in regenerative medicine is to develop structures adapted to a particular tissue function, mimicking at the best the tissue to substitute. Detailed analysis of the ECM and natural components of the body is mandatory in order to better understand and conceive new artificial scaffolds.

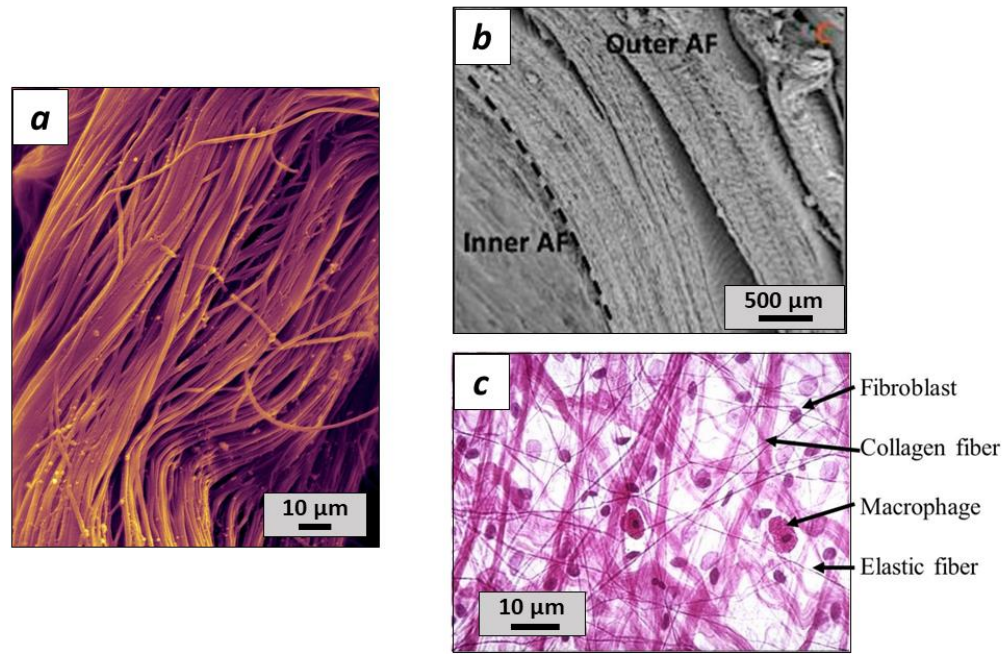


Figure 1-1: Natural tissue structures: a) Heart Muscle collagen Fibers, b) lumbar-intervertebral disk (outer and inner regions of Annulus Fibrosus) [8], c) histology slide of loose connective tissue [9]

1.1.3. PCL fibers as scaffolds for tissue engineering

A large variety of biomaterials has been recently developed to create scaffolds for tissue regeneration applications. Among the various methods of scaffold production, electrospinning was widely investigated during the last decade [10]. Electrospinning is a versatile and simple technique to produce nanofibers. Theory and process of electrospinning will be more detailed in the next **section 2.2**. Electrospun membranes consist in an intricate network of fibers with attractive properties for regenerative medicine. **Figure 1.2.a** [11] exposes a typical structure of fibers obtained by the technique of electrospinning (PCL fibers with average diameter of 466 nm).

Polycaprolactone PCL is a synthetic polymer extremely used for biomedical applications [12]. PCL is a linear aliphatic polyester chemical structure of PCL shown in **figure 1.2.b**, with a glass temperature of -62°C and a melting point of 55 to 60°C . It has a clean and slow degradation rate of 2 to 4 years

1. Electrospun materials for soft tissue regeneration applications. Elaboration techniques, morphological and mechanical properties

depending of its molecular weight. The biocompatible and biodegradable polyester was approved by the Food and Drug Administration [13]. PCL was clinically used as drug delivery carrier or suture material since the 1980s. PCL is soluble in various solvents and possesses rheological and elastic properties which makes it very easy to electrospin and to produce fibers. PCL nanofibers are widely explored as scaffolds for medical applications: drug delivery, bone, muscle, neural, renal skin or vascular tissue engineering.

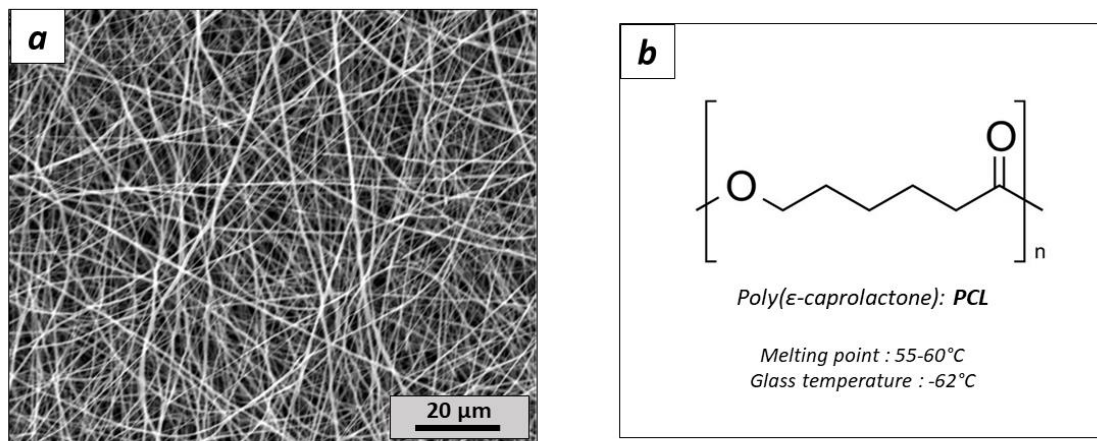


Figure 1-2: a) SEM image of PCL electrospun fibers (average fiber diameter = 466 nm) [11] b) Chemical structure of Poly(ε-caprolactone)

Table 1 lists most of the publications published from January to September 2019 in which electrospun PCL scaffolds are employed for tissue engineering applications. PCL fibers can be easily produced by electrospinning with other materials such as natural proteins, polymers, nanoparticles, drugs listed in the table. Nanofillers or polymers can be directly added into spinning solution. Two distinct polymers may be simultaneously produced by co-electrospinning coaxial electrospinning. 3D composite constructs can be created by layering several fibrous membranes, or by electrospinning fibers on 3D printed scaffolds. Moreover, post treatment and surface modification technologies offer new possibilities to tune and add new properties to PCL scaffolds.

PCL electrospun fibers possess a set of structural, biochemical and biological properties which make them suitable candidates for scaffolds in regenerative medicine:

High porosity

Electrospinning allows the formation of extremely porous materials. Porosities in electrospun membranes are extremely high, with values often superior to 80 %. This inside free space is needed for cells to invade and colonize the structure.

Interconnectivity

Pores of an electrospun membrane are interconnected in the fibrous structure. As the fiber is deposited continuously (see next **section 1.2**), a complex intricate network is formed where nutrients and cells would be able to navigate through.

High surface to volume ratio

Due to the cylindrical shape of fibers, electrospun scaffolds present more surface able to interact with cells compared to standard porous materials. Surface to volume ratio is 1000 times higher for a nano than a micro sized fiber. One considerable benefit is that surface could be easily functionalized in the electrospinning process, increasing cell-scaffold interactions.

Biocompatibility

The ability to support cellular activity without releasing toxic agents is crucial for a good recognition from the host body. Polymer used in electrospinning, such as PCL, have excellent biocompatibility properties.

Bioresorbability

An ideal scaffold needs to replace temporarily the missing tissue. Consequently, degradability of the construct is essential for an adequate regrowth of the tissue. Polymer such as PCL have healthy degradation mechanism adjustable to match development rate of new natural tissue.

Mechanical properties

Electrospinning provides fibrous membranes with controlled mechanical properties. Scaffolds with tailored mechanical properties can be obtained with PCL electrospun fibers, with properties close to properties of skin tissues. Moreover, PCL can be easily blend with other natural or synthetic polymer in the process of electrospinning, conferring more possibility to tune mechanical properties.

The main disadvantage of PCL is its high hydrophobicity and its poor wettability. This is a concern as scaffolds need to interact with fluids and cells. A lack of cell attachment and no interaction between the artificial construct and biological environment can reduce considerably the efficiency of the regeneration process [14], [15]. Fortunately, hydrophobic nature of PCL can be hindered by modifying the chemical and physical properties of the surface. Methods of surface modification such as plasma treatment, chemical treatment or proteins/polymer coating were successfully developed to increase wettability.

1. Electrospun materials for soft tissue regeneration applications. Elaboration techniques, morphological and mechanical properties

Applications	Materials	Reference
Bone/Tendon/Cartilage Tissue Engineering	PCL/chitosan/bioactive glass scaffolds PCL/collagen I hybrid nanofibers PCL/gelatin scaffolds with silicate nanoparticles PCL nanofibers PCL-PLA/HA scaffolds PCL-PEG-PCL/Elaeagnus angustifolia nanofibers Ethyl cellulose-PCL/alginate scaffolds with HA nanoparticles PCL/gelatin/nHA composite scaffolds Bionanocomposites of PCL + (nHA/graphene oxide nanofillers) PCL/PLLA fiber scaffolds Shish kebab-like PCL nanofibers PCL/Dicalcium Phosphate Dihydrate scaffold PCL fibers Kartogenin loaded PCL fibers Cell-derived PCL scaffolds Chitosan, cellulose acetate/PCL nanofibers Calcium phosphate/Polyvinyl Alcohol/PCL nanofibers Coelectrospinning of antibiotic-loaded PHBV//PCL scaffolds PCL and PCL/chitosan scaffolds PCL fibers with nanoparticles of HA and ZnO	Kandelousi [16] Lin, Yucheng [17] Wang, Yi [18] Metwally, Sara [19] Kareem, Muna M. [20] Hokmabad, Vahideh R. [21] Hokmabad, Raeisdasteh [22] Sattary [23] [24] Li, Yuchao [25] Shamsah, Alyah H [8] Tony Yu [26] Taghavi [27] Olvera, Dinorath [28] Zhu, Qi [29] Carvalho, Marta S [30] Zhang, Yishan [31] Shafiei, Shervin [32] Dalgic, Ali Deniz [33] Gniesmer, Sarah [34] Rahmani, Amin [35]
Cardiovascular Tissue Engineering	Gelatine/PCL composite membranes PCL/Ethyl Celullose/Collagen 1 scaffolds PCL-bisura scaffolds PCL/poly(glycerol sebacate) electrospun fibers	Feng, Bei [36] Aydogdu [37] Wissing, Tamar B [38] Vogt, Lena [39]
Drug delivery	Core-shell nanofibers of silk fibroin/PCL and clincamycin Doxycyline-loaded electrospun PCL/PEO membranes	Tanha, Nadia Rahimi [40] Eskitoros-Togay, [41]
Maxillofacial Tissue Engineering (Guided Tissue Regeneration)	PCL scaffolds PLA/PCL blended with HA and cefexine-beta cyclodextrin PCL + polydopamine nanoparticles PCL-polyethylene oxide-glycerophosphate	Fuchs, Andreas [42] Sharif, Faiza [43] Deng, Yi; Yang [44] Hosseini [45]
Muscle Tissue Engineering	Polypyrrole(PPy) and PCL copolymer fibers PCL and collagen nanofibers 3D printed with nanofibers scaffold (PCL)	Daniel Browe [46] Dippold, Dirk [47] Sooriyaarachchi [48]
Neural Tissue Engineering	Poly(e-caprolactone) (PCL), chitosan and polypyrrole (PPy) Silk proteins/PCL fibers Bacterial cellulose/PCL blend nanofibrous scaffolds PCL/polyaniline electrospun scaffolds PCL/polypyrrole/multiwall carbon nanotube	Ali Sadeghi [49] Baklaushev, V. P [50] Altun, Esra [51] Garrudo, Fabio F. F. [52] Nekouian, Soraya [53]
Renal Tissue Engineering	PCL porous tubular nanofiber scaffolds PCL/decellularized kidney ECM electrospun membrane	Jansen, Katja [54] Sobreiro-Almeida, Rita [55]
Soft/skin Tissue Engineering	PCL/Calendula officinalis/gum arabic fibers Aloe vera/chitosan/PCL/keratin fibers Core shells Lawsone/PCL/Gelatin fibers PCL/fibrinogen scaffolds PCL/collagen/quaternary ammonium salt Star-shaped PCL-COOH/PLA fiber mat Bioactive glass particles + PCL scaffolds Keratin/PCL fibers PCL fibers	Pedram Rad [56], [57] Zahedi, Elahe [58] Adeli-Sardou [59] Mirzaei-parsa [60] Xie, Xianrui [61] Zhang, Xue [62] Xie, Weihan [61] Cruz-Maya, Iriczalli [63] Gomes, Susana [64]

Applications	Materials	Reference
Vascular Tissue Engineering	Electrospinning and 3D printing (PCL + VEGF)	Lee, Sang Jin [65]
	PCL/gelatin nanofibres	Johnson, Richard [66]
	Loaded tubular scaffolds of (gelatin/PCL)	Ardila, D. C. [67]
	Tubular constructs of PCL and Gelatin fibers	Joy, Jincy; Pereira, Jessica [68]
	Fast degrading PCL - bis-urea scaffolds	van Haften, E. E. [69]
	Bicircular electrospun tubular vascular graft membranes	Tejeda-Alejandre [70]
	Herapin end-capped PCL small vascular graft	Jin, Xin [71]

Table 1-1: Main publications on electrospun PCL scaffolds for tissue engineering applications published in 2019

1.2. Conventional electrospinning

1.2.1. Electrospinning in our time

Electrospinning is a simple method to produce fibers at a sub-micron scale with the help of a high voltage source. First patents describing the process for preparing artificial filaments with an electric field was deposited by John Francis Cooley in 1902 and Anton Formhals in 1934 [74]. Nearly 60 years later, Doshi and Reneker published an article which is going to revive the enthusiasm around the electrospinning technique [75]. They described in the paper the elaboration of PEO (Polyethylene Oxide) fibers with a diameter in the range of 0.05 to 5 microns. This sudden interest in electrospinning technique can be related to the new progress in polymer science and new discoveries in polymer solutions. Since the 2000's, scientists have dedicated a lot of efforts to understand fiber formation mechanisms involved in electrospinning. **Figure 1.3** summarizes the publication production on the topic during the last 30 years showing the exponential interest of the field since 1995. In 2019, a total of 3490 publications were produced on electrospinning in a variety of scientific journals.

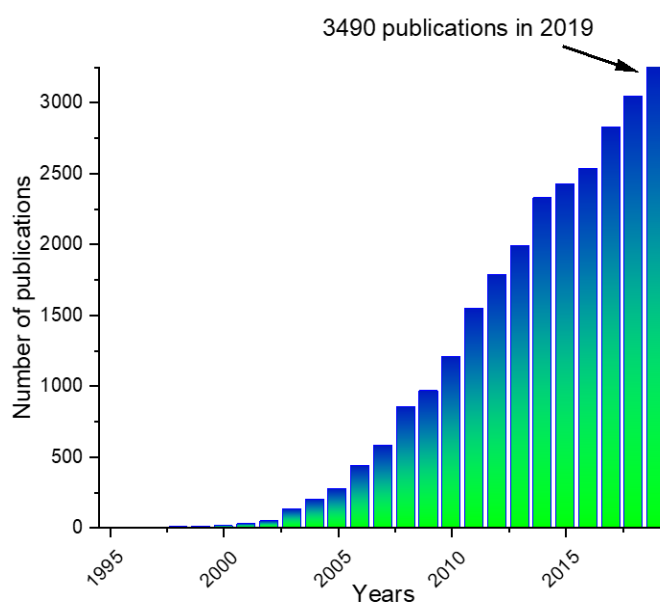


Figure 1-3: Publications on electrospinning from 1995 to April 2020 - Web Of Knowledge.

1. Electrospun materials for soft tissue regeneration applications. Elaboration techniques, morphological and mechanical properties

Such interest can be related to the simplicity of the method, to the large amount of electrospinnable polymers, to the easy functionalization of the fibers, and the associated development of a wide range of applications (filtration, sensors, wearables, textile, protection, tissue engineering, etc.)

Andreas Greiner interestingly described the evolution of electrospinning technology through a Gartner's hype cycle (**figure 1.4**). He places the current scientific progress right after the trough of disillusionment and explains how scientists need to push the emerging technology to the next level, reaching a plateau of productivity. "Develop and make it useful". Electrospinning technology begins to be well recognized for its potentials. Scientist need to be creative and embrace all possibilities that electrospinning offers.

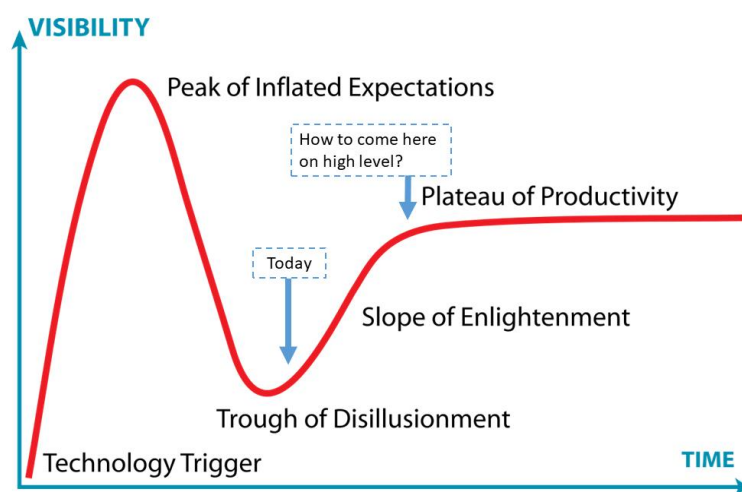


Figure 1-4: Gartner's hype cycle of Electrospinning according to Pr. Andreas Greiner lecturer at the 6th international conference on electrospinning - Shanghai – 2019.

1.2.2. Theory and set up

A simple electrospinning set up is composed of 3 main components as shown in **figure 1.5**: a high voltage power supply, a syringe containing the spinning solution and a grounded collector. Electrodes are connected to the spinneret and the collector. The polymer solution is placed in the spinneret and slowly expelled at a constant flow rate to balance the polymer solution expelled by the electric field.

Fiber formation in electrospinning relies on the balance of electric forces and surface tension. The solution accumulated at the tip of the needle will be locally charged due to the effect of the high voltage applied. Consequently, polymer solution at the tip of the needle will be stretched and form a Taylor cone as illustrated in **figure 1.5**. Once the forces induced by the charges overcome the surface tension, a jet of polymer solution is initiated. A continuous jet is formed, following initially a straight path over a few centimeters (first segment usually visible to the naked eye). Then the filament will

undergo bending motions, Rayleigh and whipping instabilities. The first instability tends to minimize the surface tension of the solution by forming droplets. The second induces the global spirally motion of the jet. During this phase, fibers are elongated and their diameters are reduced while the solvent evaporates. Finally, dried fibers are deposited onto the collectors, forming a randomly-organized or nonwoven fiber network. Fiber diameters obtained by electrospinning usually range from a few nanometers to a few microns.

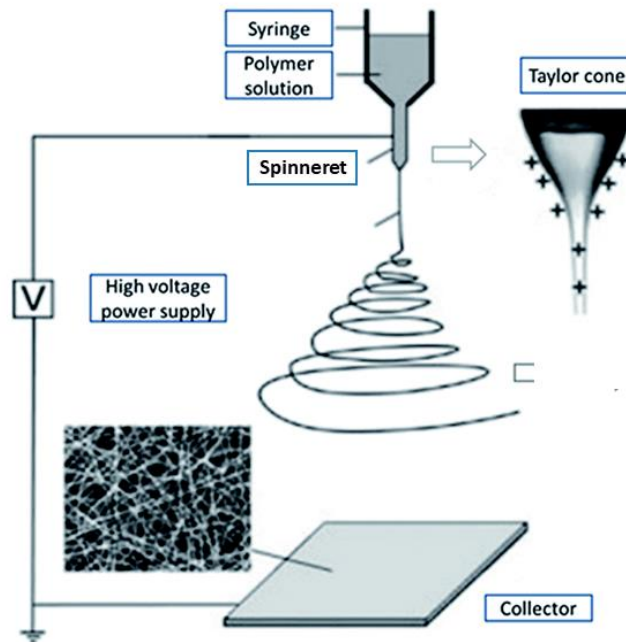


Figure 1-5: Electrospinning set up – Taylor cone formation and whipping phase. [76]

1.2.3. Electrospinning parameters

Electrospinning is governed by a set of parameters which need to be well adjusted in order to obtain a stable jet of polymer. They are classified in 3 main groups: parameters related to the polymer solution, to the process and to the environment. Each of these parameters will greatly influence the final fiber morphology.

1.2.3.1. Solution parameters

Solution parameters include viscosity [77] (concentration and molecular weight, fiber entanglement [78]), surface tension, conductivity of polymer-solvent system (surface charge density) and solvent volatility.

1.2.3.1.1. Viscosity

Viscosity of the spinning solution is a crucial parameter which directly influences the formation of a continuous and uniform jet [79]. Polymer molecular weight and concentration are directly linked to the viscosity of the solution. **Figure 1.6** illustrates 3 viscosity regimes depending on the polymer concentration.

- [I] = Low polymer concentrations ($c < c^*$) refer to a *dilute regime* where polymer chains are isolated. The critical concentration c^* , defined by De Gennes, marks the boundary between the dilute and the semi-dilute regimes. There is no cohesion of polymer chains in this state as they are too far from each other to interact. Rayleigh instability will induce the formation of droplets and only particles will be collected. This process is called electrospray. Numerous studies proved that electrospraying techniques can be efficiently combined with electrospinning to embed fibers and create interesting composites.
- [II] = A *semi dilute, untangled regime* is obtained when concentration has a value between the critical concentration c^* and the critical entanglement concentration c_e ($c^* < c < c_e$). Polymer coils start to merge and interact but molecules are not entangled. In this electrospinning regime, fibers with beads are created.
- [III] = At a further increase of polymer concentration, a *semi dilute, entangled regime* ($c > c_e$) is reached. Sufficient chain entanglements occur to confer a higher viscosity to the spinning solution. Stable electrospinning jet can be obtained and uniform fibers are produced. Suresh et al. studied chain entanglement in electrospinning and determined that a complete and stable fiber formation occurs if the average entanglement number per chains is superior to 2.5. [80]
- [IV] = After a maximum value of concentration, polymer solution becomes too viscous to be electrospun. The solvent will evaporate rapidly and polymer will accumulate at the tip of the needle, provoking needle clogging.

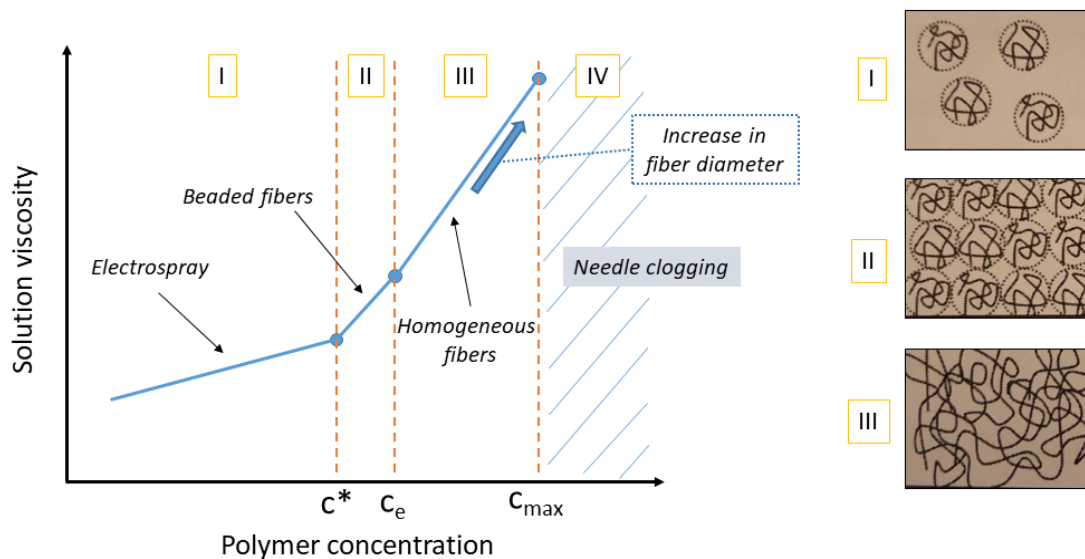


Figure 1-6: Viscosity vs concentration polymer solution – [I] dilute regime ($c < c^*$), [II] semi-dilute regime, untangled ($c^* < c < c_e$), [III] semi-dilute regime, entangled ($c > c_e$), [IV] Needle clogging (highly viscous)

It can be noticed that in the electrospinning window, i.e. in the semi dilute-entangled regime (III), an increase of viscosity leads to the formation of larger fibers. Indeed, polymer solution with higher viscosity increases the cohesion of the polymer thus the stability of the jet, reducing the whipping effect.

1.2.3.1.2. Surface tension

Surface tension of the spinning solution controls initially the shape of the droplet at the extremity of the syringe. With no external field, the droplet adopts a spherical shape to limit the surface energy of the system. With a voltage applied, the droplet of polymer solution will adopt a conical shape, named Taylor cone. Additional electrical force tends to stretch the polymer solution whereas the surface tension will trigger an opposite reaction. Surface tension greatly influences the stability and the shape of the evacuated polymer jet as well. Basically, surface tension will determine the electrospinnability domain if all other variables are held constant [81].

1.2.3.1.3. Surface charge density/ conductivity

Solution conductivity influences both the Taylor cone at the tip of the needle and the final diameter of the nanofibers. The spinning solution needs to have enough charges to be able to react to the electric fields and deform the spherical drop into a Taylor cone (**figure 1.7**). A critical minimum value of conductivity is required to initiate the jet in electrospinning.

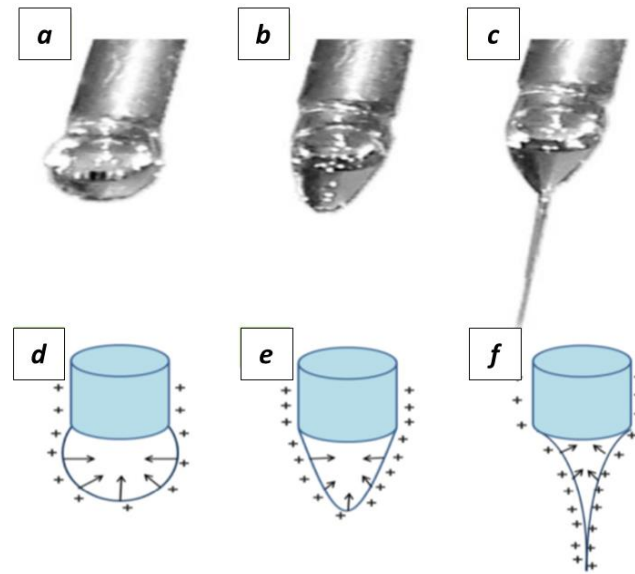


Figure 1-7: Polyvinylpyrrolidone droplets observed at the tip of the needle in an electrospinning experiment. Zoom onto the Taylor cone formation mechanism: Surface tension of the polymer solution competing with the effects of charges on the polymeric droplets to initiate the polymer jet. [82]

Moreover, it has been shown that increasing the conductivity of the solution triggers a decrease in fiber diameters [2].

Conductivity of polymer solution can be monitored by the addition of salts or minerals [83]. The increases of ions in the solution will multiply the number of charge carriers, therefore, an increase of the overall charge density. With the introduction of a small amount of benzyl trialkylammonium chlorides to poly(-3-hydroxybutatyrat-co-3-hydroxyvalerat) solution, Choi et al. [84] manage to improve the uniformity of their electrospun fibers and reduce their diameters to 1.0 μm . However, mineral particles added to the process could remain visible in or at the surface of the fibers, disrupting the smooth morphology of the fibers.

1.2.3.1.4. Solvent volatility

Solvent volatility is an important parameter to electrospun a specific polymer. First, raw polymer needs to be completely soluble in the solvent. Secondly, it has to have a moderate boiling point in order to evaporate fully during the travel from the needle tip to the collector. Volatile solvents are preferred for electrospinning. Nevertheless, a too fast evaporation could cause polymer drying at the tip of the spinneret blocking the needle and the polymer flow.

With the use of a two blend solvents with distinct evaporation rates, highly porous electrospun fibers can be interestingly produced as illustrated in **figure 1.8** [85]. A phase separation occurs before the polymer reaches the collectors leading to the formation of pores at the surface of the fibers. By changing the ratio of a DCM/THF solvent system, Megelski et al. developed several polystyrene fibers with different degree of macro textures, from porous to smooth fibers.

1.2. Conventional electrospinning

Koombahongse et al. [86] demonstrates that different polymer/solvent systems (HEMA + ethanol/formic acid, Polystyrene + DMF, PVDF + DMF/dimethylacetamide) could form fibers with different ribbon morphologies. A thin layer of polymer first dried at the contact to the ambient air forming a mechanically distinct polymer skin. Solvent inside will escape after the formation of this particular layer skin. Depending on the kinetics of the solvent evaporation, fibers adopted various morphologies such as cylinder, oval, ribbon like or flat ribbon shapes as shown in **figure 1.18.c**.

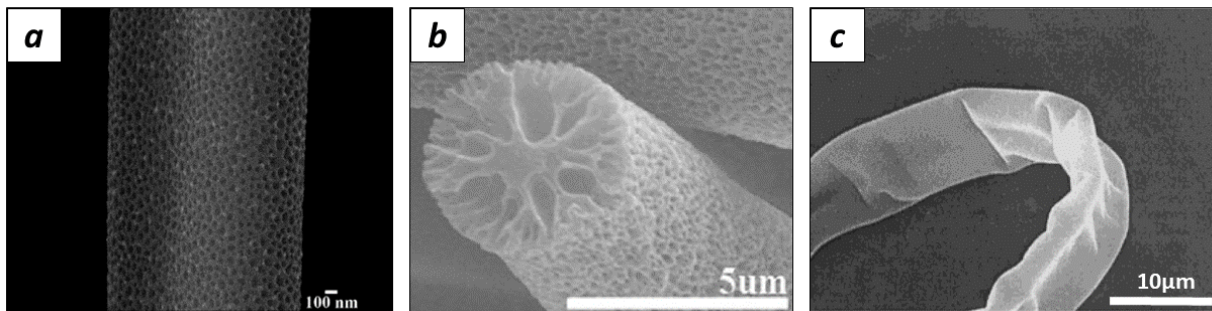


Figure 1-8: a) & b) SEM images of electrospun polystyrene fibers. The difference of evaporation rates of the two solvents (DCM/THF) triggers a phase separation resulting in a surface pore formation [85] c) Flat ribbon fibers of Polystyrene with irregular wrinkling [86]

1.2.3.2. Processing parameters

1.2.3.2.1. Voltage

Voltage is a fundamental parameter in electrospinning. It creates the required electric charges in the polymer solution to stretch and initiate the jet as mentioned previously (**figure 1.7**). The Taylor cone appears from a minimal value of the applied electric field. From this critical voltage, electric forces overcome the surface tension and the polymer is ejected toward the grounded collector.

At high voltage, the electric forces will be higher inducing in a more perturbed whipping motion. In most of the cases, a higher voltage implies a greater elongation and stretching, thus a reduction of fiber diameter [87] [88]. However, an increase of voltage can cause as well a reduction of flight time as the charged fibers are more attracted to the collector. In this case, diameter of the fibers could be slightly increased with the voltage.

At further increase of voltage, even the Taylor cone might be instable. A new configuration in a multi jets mode could be observed (**figure 1.9**). The technique of multi-jets in electrospinning can be used to improve efficiently the productivity of fibers. However, due to the high instability of the jet, there is a greater probability at high voltage to create fibers with irregular diameters with beads, thick and thin parts.

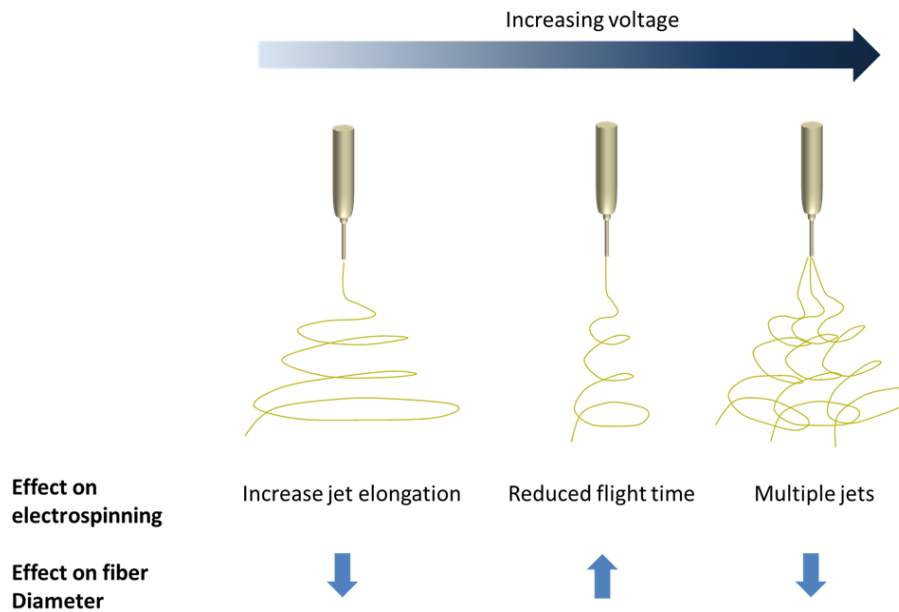


Figure 1-9: Voltage Effects on electrospinning and fiber diameter [89]

1.2.3.2.2. Tip to collector distance

Distance between the spinneret and the collector is one of the first parameter to set in electrospinning. It will determine the length that the continuous fiber needs to travel to reach the collector. Consequently, it is a crucial parameter to select a cruising time for a sufficient solvent evaporation, so that fibers are dry when collected.

Moreover, it will directly influence the intensity of the electric field perceived by the polymer solution at the tip of the needle. The Coulomb force F on a charge q is related to the electric field E , thus directly dependent on the potential difference $\Delta\Phi$, the distance d

$$F = q \cdot E = q \cdot \frac{\Delta\phi}{d}$$

According to the relation above, electric forces (F) decrease when the tip to collector distance increases, having a direct influence on the Taylor cone formation.

1.2.3.2.3. Feeding rate

Flow rate will control the amount of polymer solution expelled from the needle. A delicate balance between the feeding rate and the voltage is required to obtain a stable jet with a Taylor cone configuration (**figure 1.10.a**). Low feeding rates are usually applied to insure enough time to the polymer to be expelled from the nozzle tip during electrospinning [90]. On the contrary, high flow rates could generate non-regular fibers and beads as not sufficient time is allowed to the jet to properly

dry. An excess of feed rate, basically superior to 0.5 mL/min, will provoke an accumulation of polymer fluid and result in unspun droplets (**figure 1.10.e**).

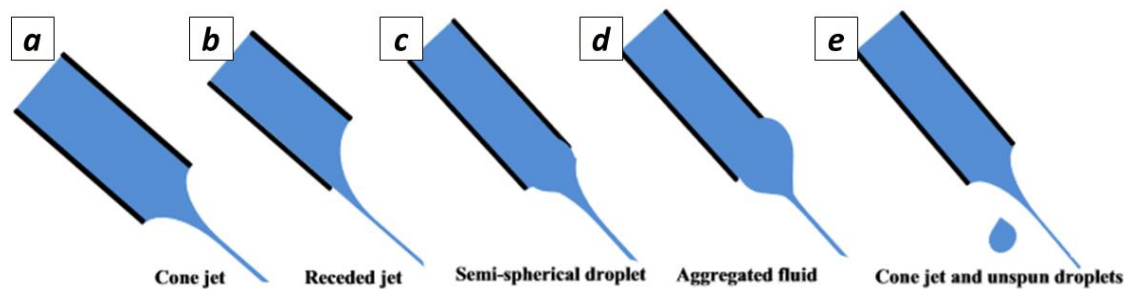


Figure 1-10: Formation of various jets with increasing flow rate [91]

1.2.3.3. Environmental parameters

Environmental parameters (relative humidity and temperature) are critical parameters for electrospinning as they affect greatly electrospinning solution parameters such as conductivity, viscosity or solvent volatility.

1.2.3.3.1. Humidity

Relative humidity is a major parameter to set in the electrospinning box as it deeply affects final morphology of fibers. Depending on the nature of polymers, humidity has a direct effect on the solidification of the jet. In several cases, an increase of humidity leads to a decrease in fiber diameter [92], [93].

Humidity can activate and accentuate the solvent evaporation rate difference in a two solvent blend polymer solution as described previously. Bae et al [94] observed a great influence of humidity on fiber morphology (**figure 1.8.b**). Highly porous fibers (56-70 %) were obtained with the formation of inner pores. This result is attributed to the condensation of water droplet at the surface of the fiber during the jet path. Water will mix with the DCM solvent and phase separation will create porous PMMA electrospun fibers [95].

1.2.3.3.2. *Temperature*

Temperature increases the rate of evaporation and decreases viscosity, both leading to a reduction in fiber diameter. Mit-Uppathan et al. [96] have investigated the electrospinning of polyamide-6 fibers at temperatures ranging from 25 to 60°C. They observed a decrease of fiber diameter with an increase of temperature. Results were interpreted as a reduction of viscosity related to higher temperatures. Similar results were observed by De Vrieze et al. [97] with cellulose Acetate and poly(vinylpyrrolidone) (PVP) fibers produced by electrospinning.

Table 1.2 summarizes the general effects of solution, processing and environmental parameters described in the section on fiber morphology. It is important to note that the following table cannot be applied for all the electrospinning results found in the literature. Exact relationships between parameters and fiber morphology will differ for each polymer/solvent system. Nevertheless, it draws qualitative trends of parameters involved in electrospinning, which could be useful to optimize a set of conditions.

Parameter	Effect on fiber morphology
Applied voltage ↑	Fiber diameter ↓ initially, then ↑ (not monotonic)
Flow rate ↑	Fiber diameter ↑ (beaded morphologies occur if the flow rate is too high)
Distance between capillary and collector ↑	Fiber diameter ↓ (beaded morphologies occur if the distance is too short)
Polymer concentration (viscosity) ↑	Fiber diameter ↑ (within optimal range)
Solution conductivity ↑	Fiber diameter ↓ (broad diameter distribution)
Solvent volatility ↑	Fibers exhibit microtextures (pores on their surfaces, which increase surface area)
Humidity ↑	Fiber diameter ↓ (pore formation)
Temperature ↑	Fiber diameter ↓

Table 1-2: Effects of electrospinning parameters on fiber morphology (inspired from Sill et al.) [98]

1.3. Structuration of fibrous materials in electrospinning

Conventional electrospinning creates nonwoven frameworks of fibers. Electrospun membranes are usually collected on planar collectors giving homogeneous fibrous scaffolds. The whipping instability of the electrospinning device induces a deposition with no organization at the fiber scale. In order to conceive better nanostructured devices with controlled morphology, scientists have been trying to organize electrospun fibers since 20 years. The next section is dedicated to the attempts to structure fibrous mats in electrospinning. An overview of the different techniques employed (self-assembling, use of rotating or 3D collectors) and of the resulting macro-organized scaffolds is provided.

1.3.1. Self-assembling: Dimpled/ honeycomb membrane

In some particular cases, collection of fibers onto a plane surface as in conventional electrospinning could lead to a self-formation of macrostructures. Self-organization of fibers is a phenomenon rarely observed in electrospinning which could be triggered with specific parameters. It is believed that the opposite actions of surface tension and electrostatic repulsion favor unusual fiber configurations in dimpled structures (**figure 1.11**).

Yan et al. [99] successfully produced with 3 different polymers (polyacrylonitrile, polyvinyl alcohol, and polyethylene oxide) self-assembled honeycomb nanofibrous structures illustrated in **figure 1.11.a**. The authors explained the structuration of such neat structures with a 5 steps mechanism theory described in **figure 1.11.b**. In the first step (I), wet fibers with remaining charges will tend to agglomerate and decrease their surface energy. Fibers will deposit along each other. Then, repulsive electrostatic forces will create a 3 branched system (II-IV). As the charges are dissipated by travelling from one fiber to the other until the grounded collector, points of contacts will have less charge density compared to the others. Once the initial framework of the first fibers completed, new fibers will be preferentially attracted to the lower charge density areas and stack to form the honeycomb structure (V).

With the similar self-assembly process, Moroni et al. [100] developed PCL fibrous meshes with a pore size gradient from 300 μm to 800 μm (**figures 1.11.c & 1.11.d**). The use of specific process parameters allowed a distinct honeycomb organization after 30 minutes of electrospinning.

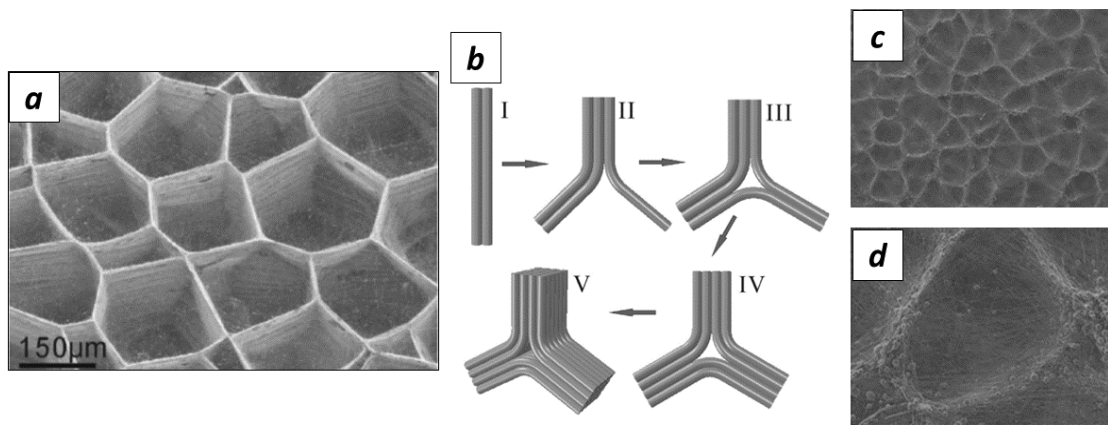


Figure 1-11: a) Self assembled dimpled fibers (Yan et al.) [99] b) Schematic showing the self-assembling mechanism of the wet electrospun fibers c) Self-assembled honeycomb fibers with pore gradient (Moroni et al) [100]

1.3.2. Aligned fibers

Alignment of the electrospun fibers in a preferential direction was intensively investigated during last decades. Techniques to orientate fibers can be classified in three main groups by using rotating collectors, gap collectors or centrifugal electrospinning.

1.3.2.1. Rotating collectors

Electrospinning with rotating devices such mandrels, wire drums, wheels, cones or frames is the most common and simplest method to fabricate uniaxial fibers [101]–[104]. The principle of electrospinning with a rotating collector is illustrated in **figure 1.12**. A rotating cylindrical support replaces the planar collector in order to catch and coil fibers. The collector is usually connected to the ground or placed between the two electrodes (spinneret and grounded electrode). Fibers will be attracted toward the collector and stretched around the cylinder. Rotating velocity of the mandrel should match the polymer jet speed, estimated to a few meters per second, to obtain a good alignment of the fibers. Main advantage of the wire drum collector illustrated in **figure 1.12.b** is that membranes are easily removed after collection due to the restraint contact between fibers and collector. Same quality of alignment is generally observed for both collector types.

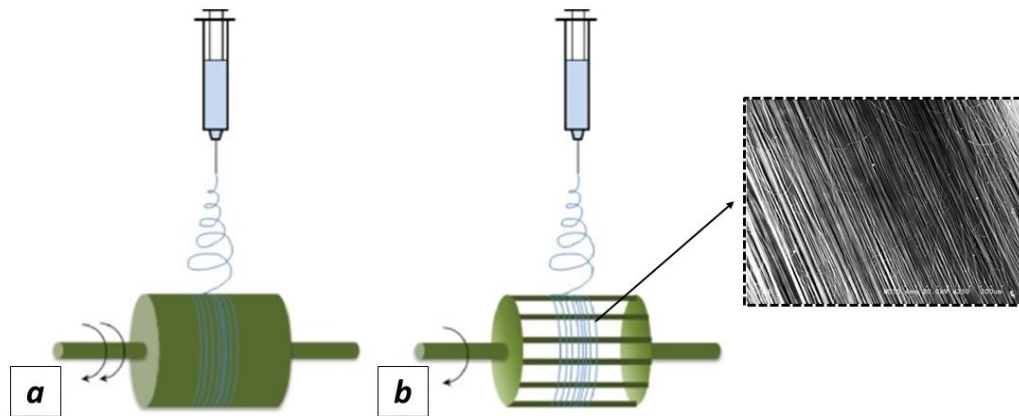


Figure 1-12: Electrospinning with rotating mandrel (a) and a wire drum (b) [104]

Rotation speed of the collector will greatly influence the final morphology of the aligned fibers. If the linear speed of the mandrel edge is too slow, fibers will not be aligned properly leading to a poor quality of fiber alignment. However, at high velocity (much higher than that of the fiber velocity), fibers might break due to an extreme elongation.

It has been shown that fiber diameters are decreasing with increasing rotating speed [105], [106]. Manuel A. Alfaro et al. [16] studied the effect of the rotating mandrel onto the PCL fiber morphology and degree of alignment. They have shown that the rotational force of the drum causes fiber alignment and a reduction in diameter. Diameters of the fibers are reduced by 15 to 40 % compared to the conventional electrospinning when the speed of the rotating collectors is between 5 and 15 m/s [107].

Aligned fiber mats with a large area and a significant thickness (up to hundreds of microns) could be elaborated with this technique. Nevertheless, as the membrane grows, charges are accumulated on the collectors. Repulsion between fibers increases and might at some point hinder the alignment process.

1.3.2.2. Gap collectors or parallel plates

Aligned fibers can be produced as well by locally modifying the electric field around the collectors. Charges in the polymer jet are driven by the electric field, thus a new design of collector will modify the forces involved and favor an organized fiber deposition. Gapping or void gap collection consists in changing the plane collector by two conductive electrodes separated by a gap [108].

Li et al. [109] used two silicon parallel plates to control the bending instability inherent of the electrospinning process (**figure 1.13.a**). Rectangular stripes cause the deposition of the fibers across

1. Electrospun materials for soft tissue regeneration applications. Elaboration techniques, morphological and mechanical properties

the air gap, perpendicular to the plates as shown in **figure 1.13.b**. It is hypothesized that fibers are stretched by the electrostatic interactions to span across the gap.

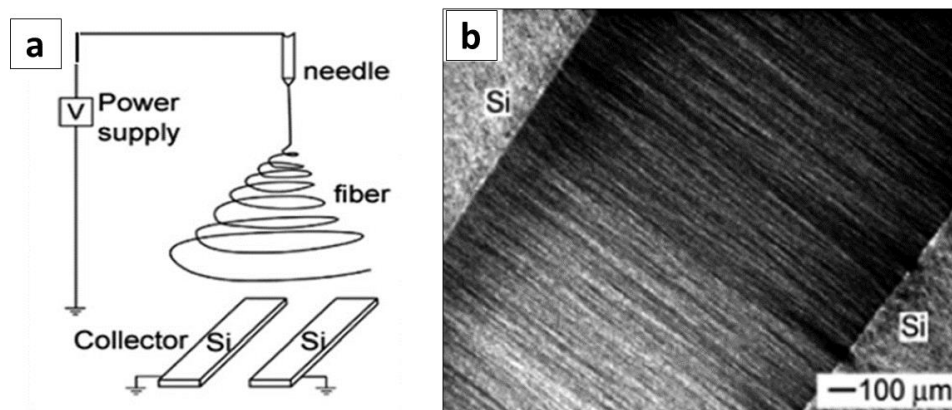


Figure 1-13: Aligned fibers with Si electrodes separated by an air gap (Li et al) [109]

Gap size could vary from a few microns to a few centimeters. Liu et al investigated the distance of the air gap in this method collection and explained that alignment improves substantially with a gap increasing from 3 to 8 mm. The maximal distance separating the two electrodes is determined by the diameters of the fibers and polymer physicochemistry. Above this maximal value, fibers will break, probably due to an over stretching of the fiber or to the fact that they cannot support their own weight beyond a certain length [110].

As explained in the previous section, the accumulation of the charges on the deposited fibers hinders the alignment process. This phenomenon is more observed in this technique as fibers are hanging in the air between the two electrodes. As they are not in direct contact with a grounded surface, charges will be less likely evacuated.

1.3.2.3. Centrifugal electrospinning

More recent electrospinning devices were developed to align fibers with the help of centrifugal forces. The centrifugal electrospinning set up is shown in **figure 1.14**. Here the spinneret is rotated instead of the collector and fibers are deposited on an annular collector. The addition of the centrifugal force allows the fabrication of fibers at lower voltage, typically 3kV [36],[37]. However, centrifugal electrospinning involves a complex set up with often larger rotating devices involved. The spinning process needs a high rotational speed which will potentially create new safety hazard.

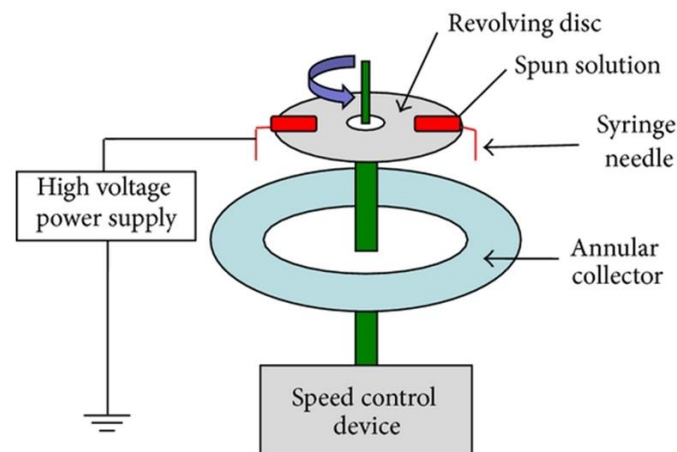


Figure 1-14: Centrifugal electrospinning [111]

1.3.3. 3D templates

Scientists nowadays want to improve the control of geometry, diameter and pore size of electrospun scaffolds at a micro scale. A more controlled structuration of electrospun fibers would allow the design of appropriate scaffolds to closer mimic natural tissues or implement new features.

Intensive studies to enhance structuration in electrospun mats have been conducted in template assisted technique. Conductive or nonconductive 3D supports can be easily fabricated nowadays with the new current technologies (3D printing, lithography, electro erosion, laser cutting, etc).

By using such new type of 3D collectors, the electric field will be locally distort delimiting a new pathway for the fibers. The next section is focused on the recent breakthroughs in fiber organization using patterned templates.

1.3.3.1. Grids/wire nets

From the early 2000's, grids or wire nets started to be used as collectors to collect fibers with a patterned architecture in electrospinning.

Vaquette et al. [113] exploited metal grids or drilled plates to collect patterned fibrous mats. Their results showed that fibers are preferentially deposited on the conductive parts in both cases. Fibers accumulate on the grid and form a micro pattern mimicking the conductive template (**figure 1.15**). A typical grid structure favors the deposition of the fibers along the wires or on the conductive parts. The upcoming propelled fiber will continue its path towards the adjacent metal zone with higher probability in order to stay on a conductive component. The result is the formation of two distinct zones of low and high fiber density. Fibers will tend to align along the wires whereas a random collection is observed across the gap.

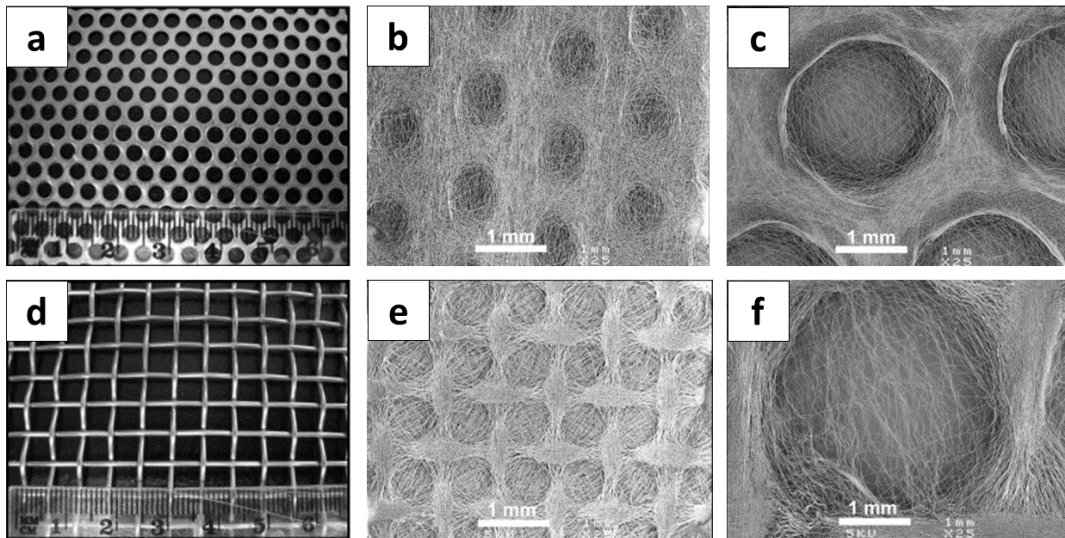


Figure 1-15 - Structured PCL fibers electrospun on wire and round collectors, Vaquette et al. [113] (a) round collector, (b-c) round scaffolds, (d) wire collector (e-f) wire scaffolds

It is believed that electrostatic forces drive fibers to move to the conductive parts of the template. **Figure 1.16** illustrates a numerical simulation of the electric field lines at the vicinity of a patterned collector. In conventional electrospinning, electric field lines are homogeneously distributed toward the flat collector (**figure 1.16.a**). However, with structured collectors (**figure 1.16.b**), lines are disrupted and directed towards the conductive parts. Indeed, the electric field is stronger in these areas than in the insulating parts. Electric field is confined to the immediate vicinity of the mesh collector surface. Titov et al. [114] described in their computer modelling work the electrostatic sensitivity of a charged fiber reaching a conductive grid. They found that electric field strength in the horizontal direction significantly increases when the fiber approaches to the patterned collector (i.e. < 1mm). Moreover, when the membrane thickness reaches a value superior to 500 μm , electric field comes back in a homogenous configuration and fibers are randomly deposited. This loss of microstructure was often experimentally observed in several templated assisted collection after a few hundred microns of deposited polymer [115], [116].

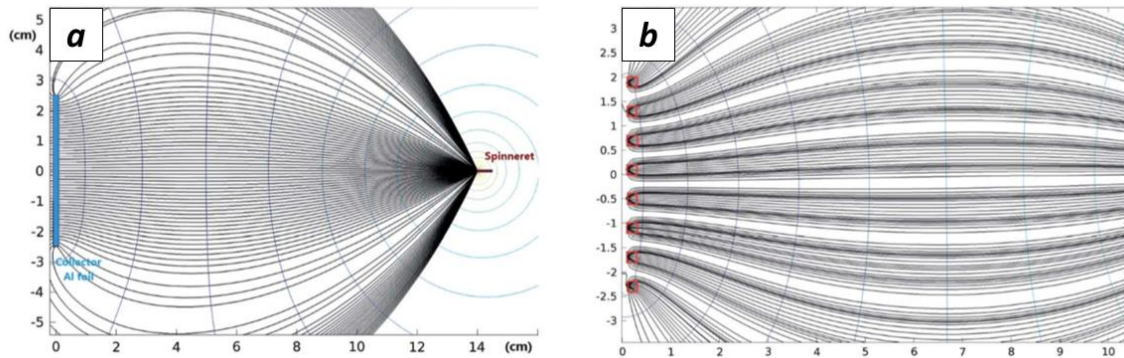


Figure 1-16: Electric field simulations with a) aluminum foil and b) metal grid (Zho et al) [115]

1.3.3.2. Protrusion templates

Applying the same principle of changing the electric field at the surface collector, 3D templates with protrusions can be developed to arrange spatially electrospun fibers. **Figure 1.17** shows the deposition of PCL fibers onto conductive templates inscriptions [117]. Letters of 1mm² were successfully reproduced on the free standing electrospun membrane. As previously described, the modification of the collector topography triggers a controlled deposition onto the conductive protrusions.

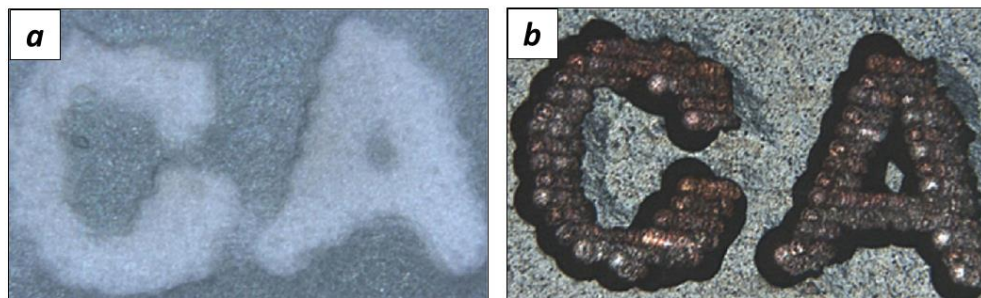


Figure 1-17: Optical images of electrospun membrane (a) over the corresponding part of the collector designed on a printed circuit chip (b) [117]

Wang et al. [118] electrospun fibers on stainless steel screws to analyze fiber organization surrounding a protrusion. Fibers formed in this case a pyramidal shape around a single probe as shown in **figure 1.18**. Fibers are strongly attracted to the top of the protrusion which is situated closer to the spinneret. If two probes are putted next to each other, a fiber bridge can be formed as in a void gap configuration (see previous section). Wang et al. [118] determined with simulation studies a critical distance of 20 mm to connect with fibers 25 mm high probes. Ratio between the distance (separated

1. Electrospun materials for soft tissue regeneration applications. Elaboration techniques, morphological and mechanical properties

the two conductive parts) and protrusion height requires to be inferior to 1 in order to obtain a fully suspended fibrous membrane (no fibers reaching the bottom of the collector).

Ortega et al. [119] observed a similar dependence with the height of a single ring collector (**figure 18.1.c**). In their experiments, they increased thickness of cell templates in order to control the fiber density difference between the center of the niche (air void) and the outer ring (conductive part).

At low template height (case A), fibers are able to reach the ground floor collector whereas at higher template thicknesses (case B, C and D), fibers are mainly deposited on the collector ring surface creating “empty” zones of low fibers density (bright inner and outer ring areas). They measured, for four templates with different thicknesses, the distance D which corresponds to the width of the outer area that surrounds the electrospun rings (**figure 18.1.c**). Distance D was found to be linearly linked to the height of the ring collector.

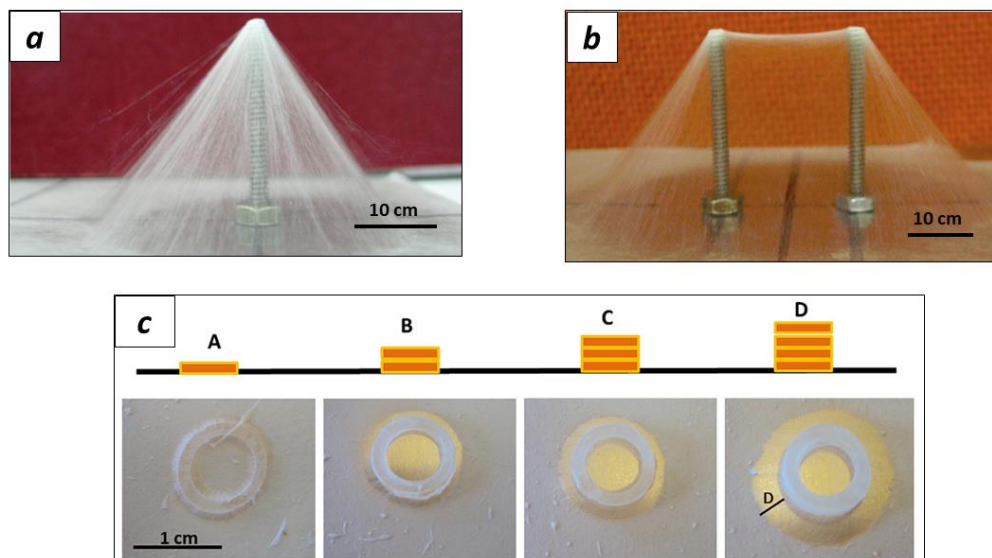


Figure 1-18: a-b) Fibers collected on probe collectors [118], c) fibers electrospun on a rounded-niche collector [119]

Repetitive meshes made of probes, pins or needles were investigated to produce suspended patterned electrospun membranes [116], [118], [120]–[122]. Qiao et al. [120] elaborated structured mats by collecting fibers onto probes arrays. In this process, they compared their porous architected membranes to random membranes produced on a plane collector. They noticed an increase in pore size from 7.6 μm to 13.2 μm and a reduction of fiber diameter (from 2 μm to 1.5 μm) with the use of the probes collector. Liu et al. [123] interestingly produced 3D membranes by changing the height of the needles on a same collector. Specific structures with different elevations such as convex, triangle wave, inverted cone and complex curved surface were built (see **figure 1.19**).

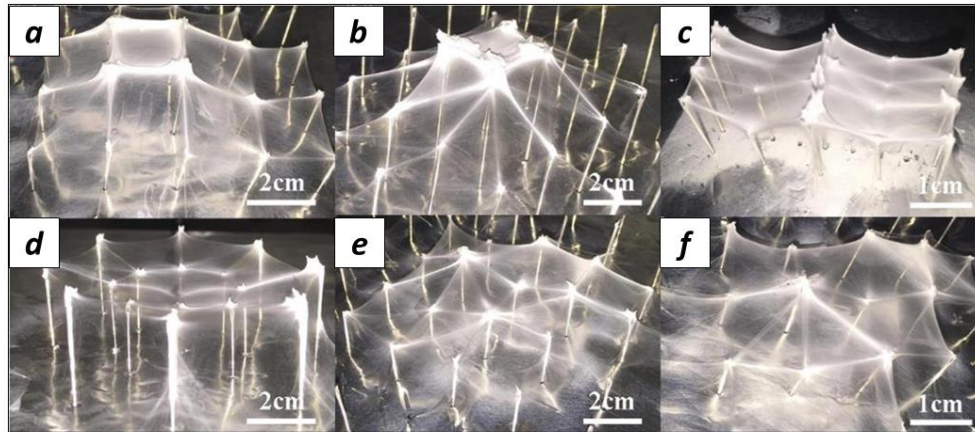


Figure 1-19: 3D nanofibrous structures printed on probe arrays with non-uniform probe heights. (a,b) Convex; (c) triangle wave; (d) inverted cone; (e,f) complex curved surface. [123]

Fiber structuration onto patterned collectors relies on two main factors: the velocity of the fibers when they reach the surface of the collector and the electrostatic attraction due to the charge surface density. Zhang et al [124] studied the effect of three electrospinning parameters (voltage, feeding rate and solvent conductivity) on the structuration (**figure 1.20**). When high voltage is applied, the fibers arrived to the collector with high velocity. The result is a poor structuration as kinetics will be predominant over the electric attraction (**figure 1.20.a**). Similarly, an increase of feeding rate will induce a chaotic organization (**figure 1.20.b**). It is reported that charge density is lower with a high feeding rate. Thus fibers produced at high feeding rate are less organized as the electrostatic attractions are smaller. Finally, **figure 1.20.c** exhibits solvent conductivity effects on structuration. It is with the solvent with a blend of 4:1 of DMF:THF, where the charge density is higher that fibers are well aligned between the protrusions.

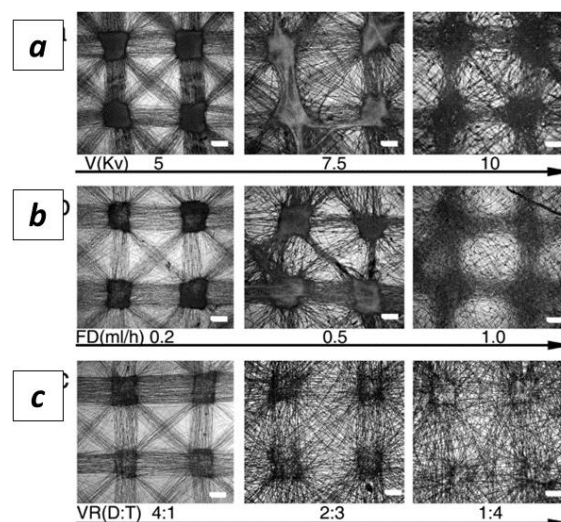


Figure 1-20: Influence of Voltage (a), Feeding rate (b) and conductivity (c) of the solution over the structuration. (Zhang et al) [124]

1. Electrospun materials for soft tissue regeneration applications. Elaboration techniques, morphological and mechanical properties

3D templates from lithography were developed as new collectors for electrospinning (Schalter, Lee, tallawi 2016). Nedjari et al [125] developed remarkable thick scaffolds with a honeycomb structure. They used soft lithography to fabricate a 3D collector with regular meshes (**figure 1.21.a**). Structuration of PCL fibers is explained by the bi modal behavior of the fiber jet as illustrated in **figure 1.21**. Thicker part of the fiber (diameter d_2), containing a higher charge density will deposit on the wall of the honeycomb mesh. Meanwhile, thinner parts will occupy the center of the mesh. The accumulation of positive charges forms a repulsive area in the core whereas fibers in direct contact with the substrate will discharge rapidly and create an attractive pole. The organization of remaining charges will reinforce the electrostatic sensitivity for the new incoming fibers, resulting in an organized fiber deposition. Wittmer et al. [126] fabricated on the same 3D templates structured composite constructs by using simultaneously electrospinning and electro spraying. Particles produced by electro spray will deposit preferentially at the honeycomb wall, facilitating the release of the charges and reinforcing the repulsive-attractive zones disparity.

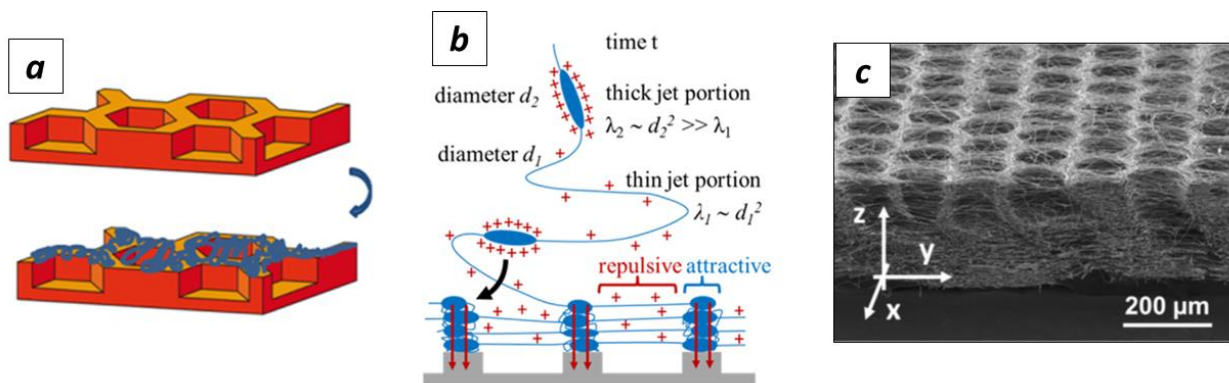


Figure 1-21: Electrospinning of PCL fibers onto 3D honeycomb templates: a) honeycomb collectors, b) mechanism theory of fiber deposition on conductive honeycomb templates, c) SEM image of structured PCL fibers (Nedjari et al) [125]

1.4. Mechanical properties of electrospun membranes

The evaluation of mechanical properties of the electrospun materials is a necessary step to validate a product for biomedical applications. Fibrous scaffolds need to host cells and withstand many biological forces: cell activities, tissue growing, pulsed blood flow, etc [127].

1.4.1. Natural tissues

Natural tissues exhibit a structural and mechanical anisotropy. In the case of human skin, Langer identified distinct orientations, called Langer's lines, where collagen fibers are parallel oriented in the dermis (**figure 1.22**) [128], [129]. Mechanical tests applied to skin samples in two directions, parallel

1.4. Mechanical properties of electrospun membranes

and perpendicular to Langer's lines, showed anisotropic behaviors [130]. Most of the soft tissue exhibit a strong anisotropy, with anisotropic ratio from 3 to 4 depending of its function and localization. **Figure 1.22.b** shows the stress-stretch curves for uniaxial tensile tests on human back skin parallel and perpendicular to the Langer's lines. Stress is usually plotted in function of stretch ratio (l/l_0) as in **figure 1.22.b** or global strain ($\Delta l/l_0$) with l being the gauge length and l_0 its initial value. Mechanical properties of natural soft tissues are usually ranging from a few to hundreds of MPa. **Table 1.3** details soft tissues Young's moduli measuring on human tissues by tensile tests in "wet" or "hydrated" conditions [131], [132].

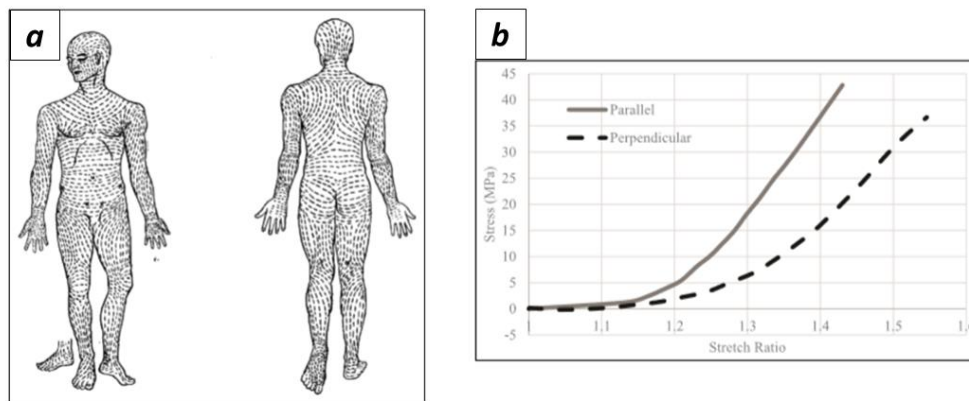


Figure 1.22: Langer's lines in the human body and mechanical anisotropy of skin tissue (parallel and perpendicular to Langer's lines) [130]

Tissues	Young's Modulus (MPa)
Bones	0.1 - 1000
Tendon	43 - 1660
Muscle	480
Skin	21 - 39
Liver and Kidney	1 - 15
Cornea	0.1 - 11.1
Sclera (white of the eye)	0.6 - 49
Spinal cord & gray matter	0.4 - 3.6
Artery & Vein	0.6 - 3.5
Breast tissue	0.167 - 29

Table 1-3: Young moduli of human tissues measuring by tensile stretching [131], [132]

1.4.2. Random and aligned electrospun membranes

The most common way to measure mechanical properties consists in applying a tensile load on rectangular fibrous samples. It is worth mentioning that precautions need to be taken while manipulating electrospun membranes as they are usually very thin and delicate. Sufficient caution is required to avoid a severe and definitive damage during sample handling.

Typical shape of Stress-strain curve obtained by tensile tests is shown in **figure 1.23**. Fibrous mats observed a bimodal behavior until rupture. A few set of mechanical data can be extracted from such curves. *Tensile* or *Young modulus* corresponds to the slope in first linear part (red), called elastic domain. *Tensile strength* which is the maximum load that a material can support without fracture, and *Ultimate Tensile Strain*, maximum elongation before rupture of the fibers. A Yield Point can be defined as the boundary of the elastic and plastic regions. It corresponds to the amount of stress required to produce a predetermined amount of permanent strain, usually 0.1 or 0.2 % (“percent offset”); *Toughness* which is all the energy that a material can withstand (depicted with the area under the curve).

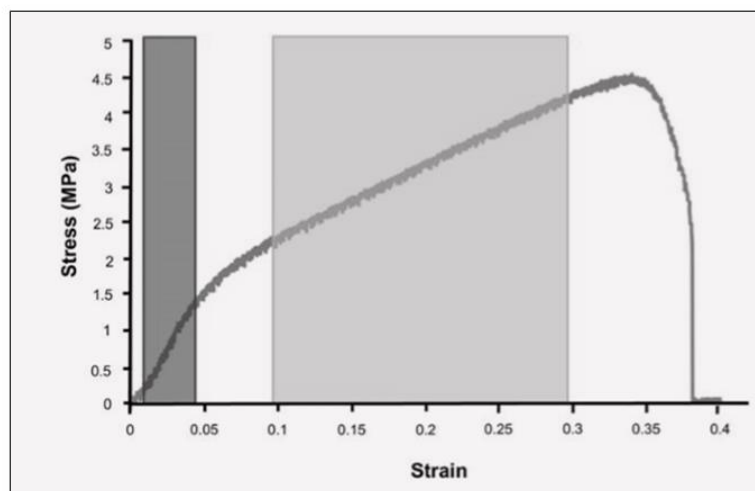


Figure 1.23: Typical stress strain curves of electrospun membranes [133]

These previously described material properties are not necessarily intrinsic to the polymer material. They highly depend on the morphology of the membranes, its macro structure and its thickness. Mubyana et al. [133] showed that material and failure properties vary with the specimen thickness and degree of alignment. Aligned and random PCL fibers were mechanically tested and ultimate tensile stress, Young moduli and toughness have a tendency to decrease with mat thickness. According to the authors, this thickness-dependent property would be related to underlying mechanisms such as fiber-to-fiber surface interactions (friction), fiber reorientation and fiber packing density.

Aligned fibers properties are often compared to a fibers collected by conventional electrospinning with a random organization. In general, aligned fibrous mats exhibit higher tensile mechanical strength (higher tensile modulus) when they are tested along the orientation of the fibers. Lee et al. (2002) had found that materials have different mechanical behaviors in different directions when membranes are collected by a rotating collector. Fiber orientation, depending on the velocity of the drum can be directly related to this mechanical anisotropy. Mubyana et al. [133] measured a significant increase of Young modulus and toughness (superior to x2) on aligned PCL fibers compared to randomly deposited fibers.

However, mechanical properties of the aligned fibers in transversal direction are poorly investigated. Yuan et al. [134] studied the anisotropy of aligned fibers of silk fibroin and PCL (**figure 1.24**). A modulus of 116 MPa was measured in the parallel direction compared to 19 MPa in perpendicular clearly pointing out the expected anisotropy of aligned fibers. Non-woven mats of the same electrospun fibers showed an intermediate value of 38 MPa. Shamsah et al [8] investigated the mechanical properties of PCL fibers at different orientations where the load was applied with a angle of 0, 30 and 60°. They showed that tensile properties were weaker for fibers not directly aligned to the load axis. Young modulus was decreased by 31 % and 73 % for angles of 30° and 60° respectively.

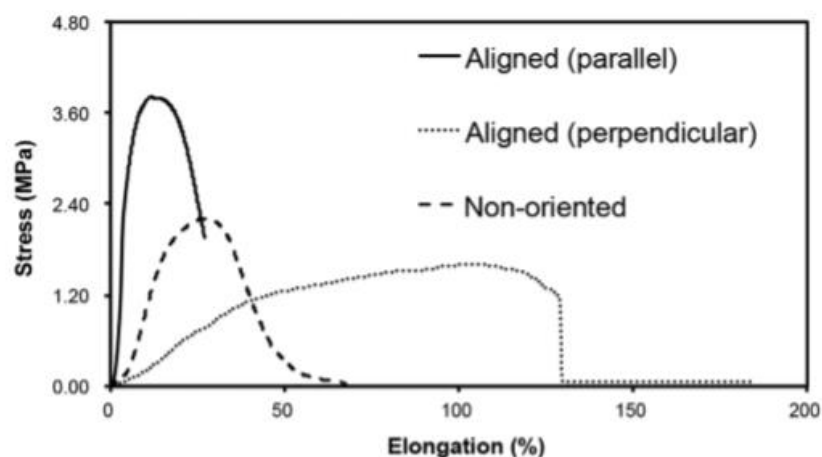


Figure 1.24: Tensile stress strain curves on Silk fibroin/PCL electrospun fibers. [134]

Scientists tried to perform mechanical characterization of a single electrospun fiber, unique component of larger fibrous membranes. Atomic Force Microscopy (AFM) is the most common technique used to measure mechanical properties of one fiber by 3 points bend analysis. Strand electrospun fibers of few different polymers were investigated with AFM technology. Baker et al. [135] determined the mechanical properties of individual PCL fibers with diameters ranging from 440 to 1040 μm founding an elastic modulus of 64 MPa. Properties of a single fiber, as the unique constitutive component of fibrous scaffold, might be a key identified parameter to predict mechanical behaviors of fibrous scaffolds. Ideally, mechanical response of a single fiber in a longitudinal direction can be correlated to a bundle of fibers (aligned scaffolds made by electrospinning).

1.4.3. Patterned membranes

The introduction of patterned structures has an important impact on the global mechanical behavior of electrospun scaffolds. This section will describe the modification in terms of mechanical properties of the architected membranes and develop the link between fiber organization and mechanical performance.

Patterned electrospun mats were successfully developed last decades thanks to the breakthrough of electrospinning technology. Most studies well described the morphology of the new fibrous constructs but they don't or barely explore their mechanical comporment.

Nevertheless, a few publications detailed the effect of structuration induced by 3D templates on mechanical properties reported in **table 1.4** [113], [118], [136], [137].

In most of these researches on patterned electrospun scaffolds, organization of the fibers induces a softening of the matrix. Vaquette et al. [138] showed that elastic modulus of PCL membranes decreases from 8 MPa (flat collector) to 2-5 MPa (patterned collectors). Mechanical properties of the patterned scaffolds seems to depend of the dimensions of wire and round collectors. A similar tendency of a weakening of the structured membranes was obtained by Neves et al. [137] and Kang et al. [139] , showing also a wider elastic zone, passing from 5 to 15 % for membranes produced on wire collector (Vaquette et al. [138]).

Specific dimensions of collectors can be related to mechanical behaviors of electrospun membranes. An improvement in mechanical properties (Young's modulus) is observed when the air gap between the wires decreases. Kan et al. [139] enhanced their Young moduli of Sc-PLA fibrous scaffolds from 375 to 445 MPa by reducing from 800 to 200 μm the space between wires. Vaquette et al. [138] improves in their PCL scaffolds the ultimate strain to failure from 140 % to 190 % when the diameters of round gaps decrease in metal collectors. For a value of 0.381 mm, Wang et al. [140] and Yan et al. [141] even observed mechanical strength superior to the random scaffolds, contradicting the first interpreted observation of membrane softening.

Complex mechanisms are involved in fibrous network but two opposite effects can be described from the experimental observations:

- Improvement of tensile properties due to the alignment of the fibers in well oriented areas. Higher stress can be contained if the load is applied in the same direction than the alignment of the fibers.
- An increase of porosity in low dense areas (centers of the mesh) which will decrease the global mechanical cohesion.

It has been reported than porosity tends to increase in electrospun membranes collected on 3D collectors [124], [138]. These areas with a lower fiber density will obviously exhibit weaker mechanical strength. Based on the work of Ashby and Gibson (1997) [142], [143] on the effect of porosity on

1.4. Mechanical properties of electrospun membranes

cellular solids, a simple model was defined and used for porous polymer scaffolds to correlate the Young modulus $E_{Scaffold}$ and its porosity ε as (see following **equation**):

$$E_{Scaffold} = E_0 \cdot (1 - \varepsilon)^n$$

E_0 the Young modulus of the material considered and n a constant. Vaquette et al. calculated a n value of 1.52 for electrospun PCL scaffolds. This relation thus explains that the main factor affecting mechanical properties in their study is the porosity of the scaffolds.

To conclude, the balance between the structuration (alignment of the fibers) and the increase of porosity in specific areas will determine the mechanical properties of the structured mat. In the case of a wire collector, as we decrease the gap air, we lower the amount of low dense zones. This might explain the increase of the overall tensile strength properties.

Structured mats often have an overall isotropic behavior as collector are repetitive symmetrical patterns. Neves et al. [137] cleverly produced an anisotropic fibrous scaffolds on a screw collector. Both longitudinal and transversal directions were mechanically investigated proving an anisotropic mechanical behavior. The anisotropic ratio, defined as the Young moduli ratio of the longitudinal over the transversal axis, was estimated as 3.33. The design of new anisotropic electrospun material can be a new asset for biomedical applications. Indeed, scaffolds need to mimic as close as possible the natural tissues, which exhibit pronounced anisotropic behaviors. Nowadays, it is crucial to develop new scaffolds with controlled mechanical properties in different directions.

References	Materials	Collector	Young's Modulus (patterned)	Young's Modulus (random)
<i>Neves et al (2007)</i>	<i>PCL fibers</i>	<i>Wire (1.5mm)</i>	<i>2 MPa</i>	<i>20 MPa</i>
<i>Wang et al (2009)</i>	<i>PCL fibers</i>	<i>Wire (0.381 mm)</i>	<i>63 MPa</i>	<i>44 MPa</i>
<i>Vaquette et al (2011)</i>	<i>PCL fibers</i>	<i>Wire (0.5-5mm)</i>	<i>1.7-4 MPa</i>	<i>8 MPa</i>
<i>Yan et al (2012)</i>	<i>PCL fibers</i>	<i>Wire (0.381/0.864mm)</i>	<i>5-10 MPa</i>	<i>9 MPa</i>
<i>Kang et al (2018)</i>	<i>Sc-PLA/10% fibers</i>	<i>Wire (0.2-0.8mm)</i>	<i>375-445 MPa</i>	<i>446 MPa</i>
<i>Neves et al. (2007)</i>	<i>PCL fibers</i>	<i>Screw collector</i>	<i>38 MPa (long.) 11 MPa (transv.)</i>	<i>20 MPa</i>

Table 1-4: Mechanical properties of structured electrospun scaffolds [137]–[141]

1.5. Conclusion

Advances in technology in medicine and recent tool developments for surgery places tissue engineering in the spotlight as primary therapy solution.

Regenerative medicine requires biomedical devices more and more efficient based on sophisticated biomaterials to interact with the human body. To replace in a better way natural tissues, tissue engineering requires a scaffold with tunable properties. Electrospinning is a promising technique to fabricate performant scaffolds made of an intricate nano or macro- fiber network. Polycaprolactone electrospun fibers possess all required properties such high porosity, good interconnectivity, suitable biodegradability and bioresorbability to substitute temporarily a missing part of natural ECM.

One remaining challenge is to organize better and master fiber deposition in electrospinning process. Nowadays, scientist successfully produce fibers with controlled fiber morphology. However, distribution of fibers at a macro scale is still not well mastered. Random collection of fibers in conventional electrospinning creates isotropic membrane.

Two main objectives in scaffolds structuration are to master fiber distribution in the xy plane and grow thicker mat in a controlled manner, i.e. with homogenous deposition in depth.

A promising way to organize fibers is the use topographical substrates as collectors. Alignment of fibers in one direction is now well mastered with rotating collectors. Patterned templates starts to be employed to spatially orientate the fibers in 2D dimensions.

2. Structuration of electrospun PCL membranes for soft tissue engineering

This chapter is dedicated to the development of structured PCL membranes by electrospinning. All of this study rely on the fabrication of fibrous scaffolds by template assisted method thanks to new designed tridimensional macro-structured collectors. The first part of this chapter is focused on the description of the electrospinning device, materials and optical characterization methods. Produced electrospun materials will be then presented, from random, aligned to patterned fiber mats. In each case, morphology of the fibrous scaffolds will be assessed with the help of optical and SEM image analysis.

2.1. Electrospinning

2.1.1. Polymer solution

Poly(ϵ -caprolactone) (PCL) was selected as electrospun material for this study. As detailed in **chapter 1**, this biodegradable polymer possesses numerous advantages for soft tissue engineering, especially when it is fabricated and turned into a nanofibrous network. Electrospinning of PCL polymer solution is relatively easy and quite-well documented in the literature (see **table 2.1**).

According to the previous work of Lancuski [144], [145], a blend of Dichloromethane (DCM) and Methanol (MeOH) with a volume ratio of 4/1 was chosen to dissolve the polymer. DCM is a good solvent for PCL and has a high volatility which allows a nice evaporation during electrospinning. However, it has a low conductivity (relative permittivity at 20°C of 8.93), property required to charge the polymer solution and initiate the jet in the fiber elaboration process. Methanol, in another hand, has a poor solubility with PCL but a high dielectric constant of 33. Thus the mixture of these two previous solvents will confer to the polymer solution a sufficient conductivity to smoothly electrospun fibers.

Poly(ϵ -caprolactone) (PCL) with a mean molecular weight of 80 000 g/mol⁻¹, Dichloromethane (DCM, ≥ 99.9 %) and Methanol (MeOH, >99.5 %) were purchased from Sigma Aldrich. All polymer solutions for electrospinning were obtained by dissolving PCL pellets in the two solvents blend DCM/MeOH with a ratio 4/1. Solutions were stirred with a roller mixer device for 24 hours minimum at room temperature in order to obtain a clear and homogeneous solution.

Polymer solutions with a concentration in a range of 8 to 16wt% were investigated. All solutions were successfully electrospun and produced macro-sized fibers. Average fiber diameter, porosity and pore size were greatly dependent of the solution concentration and ambient parameters of electrospinning. A solution of 16wt% was selected to produce PCL fibers because of its good electrospinning

replicability. The polymer solution is situated in the entanglement regime, closed to the upper limit of the electrospinning window. Polymer chains are sufficiently entangled to produce continuous fibers. Polymer concentration of 16wt% was found appropriate to obtain a steady polymer jet and bead-less fibers.

Two different PCL batches with same characteristics were purchased and used during the 3 years study: an old polymer, date of opening in *December 2010* (batch A) and a more recent one, date of opening in *May 2018* (batch B). Significant different results were observed in term of scaffold morphology for these two different batches. We define here the distinct batches so we can expose in the later sections clearly morphological and mechanical results in the following sections.

2.1.2. Electrospinning Set up

A vertical electrospinning apparatus as illustrated in **figure 2.1** was used to produce PCL polymer fibers. Set up consists of a syringe pump (model: KDS Legato 200, KD Scientific, Holliston, MA, USA) where the polymer solution will be expelled, a voltage source ($\pm 30\text{kV}$, iseq GmbH, Radeberg, Germany) and an attractive negatively charged collector. A 5mL syringe with a 21Ga metal needle tip was loaded with the polymer solution and a constant flow rate of 5mL/min was applied. Distance between the tip of the needle and the collector was adjusted at 20 cm and the applied voltage varied from 12 to 20kV.

Fibers were collected during 10 to 30 minutes on their templates to obtain different membrane thicknesses. Temperature and humidity were controlled in a confine environment of a protective Plexiglas cage containing the electrospinning device. Experiments were carried out at a temperature of 21°C and at a relative humidity adjusted between 40 and 60 %. Plane, rotating or micro structured collectors were used as negative electrode to fabricate random, aligned or patterned fibrous mats.

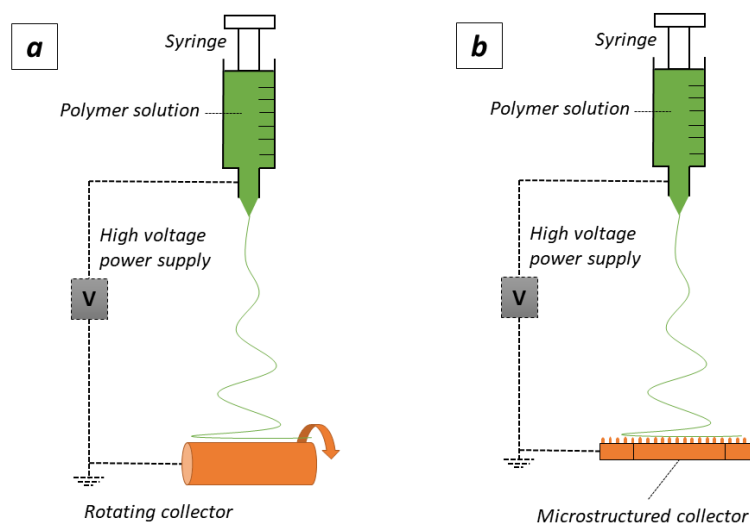


Figure 2-1: Electrospinning set up with (a) rotating collector and (b) micro-structured collector.

2.1.3. Characterization techniques

Optical microscopes (Olympus and Keyence) were used with transmission or reflection mode to observe scaffold micro-structures and assess local arrangement of the fibers. A field-emission–scanning electron microscope (FESEM ZEISS ULTRA55) was used to characterize the structure at the fiber scale. Fibrous samples were previously coated with a thin carbon layer by sputtering for SEM imaging. Fiber analysis (diameter and orientation) was performed with ImageJ software. Measurements over 100 different fibers were made to estimate the average fiber diameter (AFD).

2.2. Random fibers

Conventional electrospinning was firstly used to produce reference electrospun materials. Random fibers were fabricated on a plane collector with the above parameters of electrospinning. Morphology of random fibers is exposed in the SEM images of **figures 2.2**. Fibers are randomly deposited and fabricate an intricate network with no macro organization. Average fiber diameter was estimated at $3.7\pm 0.4\ \mu\text{m}$ from SEM images. Fibers shown in **figure 2.2.b** possess regular and smooth surface. Fiber are deposited on the top of each other, sometimes merging at their intersections (due to the remaining solvent when polymer jet reaches its final destination).

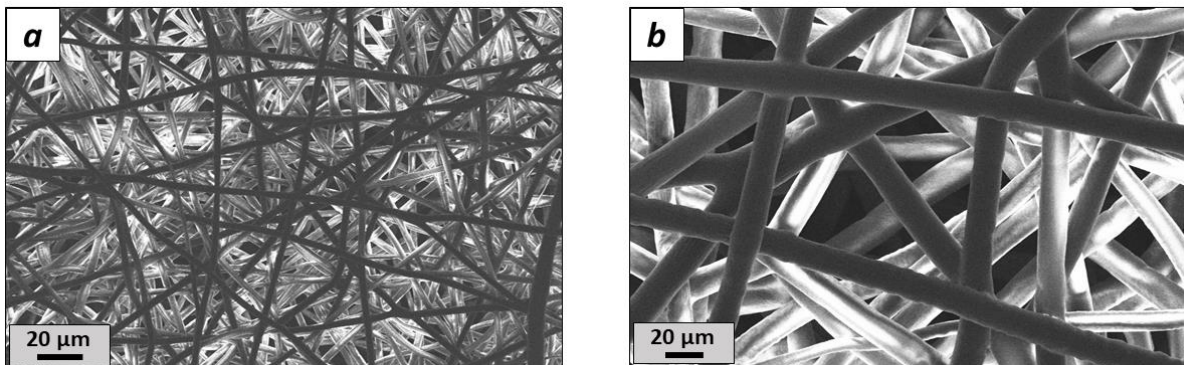


Figure 2-2: PCL fibers electrospun with a polymer concentration of 16wt% in DCM/MeOH (4/1) (500x (a) and 2000x magnification (b))

2.3. Aligned fibers

2.3.1. Rotating collectors

Two types of cylindrical collectors used in this study are illustrated in the **figure 2.3**. These collectors are made of a metallic tube of 10cm diameter with a length of 2cm (disk 1) or 25cm (disk 2). They are rotating at a constant high speed which can be set between a range of 1000 to 3000 rpm. Conductive contact is maintained by a soft metallic brush, assuring the conductivity of the mandrel surface during rotation.

The rotating device continuously collects and orientates fibers around the disk. Membranes were collected during 10 to 15 minutes to obtain a sufficiently thick membrane.

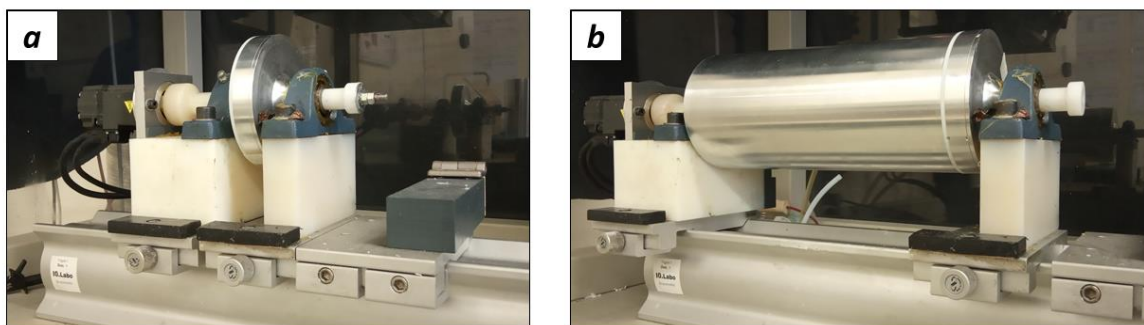


Figure 2-3: Rotating collectors: a) disk 1 (length = 2cm) and b) disk 2 (length = 25cm)

2.3.2. Average Fiber Diameter and degree of alignment

SEM images of the membranes were performed in order to evaluate the average fiber diameter (AFD) and the degree of fiber alignment. **Figure 2.4** shows aligned fibers obtained by the rotating disks with a short collection time (a few seconds). Fibers are elongated and stretched along the perpendicular direction of the cylinder.

Degree of alignment was clearly dependent of the length of collector disks n° 1 and n°2. A narrower distribution of orientation can be observed with the use of a short cylinder (n°2) as rotating collector (**figure 2.4.b**). This change in alignment quality is probably due to the reduction of the conductive surface. The smaller collector concentrates fiber deposition and limits the whipping effect of electrospinning. Bending instabilities of the jet are hindered by the rotational forces of the collector.

Moreover, air convection induced by the cylindrical rotation in the electrospinning cabin needs to be considered. Air flows provoke a quicker evaporation of the solvent at the needle tip, thus polymer cannot be pulled off by the electric forces and tends to form agglomerates. The phenomenon of air convection is obviously more important with the disk n°2 as a larger air volume is displaced at high rotating velocity. Excess of polymer had to be removed regularly with large disk n°2 in order to assure optimal spinning (i.e. until obtaining a Taylor cone with a unique polymer jet).

A slightly reduction of the average diameter (10 %) was observed with the collector n°2. Indeed, disk n°2 offers a wider surface collection resulting in a more perturbed whipping regime of the polymer jet. Consequently, fibers are more stretched and shrank during electrospinning, resulting in a smaller AFD.

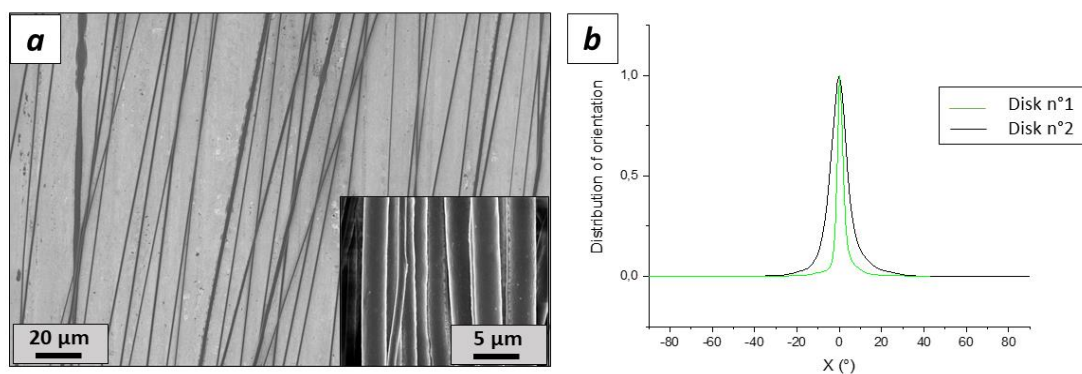


Figure 2-4: a) Aligned fibers collected on a metallic rotating mandrel (few seconds at 1900 rpm), b) Influence of collector size over fiber alignment (disk 1 & 2 at 1900 rpm)

Influence of the mandrel velocity was investigated and illustrated in the next **figure 2.5**. It can be observed that at low mandrel velocity (1300 rpm, **figure 2.5.a**), fibers are less orientated compared to higher collector speeds (1900rpm, **figure 2.5.c**). **Figure 2.5.c** shows the influence of rotational speed over distribution of fiber orientation. Broader distribution is obtained with low collector speed (1300 rpm). From 1800 rpm, it seems that orientation of the fibers reaches an optimal narrow distribution. No further improvements in alignment quality were observed from 1800 to 2100 rpm.

Average diameter of PCL fibers decreases drastically with the mandrel speed as illustrated in **figure 2.5.d**. Diameters of 3 μm were obtained with 1300 rpm, considered as a low rotating speed. Fibers have a collection mode similar to conventional electrospinning where rotational force disturbs only a little the trajectory of the jet. However, at high velocity, whipping instabilities are diminished by rotational forces. Consequently, fibers are stretched along the radial direction resulting in a smaller average diameter of 1 μm.

Aligned fibers (diameter of 1.1 μm) were produced at a rotating speed of 1900 rpm and selected for further investigations (cross section characterization and mechanical tests). Mandrel velocity was determined in order to ensure both a good alignment and fiber continuity. Indeed, at very high velocity, fibers could be overstretched leading to a complete rupture. Thus, considering the diagram of fiber orientation, an intermediate velocity of 1900 rpm was preferred rather than higher velocity.

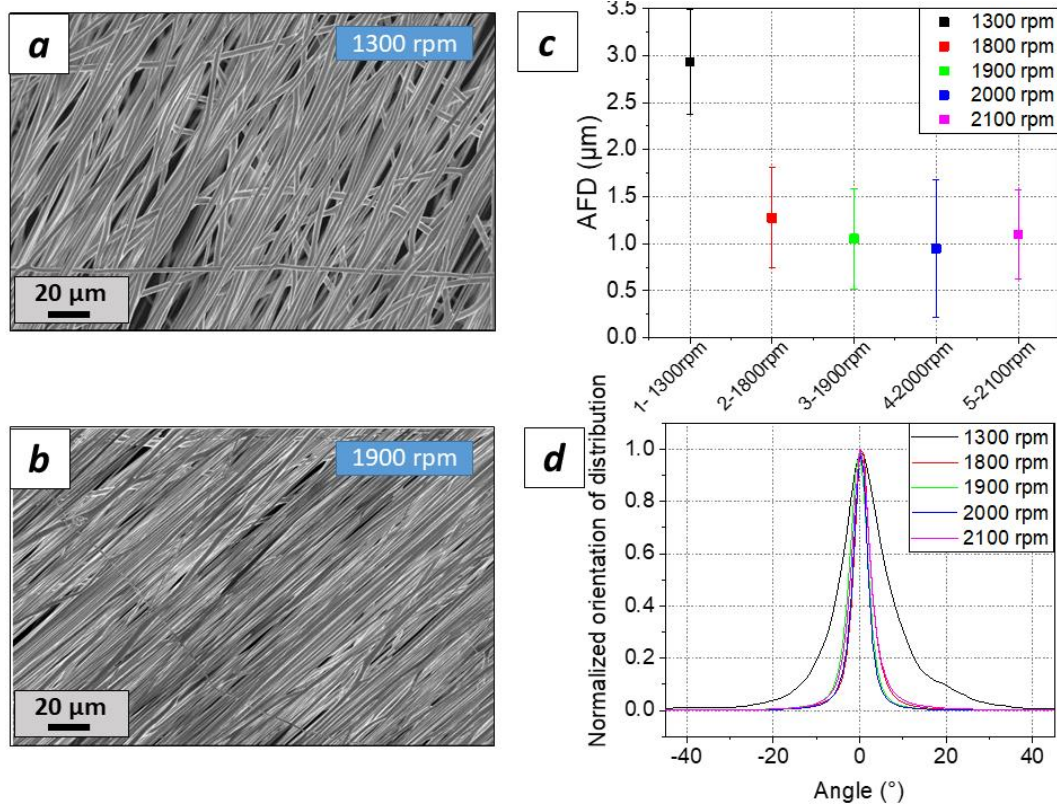


Figure 2-5: PCL aligned fibers a) 1300 and b) 1900 rpm, c) influence of mandrel velocity on average fiber diameter, d) distribution of orientation

2.3.3. Porosity assessment

Next section is focused on the analysis of a cross section of aligned fibers (rotating speed of 1900 rpm). Electrospun fibrous membranes were immersed and cut under liquid nitrogen in order to freeze the macrostructure. When temperature equilibrium was reached, cold sharp blades were used to cut perpendicularly the PCL fibers. A clean cross section of aligned fibers is shown in **figure 2.6.a**.

An accurate thickness of 138 μm was determined on the SEM image. With SEM clichés at higher magnification (x2000) (**figure 2.6.b**), porosity of aligned scaffolds was estimated. Considering that fibers are perfectly uniform and aligned, perpendicular section of fibers gives a relative surface density

similar to the volume density of the overall scaffold (volume occupied by the fibers). 10 SEM images were selected to evaluate fiber density in a 40x60 μm² image.

Following the equation below and by selecting average fiber diameter of 1.1 μm, porosity ε was calculated at 96 %.

$$\varepsilon = 1 - \frac{V_f}{V_t}$$

With V_f the volume occupied by fibers and V_t the total volume. It is important to keep in mind that two factors can over estimate this value of porosity. First, membrane cross-section is taken with a tilt, needed to observe separately the fibers. Thus, cross section surface might actually be smaller. Secondly, fibers are difficult to differentiate as they tend to agglomerate and form bundles. Errors may occur then to count and determine an exact number of fibers in the section.

Nevertheless this value confirmed the high porosity property of the produced scaffolds even though it is slightly superior to data of electrospun materials found in the literature (apparent porosity of 80 to 90 %) [22], [33], [146]–[150].

By measuring the mass of the aligned fibrous scaffold, porosity can be as well be estimated following the next equation.

$$Porosity (\varepsilon) = 1 - \frac{m/\rho_0}{V_t}$$

With m mass of the scaffold, ρ_0 the bulk density of PCL (1,145g/cm³).

A lower value of 86 % was found for the porosity of aligned PCL fibers which is closer to the experimental data found in others research works (results in agreement with literature as same employed method to measure porosity).

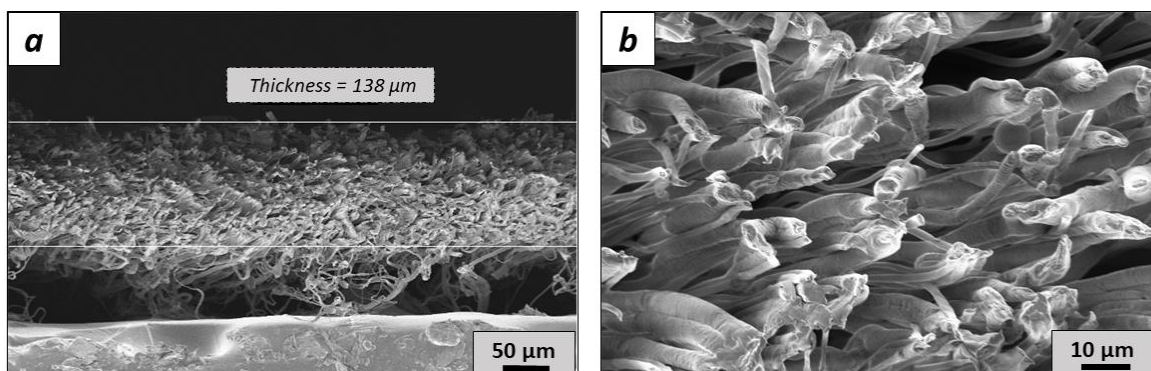


Figure 2-6: Cross section of an aligned PCL membranes (1900rpm, small disk n°1) with X500 a) and X2000 b) magnifications.

2.4. Structured membranes

Next chapter is dedicated to the development of structured membranes by electrospinning with tridimensional patterned templates. After describing the new collectors and their topographical features, morphological characterization of the scaffolds will be discussed for each induced architectures: honeycomb, square or rectangular patterns.

2.4.1. 3D collectors

Collectors with a specific surface shapes were designed to collect and arrange fibers during the process of electrospinning. They aim to replace conventional flat collectors and offer an uneven conductive surface where fibers will be attracted and gathered. Local electric field is going to be modified due to the protrusions arrangement. 3D topography of the negative electrode creates new attractive pathways for the fibers to follow.

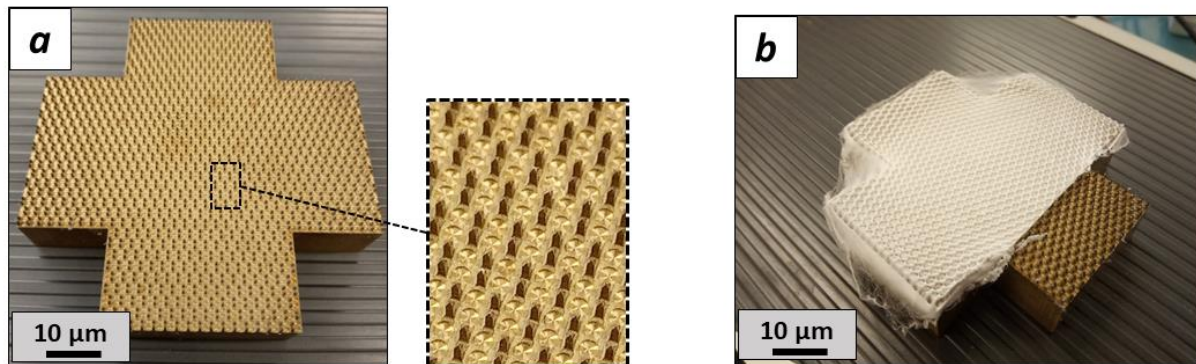


Figure 2-7: a) Micro-structured collector with honeycomb pattern b) Cut fibrous membrane collected on honeycomb type collector

A micro-structured collector with honeycomb pattern is illustrated on the **figure 2.7**. Such tridimensional metal collectors were fabricated by electro-erosion technique. They are composed of small metal peak arrays situated on the top of a brass metal cross (70 mm wide). Protrusions are disposed in a specific repetitive pattern. **Figure 2.8** lists the different mesh structures fabricated and used in this study: honeycomb, square, rectangular-1 and rectangular-2. Peaks are spatially organized with distances between the peaks ranging from 1 to 1.4 mm depending of the selected pattern. Protrusions are 1.5 mm high with a square base of 400 μm. Tips of the peaks were designed with a pyramidal shape in order to accentuate electrical pointy effect and improve the local modification of the local electric field. Ratio between the gap between protrusions and its height was carefully set

below 1 for the closest distances in order to avoid the deposition of fibers directly at the template bottom and obtain a fully suspended fibrous membranes (see **section 1.3**).

In this study, we will discuss and focus in more details on morphology and mechanical behaviors of honeycomb and square patterned scaffolds. Rectangular patterned scaffolds were successfully produced but no deep morphological and mechanical analysis were performed.

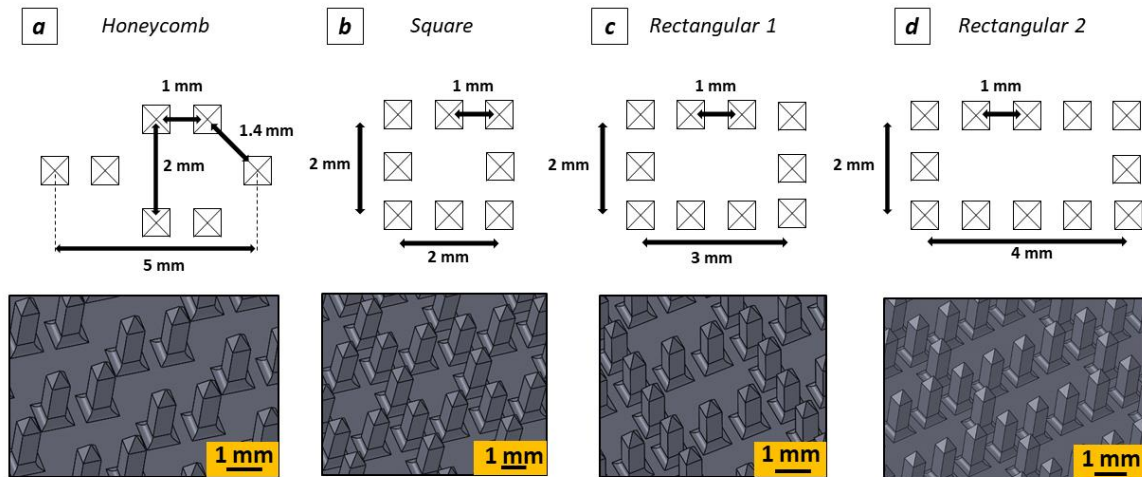


Figure 2-8- Micro structured collectors: a) honeycomb b) square, c) rectangular-1 and d) rectangular-2

2.4.2. Architected materials

The following section is focused on the micro-structured scaffolds produced by electrospinning with the help of the collectors previously described. Scaffolds with honeycomb, square and rectangular patterns were successfully fabricated by template-assisted electrospinning. Each section describes a membrane with a specific pattern, describing its macro structure and then morphology of the fibers.

2.4.2.1. Honeycomb patterned scaffolds

Macrostructure

Optical and SEM Images (**figures 2.9 & 2.10**) were performed to observe the structure of fibrous honeycomb membranes. Fibers (in white) are spatially arranged in a honeycomb pattern over a 7cm-wide metal cross. Fibrous mats were produced with high reproducibility adopting a similar shape than the 3D metal support as in several template-assisted electrospinning processes [151].

3 zones can be distinguished in **figure 2.9.b**: a dense area located at the corners of the honeycomb pattern ①, a zone between two peaks where fibers form bridges ② and ③, and a central low dense area at the core of the pattern ④ & ⑤.

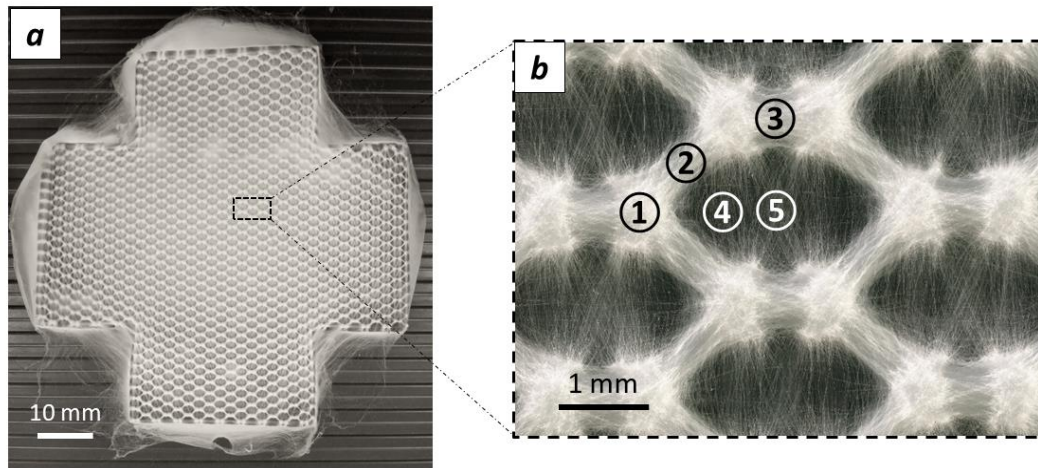


Figure 2-9: a) Electrospun membrane produced on honeycomb pattern b) Honeycomb structure of fibrous scaffolds

Figure 2.10 shows SEM images focused on each of the honeycomb parts ① to ⑤ (column i of **figure 2.10**). The first zone ① shown in **figure 2.10.1** is composed of randomly orientated fibers. The brightness of the zone on SEM images suggests that density of fibers is higher at the honeycomb mesh intersection. Between peaks (② & ③), aligned fibers are collected and form bridges (**figures 2.10.2** and **2.10.3**). Areas ④ & ⑤, respectively on **figures 2.10.4** and **2.10.5**, exhibit fibers with smaller densities. Nevertheless, a strong fiber organization is maintained in a cross shape.

With these non-flat collectors, electric static field is slightly disrupted, especially at the vicinity of the collector [120], [152]. Once fibers are close to the collector surface, they are electrically attracted to protrusions and preferentially accumulated on top of metal peaks. Continuous fiber jet will follow a preferential path to connect to the closest neighbor peaks it comes across. Fiber will move in accordance to the rigidity of the fiber (difficulty to bend fibers with an angle higher than 90) and deposit succinctly onto peaks. The fact that bridges ③ are wider than ② reinforces the deposition mechanism theory based on the electrostatic attraction. Peaks represent more attractive poles thus the fiber will be steered with higher probability toward the closest neighbor peaks. Only a few fibers are crossing the gap in the center of the honeycomb mesh which undoubtedly represents a longer distance for the fiber to overcome. A second hypothesis will consider the remaining charges accumulated by fibers and the electrostatic repulsion they create. As explained by Wittmer et al. [126], fibers in the center of the mesh have more difficulty to release the positive charges compared to the fibers situated on the peaks. Additional electrostatic repulsion forces will appear and guide new approaching fibers, resulting in a neat structuration.

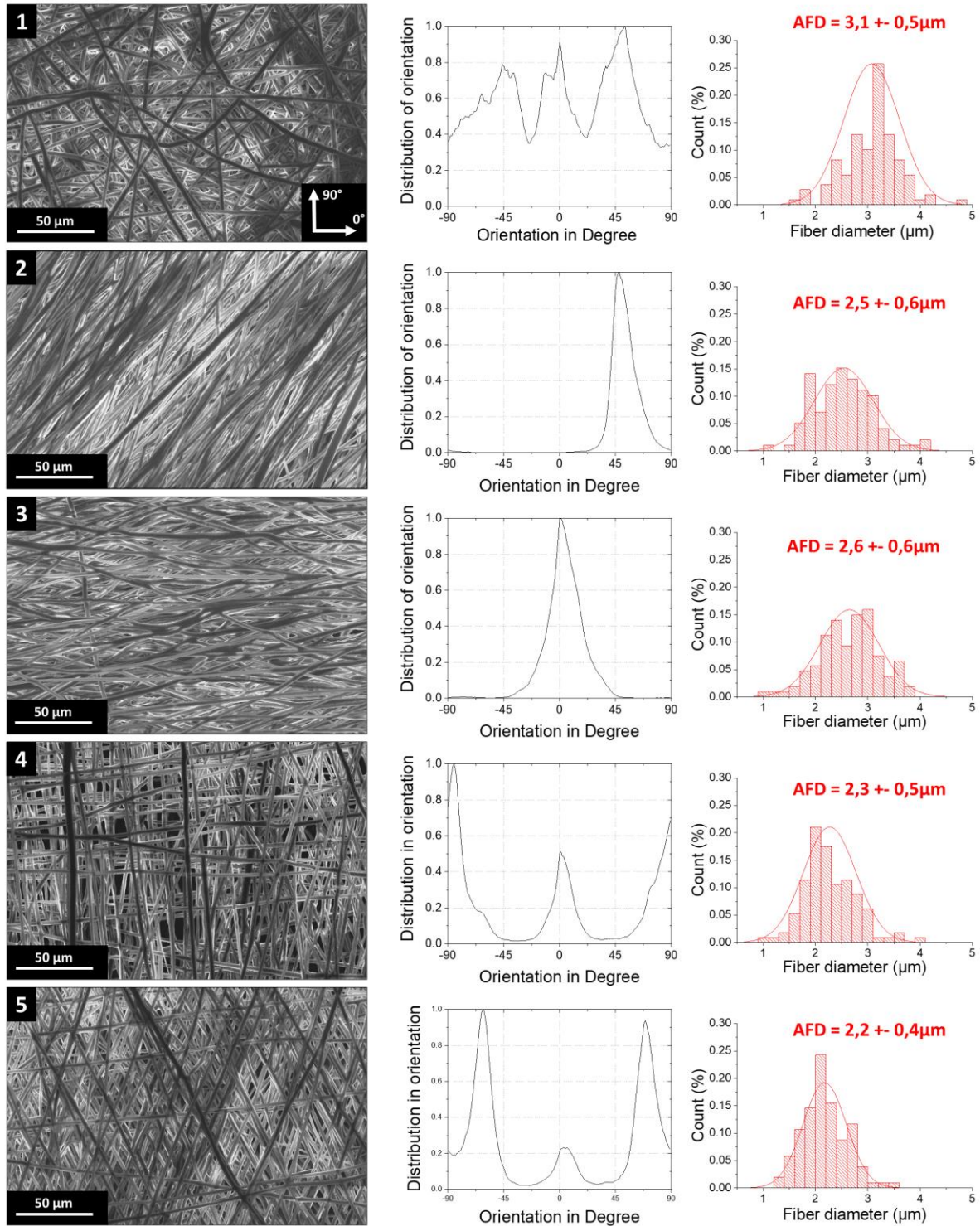


Figure 2-10: SEM images of honeycomb scaffolds with fiber orientation and Average Fiber Diameter measurements: ① high fiber density zone (collector peaks), ② & ③ fiber bridges, ④ & ⑤ center of the honeycomb mesh

Fiber morphology

Column ii of **Figure 2.10** shows fiber orientation distribution in areas ① to ⑤ of the honeycomb mesh. It is clear that fibers align preferentially along a unique direction for the bridges ② and ③ with a characterized orientation of 45 ° and 0 ° respectively. **Figure 2.10.1**, corresponding to the zone ①, reveals 3 main fiber directions at 45, 0 and -45 ° related to the geometry of the honeycomb pattern. More interesting is that even in the low dense areas, fibers are still highly orientated. As shown on **figures 2.10.4** and **2.10.5**, fibers are disposed along 0 and ±90° ④ or 0 and ±65° ⑤ directions. Alignment of fibers can be correlated to a similar process observed with a gap collection in electrospinning [72], [114], [153]. Fibers are aligned along one direction to form a bridge between two conductive protrusions.

Average Fiber Diameters (AFD) were analyzed through SEM images (column iii of **figure 2.10**). AFD is locally dependent, decreasing from 3.1 μm to 2.2 μm in the zone ① and ⑤ respectively. Fiber diameter could be related to void lengths between conductive protrusions. AFD in zone ② is higher than the ones in zone ③, ④ and ⑤, as the distance between peaks in ② is smaller. The smaller diameter is obtained in the center of the mesh ⑤ where the space between peaks is maximum. AFD is maximum in the dense zone ①, where fibers would be collected more randomly as on a flat surface (conventional electrospinning).

This fiber diameter gradient might be explained by the length of insulating gaps (here considering as the voids between peaks). Vaquette et al. [146] described in their experiences that AFD is affected by the void gap length in their wire collectors. Fibers elongate more as they have to make a longer path, resulting in a higher stretching and then in a lower fiber diameter. Another theory would rely on the non-regular morphology of the fiber during the deposition. Nedjari et al. [125] explain in their works that structuration in electrospun scaffolds is driven by the bimodal character of the fiber. Following this approach, thicker parts of the fiber, with more accumulated charges will be selectively attracted to the peaks and will compose the main bridges observed in our honeycomb meshes. Low diameter fiber parts would have no enough remaining charges and will deposit more randomly, filling the gaps of the honeycomb core.

Figure 2.11 reveals the heterogeneous topography of the 3D structured fibrous mats via a 3D profilometer scan (**figure 2.11.a**) and a SEM cross section view of the membrane (**figure 2.11.b**). Honeycomb scaffolds are produced here over a surface of 7 cm with an apparent thickness between 350 and 500 μm. As shown in **figure 2.11.c**, high thickness points are situated on protrusion as more fibers are attracted and gathered onto these locations. Lowest thickness parts of the membrane are located in the centers of the patterns. Z gaps between these high (zones ①) and low surface points (central zone ⑤) are evaluated around 250 μm in **figure 2.11.a**.

Fibers were spatially arranged over a 15 to 30 min time deposition without a loss of the microstructure that could be observed in several electrospinning cases with electro conductive templates [8], [154]. Current big challenge in electrospinning is to keep a well-defined fiber organization in depth. Indeed,

fibers are collected onto the support and start to create an insulating or repulsive layer growing with time. Patterned structures disappear after a few minutes of collection, corresponding to 100 μm layer of deposited fibers [12], [154]. As a consequence, fibrous samples with well-defined architectures are relatively thin, thus not easy to manipulate and perform subsequent tensile measurements with.

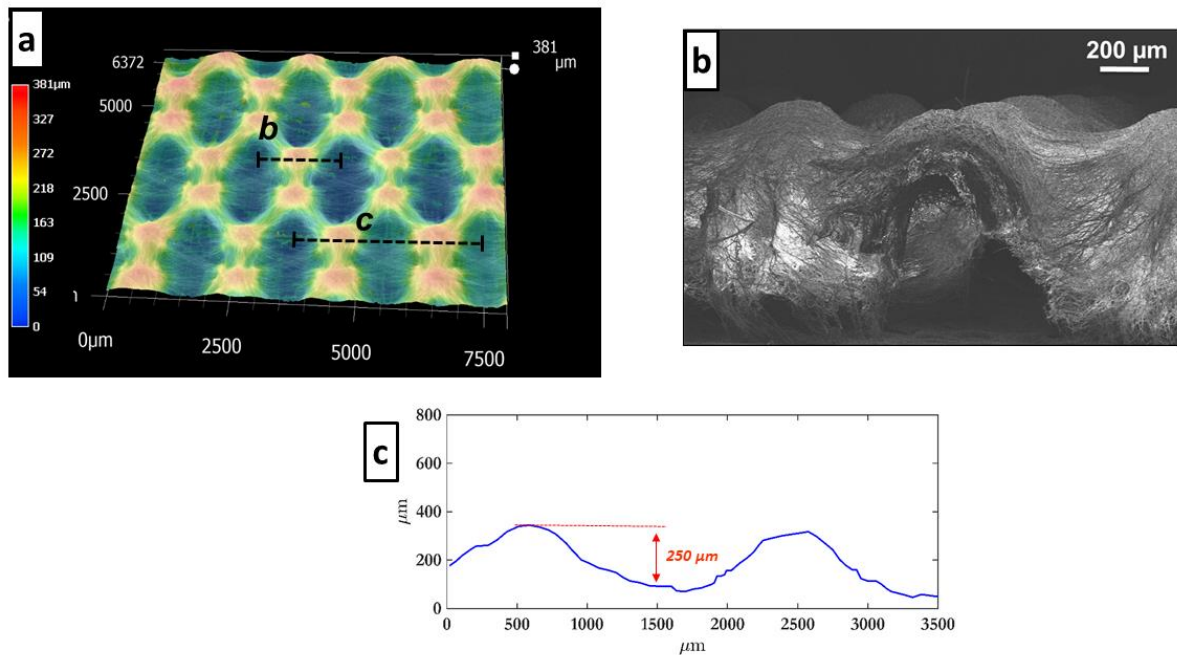


Figure 2-11: a) Optical profilometer scan of 3D honeycomb scaffolds, b) SEM image and c) profile graph of the membrane cross section

2.4.2.2. Square patterned scaffolds

The following section depicts electrospun scaffolds fabricated with square-type electro-conductive 3D templates.

Macrostructure

Fibrous membranes with square patterns were created over a cross template as shown in **figure 2.12.a**. Fibers reproduced the repetitive square mesh of the 3D collector and composed an organized fibrous assembly. On SEM image of **figure 2.12.b**, fibers in white are preferentially arranged onto or between protrusions, delimiting high and low fiber densities. Again 3 zones can be distinguished: collection areas ① & ② located on top of the peaks, ③ & ④ corresponding to fiber bridges and a centered low dense zone ⑤. Same selective deposition of the polymer filaments was perceived as in the case of honeycomb scaffolds.

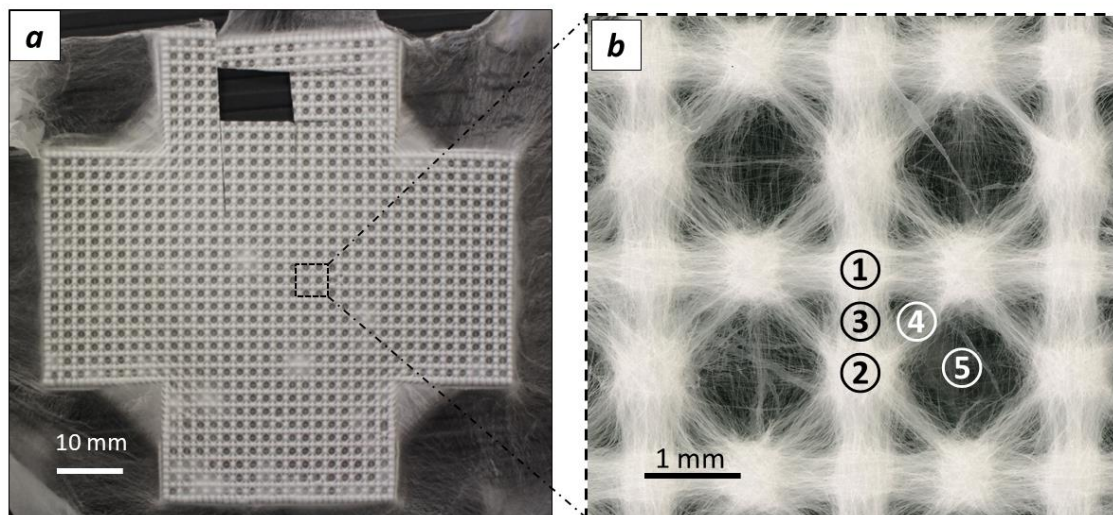


Figure 2-12: a) Electrospun membrane produced on square pattern b) Honeycomb structure of fibrous scaffolds

Fiber morphology

Distribution of fiber orientation is illustrated in column ii of the **figure 2.13**. Fibers are spatially organized along the sides of the square pattern. Over conductive protrusions, fibers are following a bimodal distribution of orientation: $0/\pm 90$ degrees for zones ① or $\pm 45/\pm 90$ degrees for zones ②. These directions indicate the lines that connect the closest peaks. Fibers, once attached to a protrusion, will be steered towards a next peak thus creating preferential pathways. In the case of middle peaks ②, two distribution peaks are broader and less distinct. Two main directions are separated with a smaller angle of $\pm 45^\circ$, thus fibers are less selectively distributed. Moreover, peak in ± 45 direction is smaller than the ones at $\pm 90^\circ$. This is probably due to the fact that next peak in this diagonal direction is a bit further (distance of $1.4\mu\text{m}$). Therefore, fibers will be less attracted along this $\pm 45^\circ$ axis compared to ± 90 degrees axis.

In zones ③ and ④, fibers are connecting peaks and form bridges. A single orientation of $\pm 90^\circ$ or $\pm 45^\circ$ is observed for areas ③ and ④ respectively. Mesh core presents two characteristic orientations at 0 and ± 90 degrees which correspond to fibers crossing the gap and linking the sides of the square pattern.

Diameters were measured with the help of SEM images of square fibrous membranes (column iii of **figure 2.13**). Average fiber diameter is locally dependent. Dense zones ① and ② contain large fibers (AFD of $3.6\mu\text{m}$) whereas bridge and center areas have a lower average fiber diameter of $3.5\mu\text{m}$ and $3.1\mu\text{m}$ respectively. As in the honeycomb structure, AFD is higher on conductive protrusions. For bridges (③ and ④) and square center ⑤, difference in size could be related to the gap distance separated the conductive peaks. The larger the space between protrusions is, the smaller the value of AFD is.

It can as well be noticed that AFD is slightly higher in square compared to honeycomb-patterned scaffolds ($3.6\mu\text{m}$ versus $3\mu\text{m}$). Complex phenomena are involved in fiber stretching and deposition on micro-structured collectors. Final fiber morphology seems to be dependent of the protrusion patterns of the collectors. Maybe dimension of the niche size of each pattern influences fiber trajectories, resulting in a better fiber structuration. Honeycomb “void” gap is slightly larger (3mm) in one direction. Thus fibers are differently deposited and endure more bending (leading to a global average fiber diameter a bit smaller).

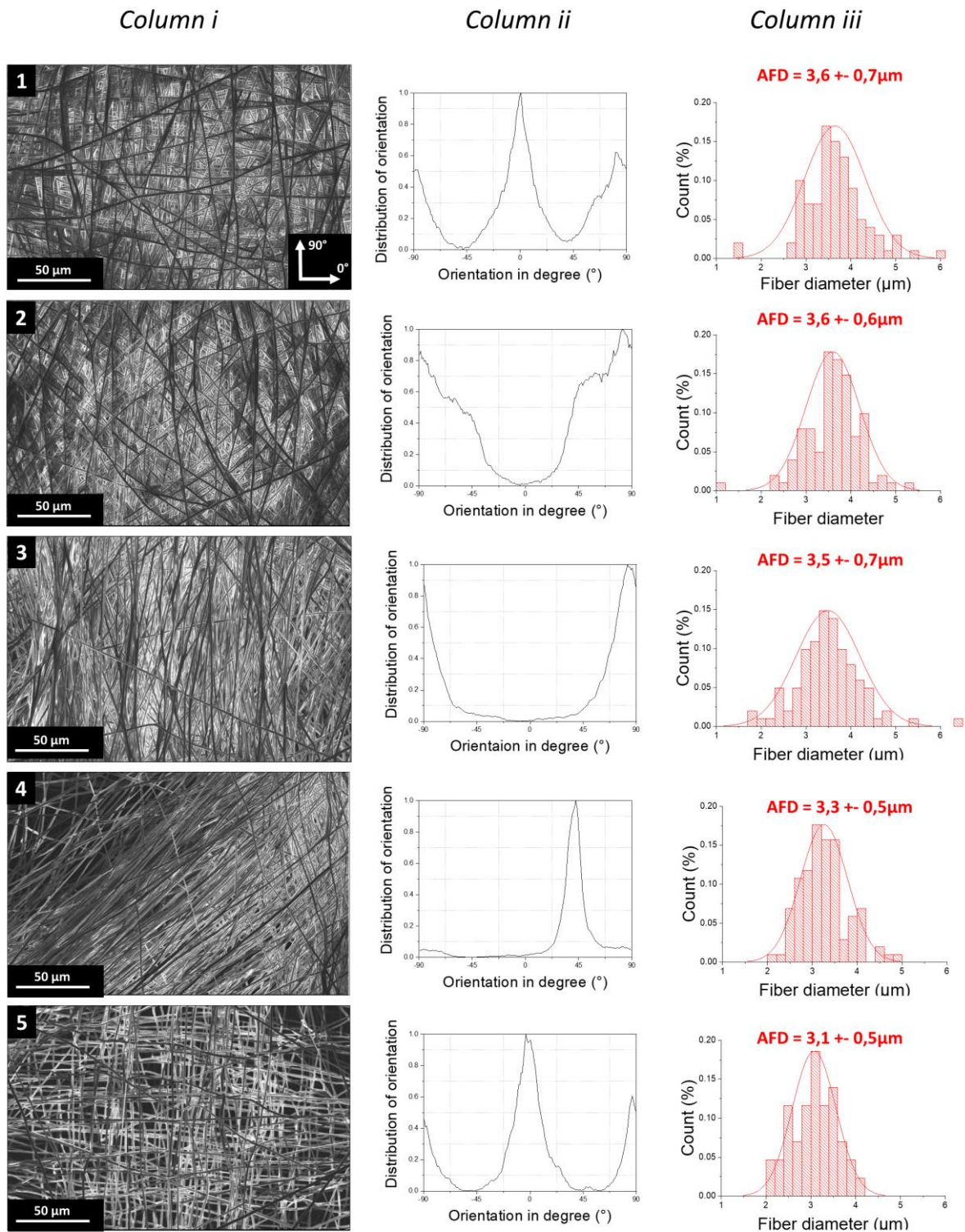


Figure 2-13 – i) SEM images of square scaffolds with ii) fiber orientation and iii) Average Fiber Diameter measurements: ① & ② high fiber density zones (collector peaks), ③ & ④ fiber bridges, ⑤ center of the mesh

Figure 2.14 illustrates the tridimensional structure of square patterned scaffolds. A digital z profile was performed on square patterned scaffold shown on **figure 2.14.c**. Z gaps or relative z positions between different zones are evaluated. An average apparent thickness of square patterned scaffolds illustrated in **figure 2.14** is estimated around 600 μm . It is important to note that last measure is not precise as the optical device detect only the surface on the fibrous mat. Moreover soft membranes are not strictly plane and do not necessarily rest perfectly on the microscope substrate.

Relative height between bridges ③ and peaks ① & ② is ranging from 100 to 160 μm . An average value of 150 μm was selected for later numerical models (square mesh reconstruction, **chapter 4**). Fibers bridges in zones ④ were estimated at a thickness of 100 μm .

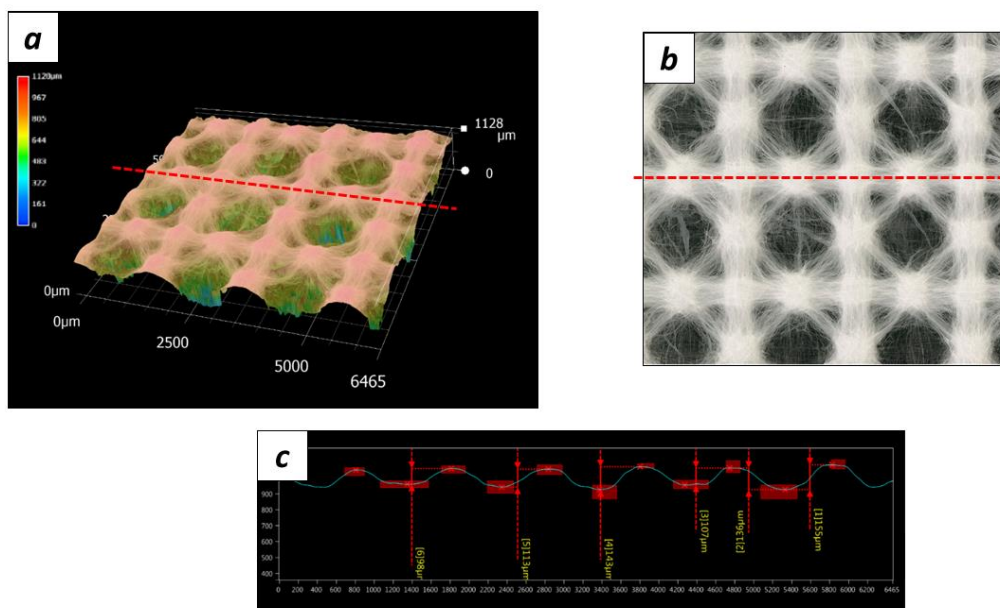


Figure 2-14: a) Optical profilometer scan of 3D square scaffolds, b) SEM image and c) profile graph of the membrane cross section

2.4.2.3. Other shaped scaffolds

Figure 2.15 displays electrospun scaffolds with different patterns: rectangular mesh 1 (**figure 2.15.a**) or rectangular mesh 2 (**figure 2.15.b**) and a more complex square-honeycomb pattern (**figure 2.15.c**). Fibers are selectively disposed on protrusions, forming bridges between conductive peaks as in the honeycomb and square structures. Various areas are created leading to organized 3D constructs with low and high porosity areas. These new shaped morphologies illustrate the potential of the method. Simple or more complex patterns can be replicated and create electrospun structured mats. By designing and adjusting protrusion dimensions and distances between them, fibers will gather, align in selective areas and mimic micro-patterns.

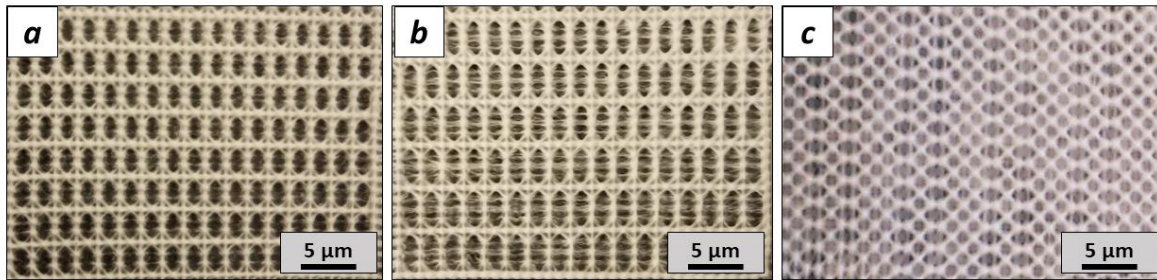


Figure 2-15 – Other architected scaffolds produced with micros-structured collectors by electrospinning a) rectangular-1 pattern b) rectangular-2 pattern and c) honeycomb-square pattern

2.5. Conclusion

Fiber structuration in an electrospinning process was successfully performed with the help of new 3D designed collectors. This study highlights the fabrication of fibrous scaffolds with honeycomb, square or rectangular patterns adapted for tissue regeneration applications.

Fibrous scaffolds can be easily shaped, reduced or expanded by designing new collectors and/or using scale-up electrospinning methods (multi spinneret, needless electrospinning, motorized collectors, etc.).

Only limited thicknesses are nevertheless obtained by this method (loss of structuration after a few minutes of collection). Still, produced membranes are a few hundred of microns thick, which offers numerous applications for tissue engineering (protective, filtration membranes, skin regeneration, bandage, vascular tissue engineering or guided tissue regeneration (GTR)). A multilayer approach can be as well considered to overcome the problem of thin thickness. Several electrospun membranes can be assembled together in order to create a thicker mat and respond to scaffold requirements.

This method brings a new way to build organized heterogeneous materials for tissue regeneration. Structured membranes offer two distinctive fibrous zones that could create attractive structural environment for cells. Indeed, dense areas would confer required mechanical strength to the global framework. Network of bundles made of aligned fibers can be monitored in order to obtain mechanical properties specific to soft tissues. Besides, low dense zones with apparent lower porosity would provide a favorable environment where cells could penetrate in depth and proliferate.

3. Characterization of the mechanical behavior of electrospun architected scaffolds

*The structured electrospun membranes described in the previous **chapter 2** were mechanically characterized. To this end, uniaxial tensile tests with a local deformation monitoring were carried out on honeycomb and square patterned scaffolds.*

The first section of the next chapter describes tensile sample preparation and the general methods of mechanical characterization tools employed. Secondly, a set of experiences is detailed to analyze influence of the sample dimension, relaxation and cyclic behavior of the materials. Finally, experimental results of monotonic tensile tests are exposed, starting with investigation of random, aligned and patterned scaffolds. For the patterned structures (honeycomb and square), a focused analysis of local strains during elongation was carried out.

3.1. Tensile test Set-up

3.1.1. Sample preparation

Samples for tensile tests were extracted from the 70 mm wide membranes produced by electrospinning. Electrospun membranes are usually very thin and thus delicate to manipulate. This is especially the case for patterned electrospun scaffolds where fibers tend to be deposited with less organization after a few minutes of collection. Softness of electrospun membranes makes sample cutting sometimes challenging as these light materials are very sensitive to air convection or electrostatic forces. Two methods to obtain the tensile samples were investigated: blade and laser cuttings.

Figure 3.1 illustrates cross sections of PCL aligned in the case of blade cutting, with the help of a sharp razor blade or scissor. Cutting is performed on the sample either at a frozen state or at room temperature. **Figure 3.1.a** displays a sliced PCL membrane where fibrous materials were immersed and cut in liquid nitrogen. A clean section appears where inside morphology of aligned fibers remains intact. **Figure 3.1.b** shows a cross section for the cutting performed at ambient temperature. A more degraded morphology is observed when the incision occurred at ambient temperature. In this case, fibers are extremely deformed by the compressive action of the blade, PCL fibers being soft and easily deformed. In this case, fibers are merging together and form a continuous line of agglomerated polymer (**figure 3.1.b**). The micro structure is then deeply affected at the rectangular edges of fibrous samples.

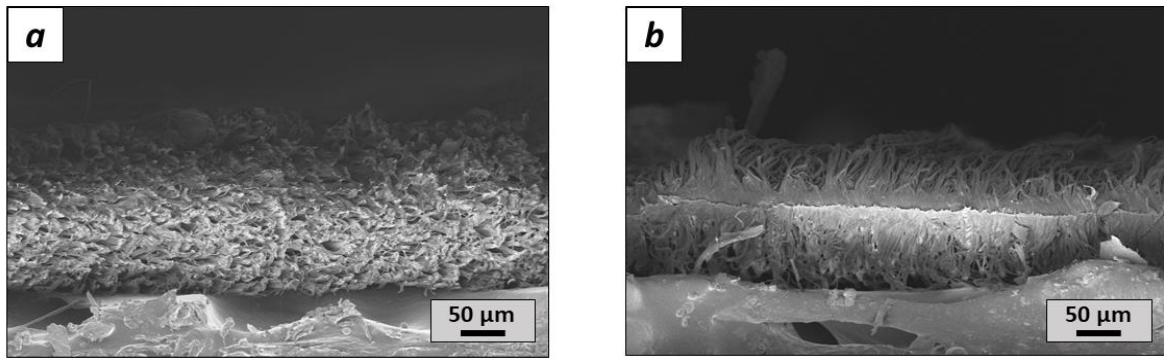


Figure 3-1: Cross section of aligned electrospun fibers cutting (a) under liquid azote (b) at ambient environment

Laser cutting was then investigated as an alternative shaping technique for our fibrous scaffolds. A laser cutting device (Trotec, Speedy 300, CO₂ laser [10-120 Watts]) was used to shape regular fibrous sample with a controlled intensity of the laser beam light. Even with a low beam intensity and a slow repetitive displacement, morphology of the fibers was deeply affected. As shown in the SEM images in **figure 3.2**, fibers are locally melted after laser exposition. Square patterned scaffold loses its fibrous structure especially at the peak area shown in an enlarged image in **figure 3.3.b**. A continuous polymer melted region is spreading over the all thickness of the sample.

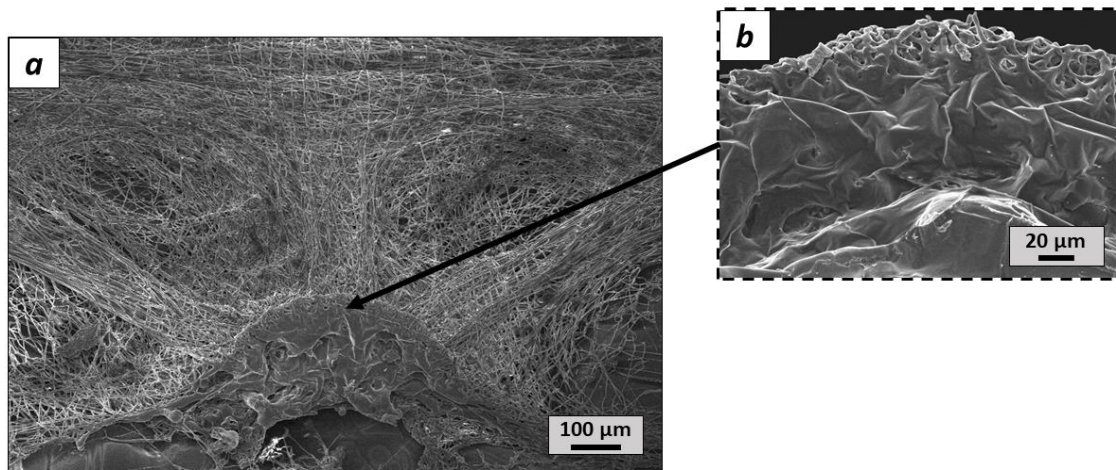


Figure 3-2: SEM images of (a) square patterned scaffolds obtained by laser jet cutting device (b) melted surface of PCL polymer fibers.

In both cases, morphology of the fibers is deeply affected by cutting procedures. Cutting under liquid nitrogen which offers an optimal morphology conservation was difficult and time consuming to implement to all samples. Thus, mechanical cutting at ambient temperature was preferred over laser

as fibers were less damaged in first configuration. The primary solution of cutting membranes with a sharp blade at ambient temperature was finally selected for all mechanical samples.

Samples having rectangular shapes were cut from the cross-shaped membranes as shown in **figure 3.3.a**. Size of tensile specimens was defined at a surface of 30x70 mm². In order to avoid local damage of the scaffolds that could be induced by the grips of the tensile machine, small strips of paper tape were stuck on both sides of the sample (**figure 3.3.b**). Initial gauge length (H_0) was set at 30 mm as shown in the **figure 3.3.c**. Length (H) and width (l) dimensions were carefully selected in order to have a ratio (H/l) superior to 3 to reduce grip effects.

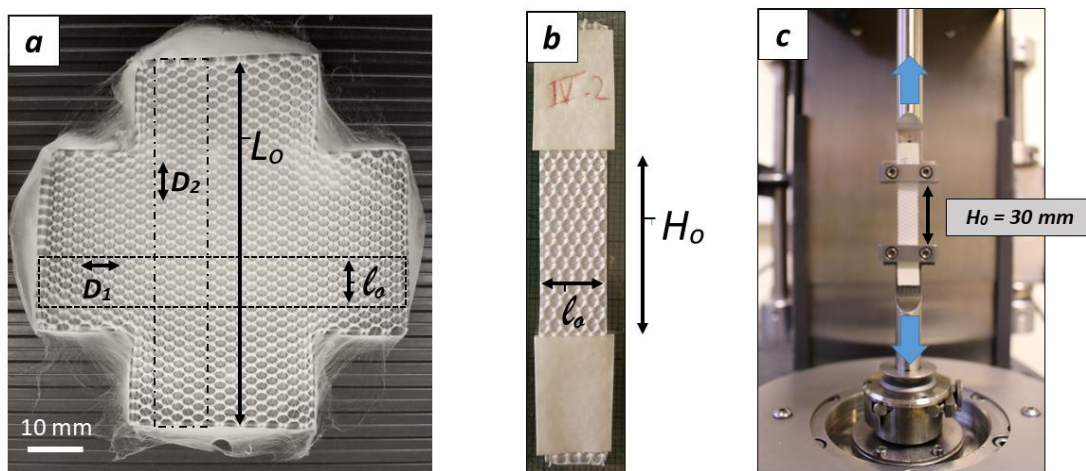


Figure 3-3: (a) Mechanical samples extracted from cross-shaped electrospun membranes (b) mechanical sample with paper tape (c) fibrous sample held in the grips of the rheometer

Loading directions need to be defined as the studied scaffolds are patterned and do not possess always an isotropic behavior. **Figure 3.4** details loading directions for square and honeycomb scaffolds. Square samples were pulled along one longitudinal direction D_1 and another D_2 set at 45 degrees. Honeycomb scaffolds were pulled along longitudinal D_1 and transversal D_2 directions as illustrated in **figure 3.4.b**.

Characteristic distances between peaks (a, b, c or d) were defined to assess the deformation of elementary patterns in both cases. It has to be noticed that the elementary square cell has a width of $a=b=2 \text{ mm}$ whereas the honeycomb mesh size is larger ($c=2 \text{ mm}$ and $d=4 \text{ mm}$).

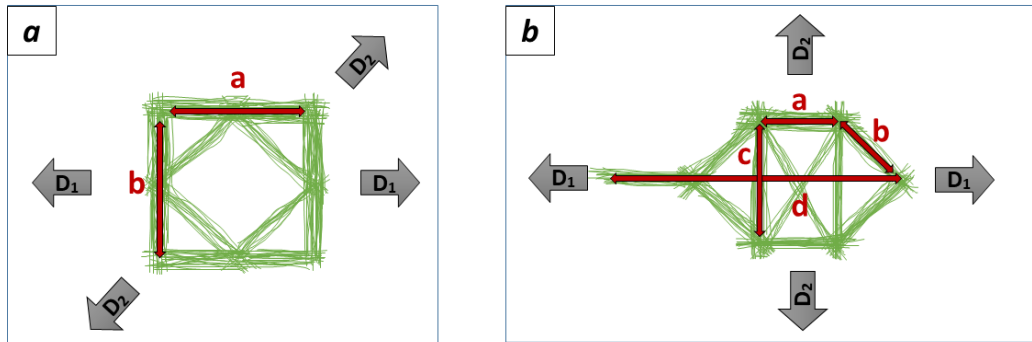


Figure 3-4: Elementary patterns of square (a) and honeycomb (b) scaffolds with loading directions D_1 and D_2

3.1.2. Uni-axial tensile test equipment

Uniaxial tensile tests were carried out with an ARES-G2 rheometer (TA Instruments, New Castle, DE, USA) or MTS tensile machine (Series 40 Electromechanical Universal Test Systems) shown in **figure 3.5**.

ARES G2 is equipped with a load cell of 20N (0.001 N precision on Axial force measurement) and a positioning accuracy of 0.1 μ m. A load cell of 25N was installed on the MTS device which confers to the system a precision of 0.1 N in axial force measurement (position accuracy of 0.4 μ m). MTS Machine was used to perform additional uniaxial tensile tests. Indeed, available wider grips allowed us to test samples with larger width (see next **section 3.2**). However, measurement accuracy with MTS machine was lower resulting sometimes in an acquisition of noisier stress-strain curves. ARES G2 was mainly used for all tensile tests due to its high precision.

Samples were placed into two axial clamps and then stretched along one direction at a speed of 0.1mm/s. A constant cross head velocity was applied and the axial force F generated by the load was measured every 0.1 second.

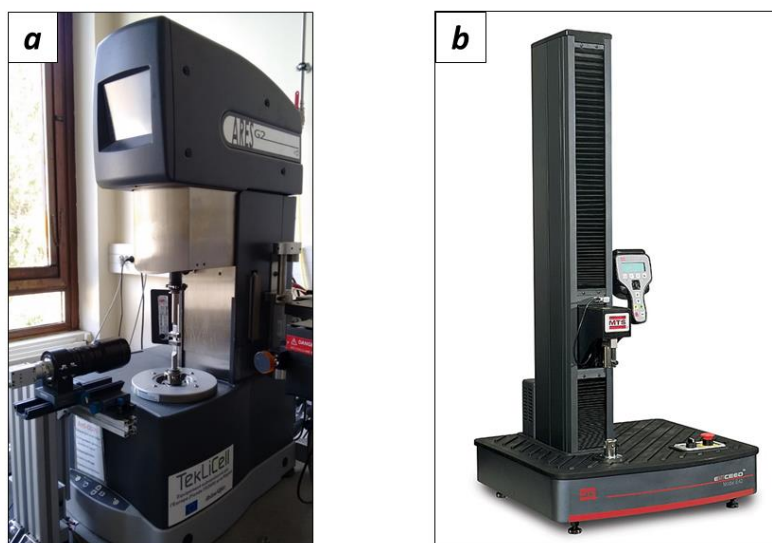


Figure 3-5 – Apparatus for axial tensile tests: (a) Rheometer ARES G2 with camera control (b) MTS exceed tensile machine

3.1.3. Local-deformation monitoring

A camera (Basler acA2000-50gm) was installed on the tensile stress measurement bench with a motorized device allowing a vertical motion. The objective was to follow the local deformation of a few patterns at the center of the sample during elongation. Optical device was then displaced at a constant speed exactly equal to half the crosshead velocity. Consequently the same central zone of the sample was observed to evaluate local strains.

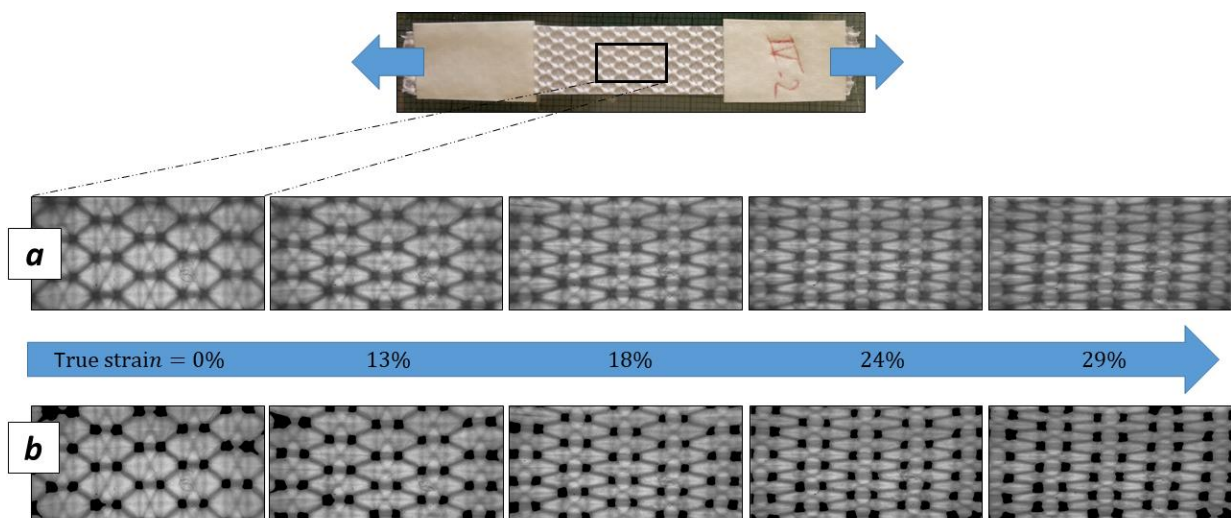


Figure 3-6: Sequence of images obtained during elongation (line a) with characteristic points detection (line b)

Line A of figure 3.6 shows the sequence of 5 pictures obtained by a camera with transmission mode corresponding to a global true strain $\ln(H/H_0)$ of 0, 13, 18, 24 and 29 %. A light source was placed behind the sample during elongation in order to improve contrast. Fiber patterns are recognized as the dark area as light crossed more matter (polymer fibers) before reaching the camera sensor. Characteristic points of the pattern were defined, as shown in line B of **figures 3.6**. These characteristic points are zones of high fiber density. They were tracked with a post treatment processed by image J software. In short, images were first binarized, revealing a black and white mask of the dense fiber zones. Then sequence of images was treated with median filters and an opening process which consists in successive iterations of erosion and dilation operations. The result is a selective filtering of the peak zones illustrated in **figure 3.6 (line b)** by the superposition of optical images and masks.

From the sequence of binary masks, x and y positions of each characteristic point were determined by a tracking mass center computation. Final tracking of the mesh characteristic points is illustrated for

the honeycomb and square scaffold in **figures 3.7.a and 3.7.b**, respectively. Trajectories are plotted for a stack of 300 images, corresponding to 300 s or 70 % of global true strain.

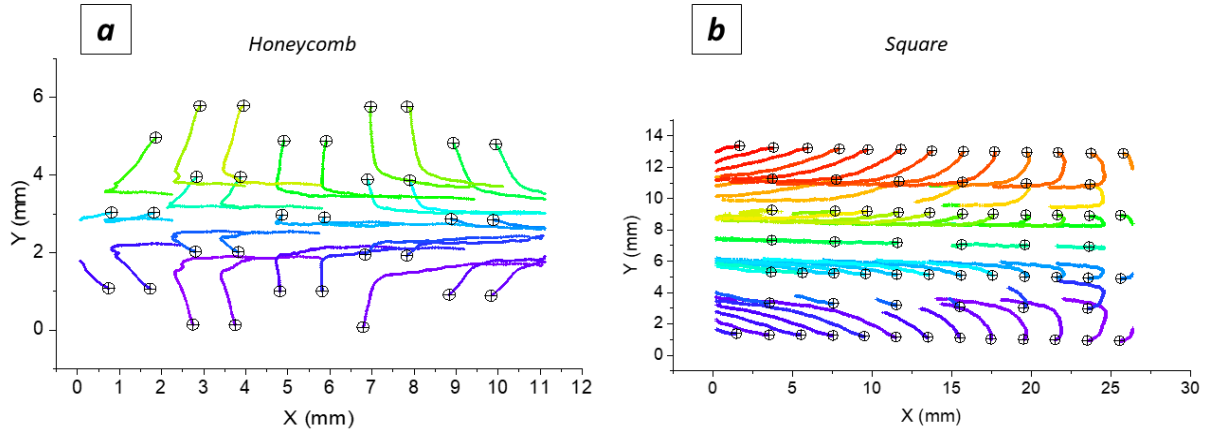


Figure 3-7: Tracking of characteristic points of honeycomb (a) and square (b) scaffolds meshes

As soon as actual positions of characteristic points for each set of images are determined, distances between characteristic points were easily calculated as a function of time, which allowed to calculate local strains. Depending of the loading direction, transversal and longitudinal local strains were computed (more details in local true strain **section 3.1.5**).

3.1.4. Determination of nominal Stress

Nominal tensile stress (or engineering or first Piola-Kirchhoff stress) was calculated from axial force F and the initial surface of the cross section (S_0) as described in **equation 3.1**:

$$\text{Nominal Stress} = \frac{F}{S_0} \quad (3.1)$$

3.1.4.1. Difficulty to measure 3D membrane thickness

Produced patterned membranes exhibit a non-regular topography as they are composed of a tridimensional fiber network. High porosity, softness and consequently high contractibility of electrospun mats make the measurement of an accurate thickness tricky. Conventional micrometers usually apply a force from 5 to 10 N on small round surface (diameter of 5-6mm), compressing the soft electrospun membrane that underestimates the thickness of samples.

Figure 3.8 illustrates the softness of electrospun patterned scaffolds. A compressive test was performed using a parallel plate geometry (20mm in diameter) placed at the center of a honeycomb scaffold (**figure 3.8.b**). A slow displacement at constant velocity was applied (gap starting from 2mm). Axial force was measured with high precision rheometer (HAAKE MARS III Thermo Scientific, normal force resolution of 0.001N). On the graph in **figure 3.8.a**, it can be observed that axial force increases abruptly as soon as the disk reaches the membrane (around 700 μm). If a maximal axial force of 0.1N is set, a thickness value of 640 μm is measured compared to 395 μm for a value of 5N. Considering that the real thickness value is obtained with a value of compressive force of 0.1N, a relative error of 38 % is made by measuring with an applied force of 5N.

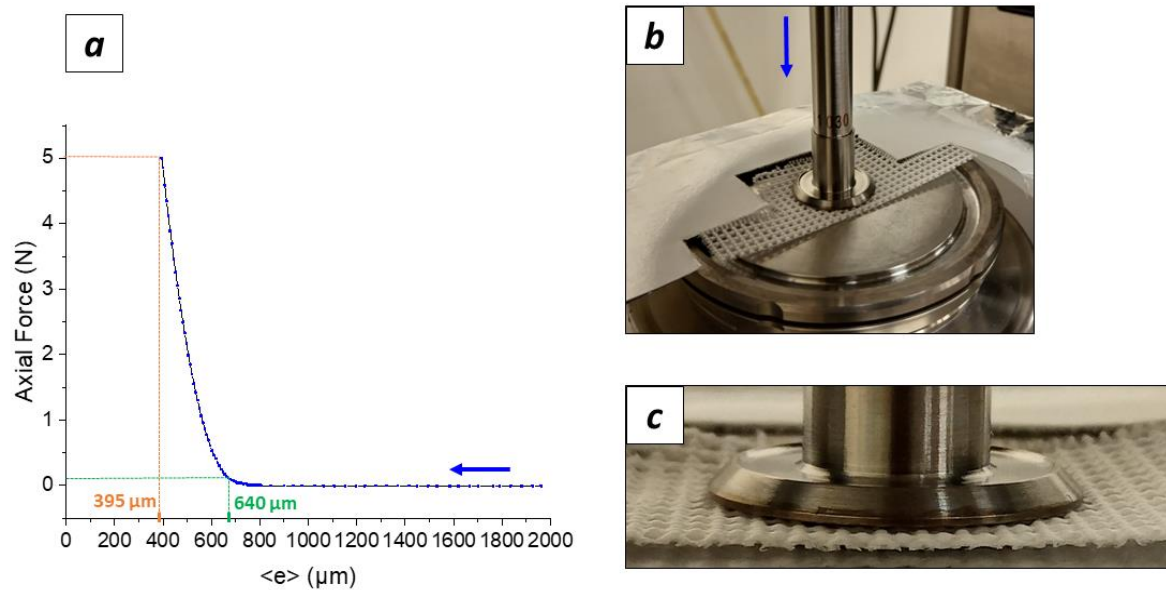


Figure 3-8 – Thickness measurement of square patterned membrane with a compressive force test (MARS rheometer): (a) Axial force applied vs gap $\langle e \rangle$ between geometry and flat support, (b) and (c) square patterned membranes compressed on MARS rheometer.

3.1.4.2. Estimation of nominal stress

Previous paragraph shows that membranes produced by electrospinning exhibit a strong irregular profile (cf. optical profilometers in **chapter 2**) that makes the determination of an accurate thickness delicate. However, this parameter is required to determine the nominal stress $\sigma = \frac{F}{l_0 \langle e_0 \rangle}$ of the membrane tensile test (with F the measured axial force, l_0 the initial width and $\langle e_0 \rangle$ the initial apparent thickness of the sample).

An alternative method is proposed in this study by measuring sample mass m which can be expressed as:

$$m = \rho (1 - p) L_0 l_0 \langle e_0 \rangle \quad (3.2)$$

where ρ denotes the bulk density of PCL (1.145 g/cm³), p the porosity and $L_0, l_0, \langle e_0 \rangle$ the initial dimensions of the fibrous sample.

The nominal stress can thus be calculated as:

$$\sigma = \frac{F L_0}{m} \rho (1 - p) \quad (3.3)$$

where F is the measured axial force, m the mass and L_0 the initial length of the sample. The parameter $(1-p)$ was experimentally calculated with a first sample, either square or honeycomb. Porosities were estimated to a value of 97 % for honeycomb scaffolds and 95 % for square patterns. To apply this method, porosities in all the patterned type-membranes are considered identical. In this manner, we introduce a way to compare patterned samples with a mass measurement which was found experimentally more accurate than measuring apparent thickness $\langle e_0 \rangle$ of the sample.

Figures 3.9. Illustrates the benefits of the new employed method to assess nominal stress. Two different samples of square patterned scaffolds were mechanically tested and nominal stresses were plotted with **equation 3.1** (**figure 3.9.a**) and with **equation 3.2** (**figure 3.9.b**). It can be noted that measures with sample mass clearly expose a better fitting (**figure 3.9.b**). This approach used to estimate average thickness is also less intrusive than applying a mechanical pressure. In this case, rectangular membranes are non-damaged by a mechanical micrometer prior to tensile tests.

Nominal stresses of all electrospun membranes were thus computed using **equation 3.3**.

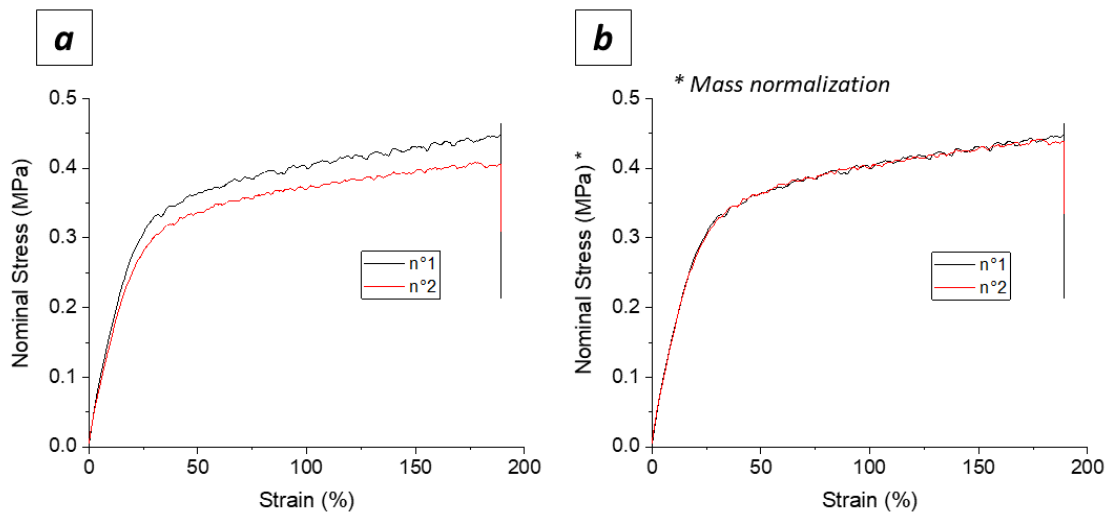


Figure 3-9: Nominal stress of square patterned membranes a) before and b) after mass normalization

3.1.5. Definition of global and local strains

Local strains of the patterned scaffolds were computed with the help of the camera focused at the middle of the stretched sample. Longitudinal and transversal strains were calculated according to the following expressions for square and honeycomb patterns (**table 3.1**).

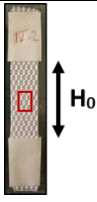
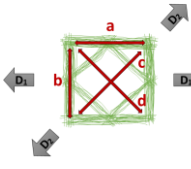
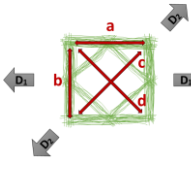
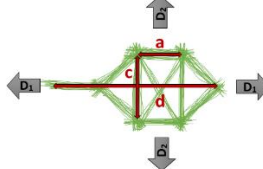
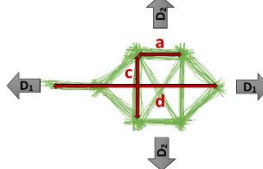
	Global	Square D ₁	Square D ₂	Honeycomb D ₁	Honeycomb D ₂
Configuration					
Longitudinal true strain	$\ln(H/H_0)$	$\ln(a/a_0)$	$\ln(c/c_0)$	$\ln(d/d_0)$	$\ln(c/c_0)$
Transversal true strain		$\ln(b/b_0)$	$\ln(d/d_0)$	$\ln(c/c_0)$	$\ln(d/d_0)$

Table 3-1: Expressions of global true strain and local axial true strains for square, honeycomb D₁ and honeycomb D₂ scaffolds

Global true strain (or global logarithmic or Hencky strain) value was determined with the initial and current gauge length, H_0 and H respectively, as described in **equation 3.4**:

$$Global\ True\ Strain = \ln(H/H_0) \quad (3.4)$$

Local strains were measured with the cell located in the middle of the sample (red rectangular on the figure of the global mechanical sample in **table 1.1**). A first comparison between local and global axial true strains were first evaluated to assess the homogeneity of the deformation through the stretched electrospun membrane. **Figure 3.10** exposes in red the three curves highlighting the difference between global and local true strains. The slope of the black straight line is equal to 1.

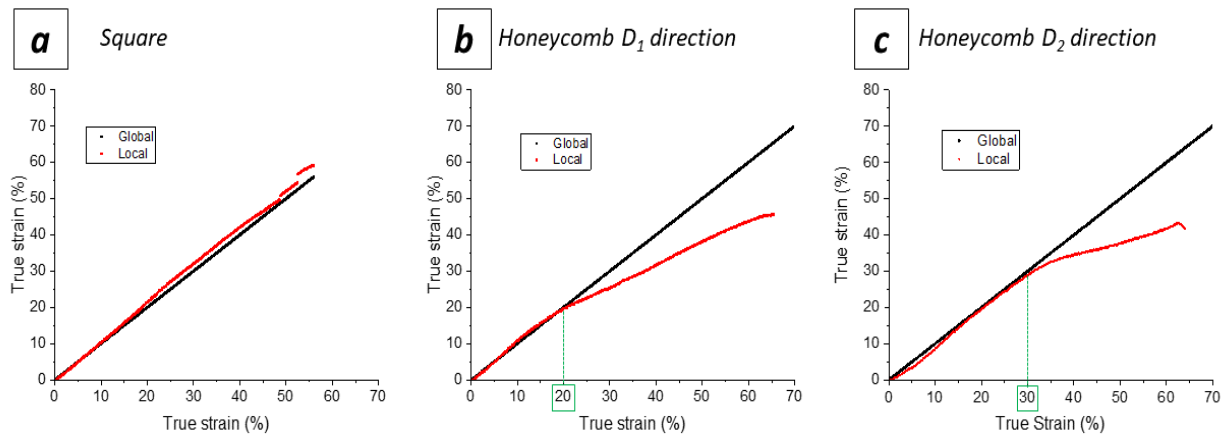


Figure 3-10: Global and local true axial strains of square (a) and honeycomb (b)-(c) patterned scaffolds

Local true strains measured on a square patterned scaffolds (**figure 3.10.a**) show a linear behavior in accordance with the calculated global true strains. For honeycomb scaffolds (**figures 3.10.b** and **3.12.c**), it can be seen local measurements are fitting with global data only at low strain, until a critical value (20 % for D_1 direction and 30 % for D_2 direction). Beyond this value, local strain appears lower proving a non-homogenous deformation in the all tensile sample.

This first analysis of local strains proves the need to describe tensile properties with a local measurement of the strain. The local investigation gives a better understanding of the mechanical answers of the tested scaffolds.

In this study and for the next chapter of numerical simulation, we will focus mostly on low strains to interpret mechanical answer of scaffolds.

3.2. Preliminary tests

3.2.1. Influence of the sample width

A preliminary study was performed to investigate the influence of tensile sample dimensions on mechanical behaviors. Indeed, only a limited number of elementary patterns can be contained in the small initial width l_0 of rectangular samples (see **figure 3.3.b**).

Widths of samples were varied from 6 to 20 mm. Depending on the patterned scaffolds (square or honeycomb), 2 to 10 elementary meshes were included in the sample width. Initial gauge length (H_0) was kept constant at 30 mm. Note that the sample width experiments were performed with the MTS machine where larger grips were available.

Axial tensile test results in **figure 3.11.a** prove that widths and thus number of meshes do not influence the mechanical behavior of square patterned scaffolds. Stress-strain curves with different width sizes are fitting quite well. Identical tendency was found with honeycomb scaffolds as illustrated in **figure 3.11.d**. Images in **figure 3.11.b** and **c** show patterned fibrous samples with $l_0 = 16\text{mm}$ at initial gauge length (H_0) and after imposed global strain equal to 25 %.

Square (**figure 3.11.a**) and honeycomb (**figure 3.11.b**) scaffolds were tested with different experimental conditions explicating the difference in measurement accuracy (noisier curves in **figure 3.11.a**)

In regards to the previous results, width of mechanical samples was set at $l_0 = 10\text{ mm}$ for every next experiment.

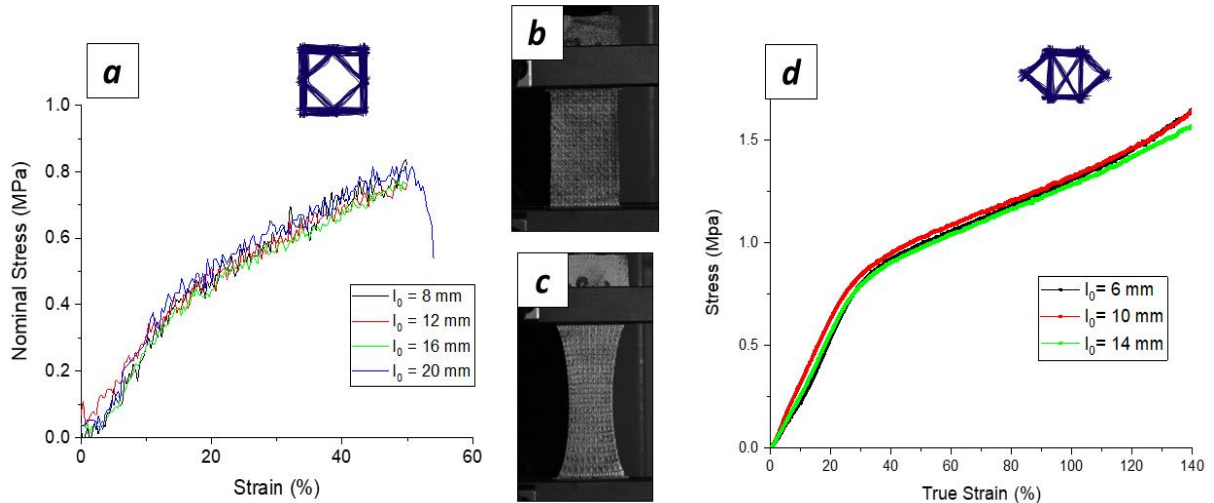


Figure 3-11: (a) Stress vs strain of PCL square scaffolds with various widths (8-20 mm or 4-10 elementary patterns), images of square patterned scaffolds ($l_0=16$ mm) before (a) and under (b) applied strain of 25 %, d) Stress vs strain of honeycomb scaffolds with various widths (6 to 14 mm)

3.2.2. Relaxation

Stress relaxation is a key parameter to analyze biomaterials aiming to replace tissue structures [155]. It represents a time-dependent decrease in stress under a constant strain. Inevitably, scaffolds need to sustain a biological network and undergo lot of external mechanical forces. Thus constitutive materials of a future artificial network require appropriate time related responses to external stimuli.

Stress relaxation tests were performed on patterned scaffolds to evaluate the viscous properties of the produced electrospun mats. Samples were stretched and kept at a constant global true strain of 5 % or 130 %. Nominal stress responses, i.e. loads required to maintain the fixed amount of deformation, are measured as a function of time (**figures 3.12**). Nominal stress values plotted in the graph are normalized by their highest starting value. Curves adopted always an exponential decay model distinctive of Maxwell polymer relaxation behaviors. Curves can be fitted with a double exponential function (**equation 3.5**) as in a few stress relaxation experiment on electrospun fibers [135], [156]–[158].

$$\sigma(t) = a e^{-t/\tau_1} + b e^{-t/\tau_2} + \sigma_\infty \quad (3.5)$$

For all studied fibrous membranes, total loss in nominal stress was evaluated around 33 % (infinite time). The material does not relax completely and still has a strong mechanical answer even after a long period of time under stress activity. Values of relaxation times are listed in the following **table 3.2**. Short relaxation τ_1 determined the first decreasing part of the relaxation curve, showing slightly lower

3. Characterization of the mechanical behavior of electrospun architected scaffolds

values for patterned scaffolds (16 and 23 seconds) compared to random or aligned fibers (25 and 24 seconds). Nominal stress is dropping faster with structured membranes (blue and black curves on **figure 3.12.b**). Nevertheless, all electrospun membranes exhibit the same decay relaxation mode with a consistent infinite stress σ_{∞} . Second relaxation time τ_2 , corresponding to the long viscoelastic behavior of the material, is higher for random scaffolds. It may be due to the fact that fibers are more reorganized when stretched with a random morphology. Then relaxation occurs due to both the structural reorganization of fibers and of the intrinsic PCL polymer. With aligned and patterned membranes, structures of fibers are less modified due to the initial fiber structuration. Thus, relaxation is induced mainly by the polymer chain relaxation and observes lower experimental values. However, values τ_2 (263 to 339s) might be not sufficiently small regarding the total time of the experience (800s) to ensure a good measurement of the long relaxation time.

	Random	Aligned	Square	Honeycomb
τ_1 (s)	24 ± 0.1	25.1 ± 0.1	23.4 ± 0.1	16.1 ± 0.1
τ_2 (s)	411.0 ± 1.3	339.1 ± 1.2	290.4 ± 1.1	263.3 ± 1.1

Table 3-2: Relaxation times of electrospun patterned membranes

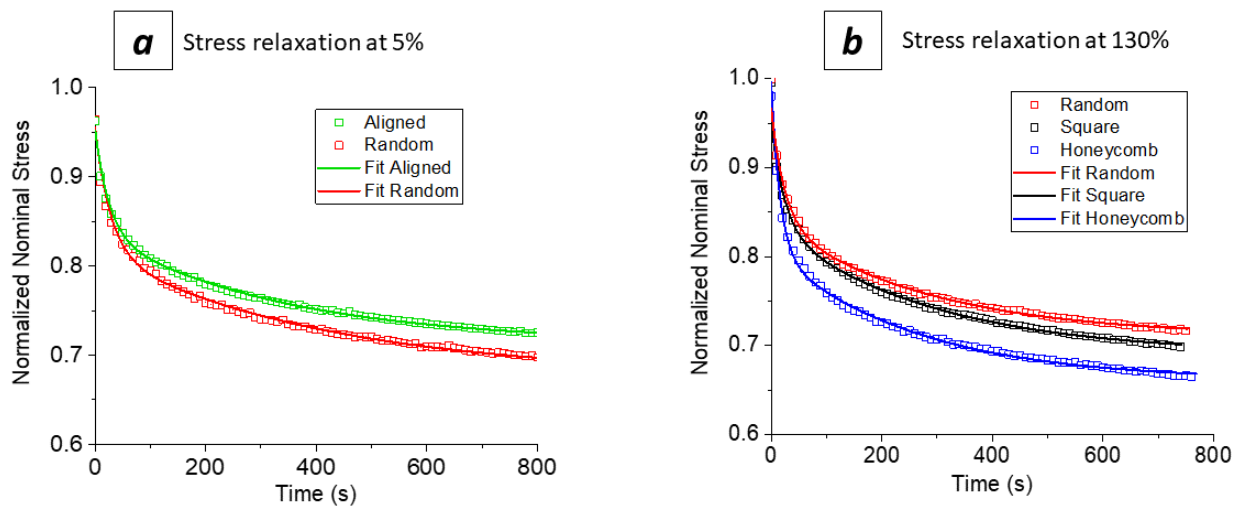


Figure 3-12: Relaxation of PCL electrospun scaffolds. Strains maintained at (a) 5 % and (b) 130 % of global true strain. Nominal stress is normalized by its highest value at $t=0$ s)

3.2.3. Cyclic tensile tests

Depending on the tissue to regenerate, scaffolds aim to last from a few weeks to a few months into the human body. Thus, during its entire lifetime, materials are going to withstand mechanical repetitive movements. Reactions of such cyclic effects are essential to evaluate in order to ensure the viability of an efficient mechanical support for cells.

Cyclic mechanical tests were carried out on square and honeycomb patterned scaffolds. Usual rectangular shaped samples were used and tested on a same classical tensile test bench as previously.

A single cycle is detailed in **figure 3.13.a**. A complete loop is divided in three steps of 45 seconds: ① a first elongation ramp at constant speed of 0.1mm/s, ② a 45 seconds period at a constant true strain value of 14 % and ③ a last step decreasing at 0.1mm/s until reaching the initial gauge length. 135 seconds-long cycle was repeated 20 times. For each cycle, a hysteresis curve of the measured axial force was plotted. **Figure 3.13.b** shows two first hysteresis loops of the fatigue test. During a single loop, measured force increases until a maximal axial force, then the material relaxes until a lower value of axial force. Finally, axial force reverses during the last step ③, reaching a zero force value before the initial gauge length. The remaining true strain ϵ_R is defined as the value of true strain at which axial force becomes superior to 0 N during the next loading. This value is measured from the second cycle of the fatigue test (red curve in **figure 3.13.b**). Previously discussed characteristic points are defined and illustrated on the **figure 3.13.b**.

The true strain value of 14 % (~15 % of strain) was selected as maximum strain as it refers typically to dynamic loading strain of soft tissues, such as cardiac muscle, under normal physiological conditions [159], [160].

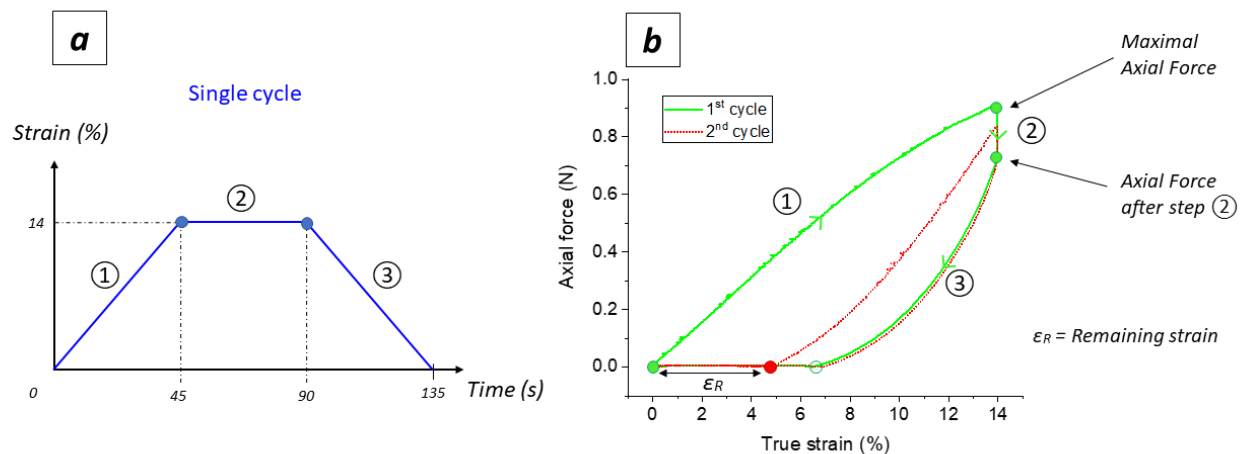


Figure 3-13: (a) Description of single cyclic test divided in 3 steps (b) Hysteresis curve of the first two cycles

Figure 3.14.a shows the superposition of all hysteresis curves for a complete fatigue test (20 cycles) of square patterned scaffolds. Blue and red curve refers to the first and last cycle respectively. Figure 3.14.b shows fatigue tests of honeycomb patterned scaffolds. Blue curves represent tensile tests performed in D_1 direction and red curves are in D_2 .

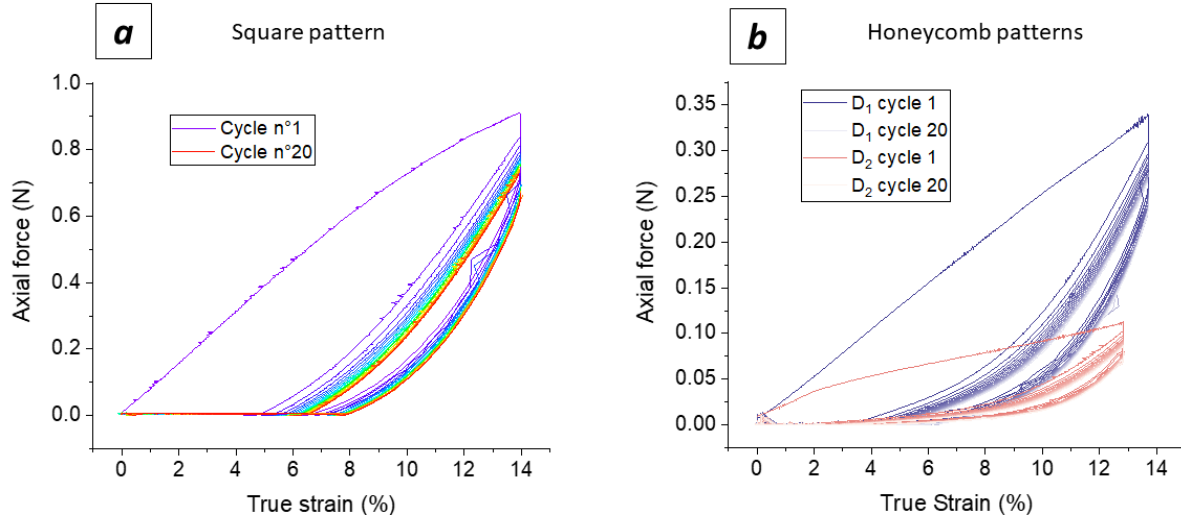


Figure 3-14: Hysteresis curves of 20 cycles of square and honeycombs (D_1 and D_2) patterned scaffolds

For all tested scaffolds, each single cycle shows a significant difference in measured axial force between loading and unloading phases. Value of axial force is always larger during the first ramp compared to the decreasing ramp, consequently forming a hysteresis loop [4].

First cycle of the test is largely superior to later cycles. A high energy is dissipated during the first loop which is characterized by a first high remaining strain. Initial slopes of the first and the rest of the cycles are thus very different. Material is stretched irreversibly losing energy in friction, structural fiber rearrangement and temperature dissipation. After the first cycle, a slower general decrease in force intensity and an increase in remaining strain are observed throughout all cycles. Similar cyclic behaviors were observed on natural tissues, with a strong permanent deformation during the first cycle, creating hysteresis curves [163].

Figure 3.15.a shows the recovery ratio of the 3 different patterned scaffolds during fatigue test. Recovery ratio defines the percentage of recovery of true strain after a complete cycle. It refers to the ability of material to find again its original length. It is directly related to the remaining strain after a cyclic load. The expression of recovery is detailed in equation 3.6, using for every cycle, the value of remaining strain ε_R pointed in figure 3.13.b.

$$\text{Recovery Ratio} = 1 - \frac{\varepsilon_R}{\varepsilon_{max}} \quad (3.6)$$

with ε_R the remaining strain, ε_{max} the maximum true strain applied (14 %).

Recovery ratios of patterned structures exhibit the same exponential decreasing behaviors as illustrated in **figure 3.15.a**. Honeycomb scaffolds in direction D_1 display the highest recovery ratio of 65 % after 20 cycles whereas square patterned mats show 50 % of recovery. Macrostructure and anisotropy of scaffolds trigger different recovery ratios.

Figure 3.15.b illustrates the evolution of the resilience through 20 cycles. Resilience is the ability of a material to deform and release energy upon unloading (evaluation of energy loss) [6]. Resilience is calculated from an energy ratio (see **equation 3.7**) for each cycle, obtained from the areas under loading and unloading curves (loop area).

$$Resilience = \frac{W_{unload}}{W_{load}} \quad (3.7)$$

with W_{load} area under the loading curve, W_{unload} area under the unloading curve.

No changes in Resilience is observed between the three scaffolds. **Figure 3.15.b** displays the progression of resilience for square and honeycomb scaffolds. All adopt an important sudden burst before reaching a plateau of 60-65 % (resilience values of the first cycle around 25 %). The first abrupt increase is related to a high loss of energy as described previously (decrease of the first loading curve).

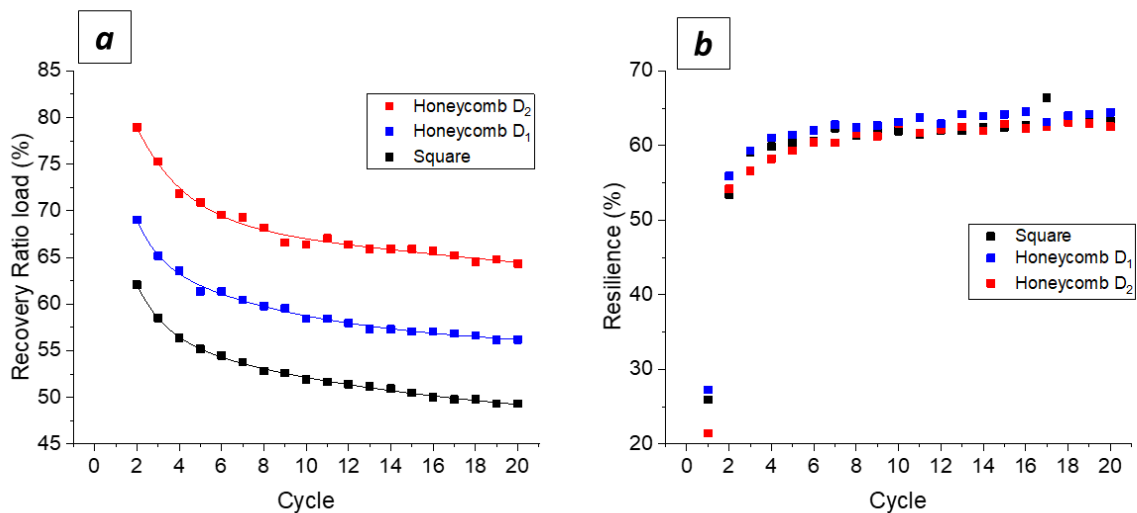


Figure 3-15: Recovery ratio (a) and Resilience (b) of square, honeycombs (D_1 and D_2) patterned scaffolds

3.3. Mechanical behavior of scaffolds under monotonic tensile loading

Next section describes mechanical behavior of PCL electrospun materials obtained with a monotonic tensile loading. Nominal stress assessment of raw PCL, random and aligned fibers scaffolds is firstly exposed. Then mechanical anisotropy of patterned scaffolds is discussed. Each structure type, honeycomb and square scaffolds, is analyzed via nominal stress curves and local strain investigations.

3.3.1. Raw, Random and Aligned scaffolds

Nominal stress measurements were performed on raw PCL, random and aligned electrospun membranes. These three materials were first investigated to obtain reference data of the constitutive materials of the patterned scaffolds, which can be roughly assimilated to an association of aligned and random parts.

Nominal stress versus global true strain curves of raw PCL, aligned and random fibers are exposed in **figure 3.16**. Raw PCL polymer (black curve) has an overall higher stress answer with an estimated Young modulus of 203 MPa. This experimental value is consistent with the measurement of PCL mechanical properties found in the literature. Tensile moduli values are ranging from 100 to 500 MPa [146], [164]–[166] depending on the molecular weight, sample preparation and tensile measurement procedures. In our case, raw PCL polymer was molded by solvent evaporation on a Teflon mold in order to obtain small rectangular samples.

Randomly collected fibers formed a structure with a lower mechanical behavior. Young modulus was estimated at 6 MPa and value of nominal stress is always inferior to 1.5 MPa. This result matches with mechanical data of the literature. Electrospun PCL scaffolds display usually Young moduli ranging from 0.5 to 40 MPa [136], [146], [167]–[170], depending on electrospinning conditions and thus scaffold porosity and fiber morphology.

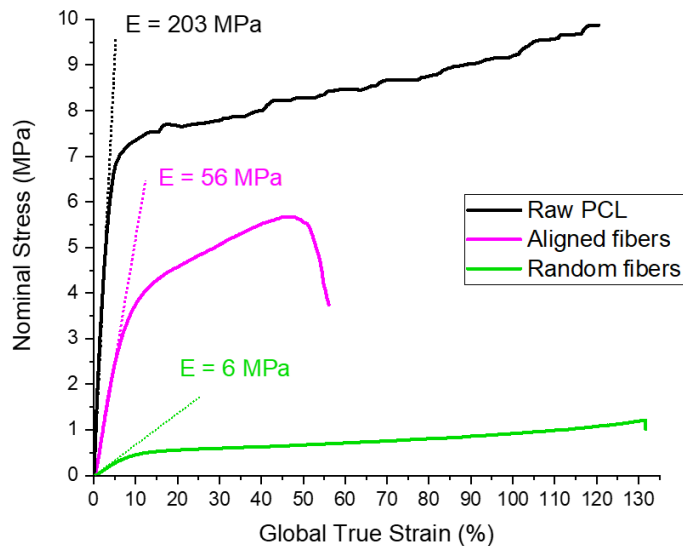


Figure 3-16: Nominal stress of raw PCL, aligned and random electrospun fibers

Aligned fibers exhibit mechanical properties comprised between raw PCL and randomly collected fibers (see **figure 3.16**). When the load is applied parallel to the alignment of fibers, a value of 56 MPa is evaluated from stress-strain curve. However, while applying a load perpendicular to the preferential orientation of fibers, mechanical strength decreases drastically to 0.16 MPa (**figure 3.17.b**). Scaffolds made of aligned fibers usually showed an important mechanical anisotropy. In this particular case, a ratio between Young moduli E_{long} and E_{trans} superior to 100 was estimated. Weaker properties in transversal direction can be easily understood due to a low cohesion between fibers. Along aligned direction, all fibers are pulled in the same manner longitudinally. Young modulus of aligned fibers is almost 10 times superior to random scaffold. In another hand, random scaffolds have a longer extensibility. Aligned fibers break around 50 % of global true strain (**figure 3.16**).

This mechanical anisotropy was previously exhibited in other scientific studies in which aligned fibrous scaffolds were produced by electrospinning. Nevertheless, smaller anisotropic ratios are evaluated, typically from 2 to 15 [8], [134], [171]–[173]. Such variability might be explained by different factors such as fiber surface properties, dimensions of fibers, scaffold porosity, triggering in each case different surface and cohesion interactions between parallel fibers.

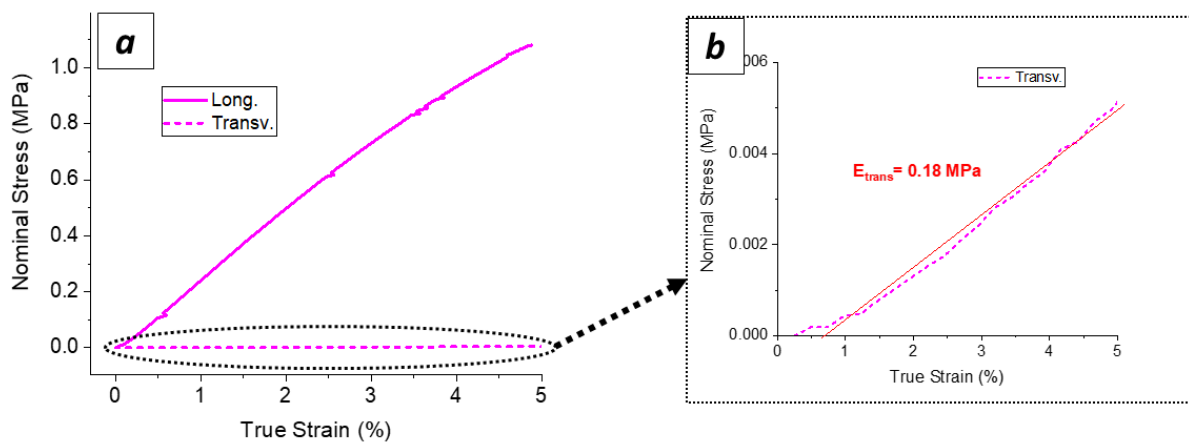


Figure 3-17: Nominal stress of aligned fibers (a) in longitudinal and transversal directions until 5 % of global true strain, (b) zoom in transversal direction

3.3.2. Honeycomb scaffolds

The next section is dedicated to the mechanical performance of honeycomb patterned membranes. Anisotropy of such produced structures was assessed by nominal stress and local true strain measurements.

3.3.2.1. Nominal stress assessment

Figure 3.18 displays tensile curves, nominal stress versus global true strain, of the honeycomb fibrous mats. Curves show a classic “stress-strain” like shape observed in electrospun membranes, beginning by a quasi linear part at low strain (until approximately 15 % for D_1 and 30 % for D_2) and followed by a plateau. This two steps behavior is specific of fibrous polymer materials [174], [175]. Failure was observed in the case of D_1 direction around 55 % of global strain. Rupture of tensile samples occurs always at the vicinity of the grips. In D_2 direction, a maximum strain of 130 % was reached before complete rupture of fibers (maximum apparatus gap of the test bench). Slope in the first elastic part, indicated here as modulus E , is significantly higher in the D_1 direction, $E_1 = 1.7 \text{ MPa}$ versus $E_2 = 0.42 \text{ MPa}$ for D_2 . Such parameters are slightly lower than the ones found in the literature of PCL patterned scaffolds collected on metals grids (2 to 4 MPa for Vaquette et al [146] or 5 to 10 MPa for Wang et al [176]). Yield Strains delimit the first linear elastic regime and the second plateau regime, i.e. where the first part of the curve becomes markedly nonlinear. They were evaluated on the basis of 0.2 % strain difference between the elastic line and the actual curve. Tensile tests performed in the D_2 direction

display a high yield strain of 38 % whereas in D_1 direction, yield point is reached at a lower value of 19 %. Honeycomb scaffolds have a larger elastic domain in the D_2 direction in which the scaffold can withstand a higher mesh deformation (structural deformation) before material deformation (PCL fiber deformation).

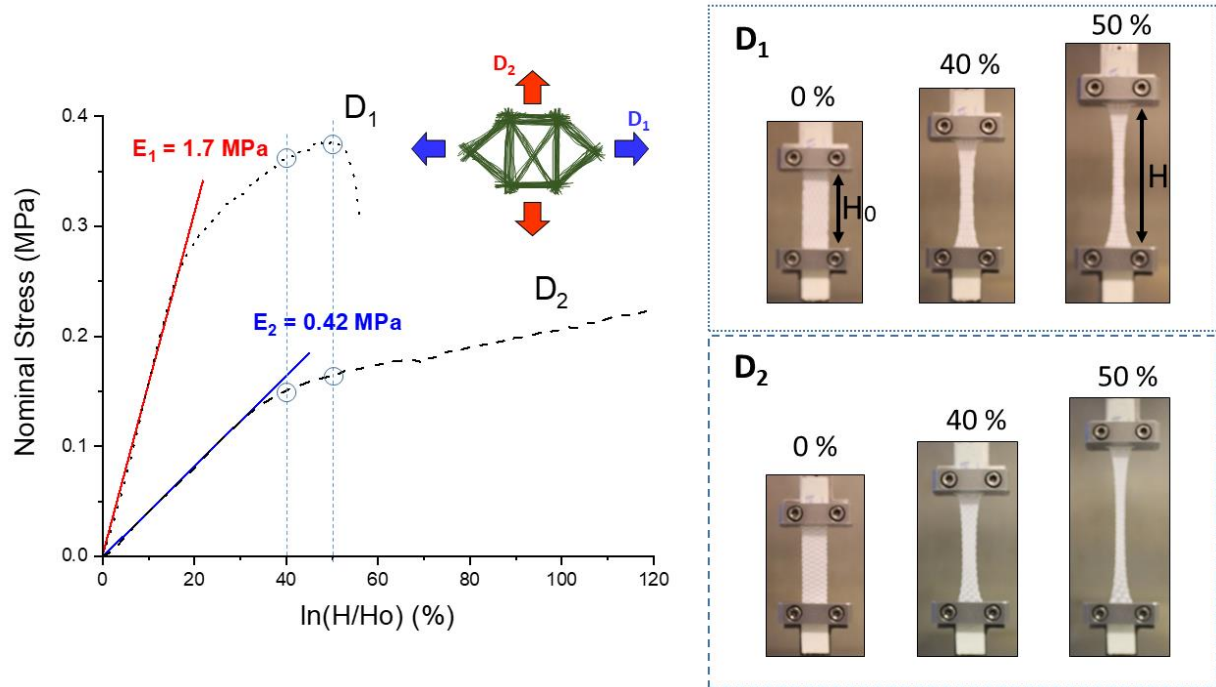


Figure 3-18: Nominal stress vs global True Strain of honeycomb PCL scaffolds. Pictures of tensile test in D_1 and D_2 directions at 0, 40 and 50 % of global true strain

Anisotropic ratio, E_1/E_2 of moduli of the first linear part, has a value of 4.2 proving the strong anisotropic behavior of produced mats. Such difference in axial stresses between D_1 and D_2 directions is due to the structural fibers orientation of the honeycomb configuration. Similar results on mechanical properties were obtained with fibers collecting on a metallic screw, producing a significant anisotropy ratio of 3.4 between longitudinal and transversal directions [23]. In our case, the anisotropic ratio is in good accordance with most natural soft tissues found in the human body (anisotropy between 3 to 5) [177], showing that our strategy is promising for soft tissue engineering applications.

3.3.2.2. Local strains investigation

In order to explain the influence of the microstructure on anisotropic behaviors of honeycomb scaffolds D_1 and D_2 , local deformations were investigated during tensile test. **Figure 3.19** shows pictures of the single honeycomb mesh during elongation taken by a digital camera focused at the center of the gauge length of rectangular samples. Local true strains in D_1 and D_2 directions (see expressions in **figure 3.19**) were extracted from the sequence of images. Images after 40 % of global

3. Characterization of the mechanical behavior of electrospun architected scaffolds

true strain were not exploited due to a loss of contrast or a loss of the visual monitoring of the protrusions. Plot in **figure 3.19** displays the Nominal Stress versus the global or local axial true strain.

No apparent difference is observed between local and global strains, until a critical value of 10 % for D_1 direction and 30 % for D_2 direction. This similarity proves that local strains at the center of the sample is matching the global true strain during the first part of uniaxial tensile experiments. However, after critical values, corresponding to higher strains, heterogeneous deformation occurs resulting in a mechanical system difficult to analyze.

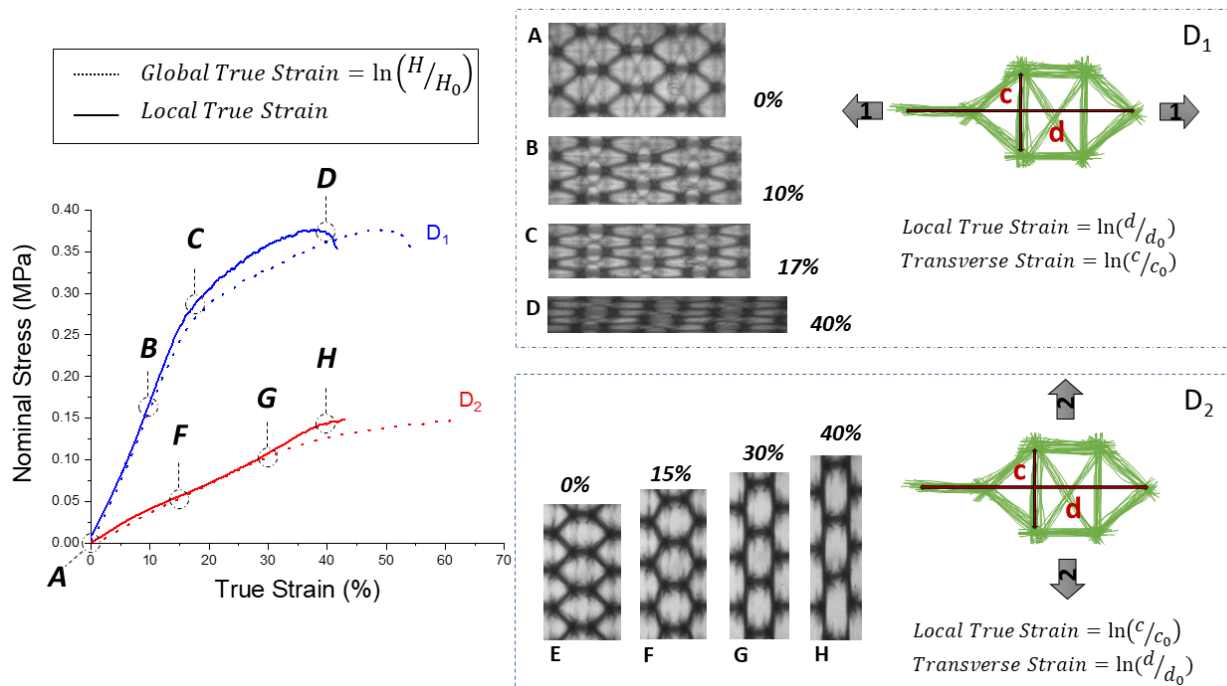


Figure 3-19: Nominal stress of honeycomb scaffolds in function of global (dashed line) or local true strains (solid line). Pictures of D_1 and D_2 scaffolds at different global true strains

Figure 3.20.a exhibits the link between the longitudinal (local true strain) and transversal strains in D_1 and D_2 directions. Both values of the transversal strain are negative, which indicates a contraction of the material in the perpendicular direction. Honeycomb scaffolds expose a higher overall transverse strain in D_1 direction compared to D_2 direction.

This difference of the membrane contraction during stretching is a direct consequence of the scaffolds microstructure. Fiber network induces a better transversal resistance in D_2 direction. As D_1 tensile test samples are more contracted along the transversal direction, higher stresses will be applied at the vicinity of the grips. This phenomenon would explain the localized failure observed around the grip area at a shorter elongation in D_1 direction (**figure 3.19**).

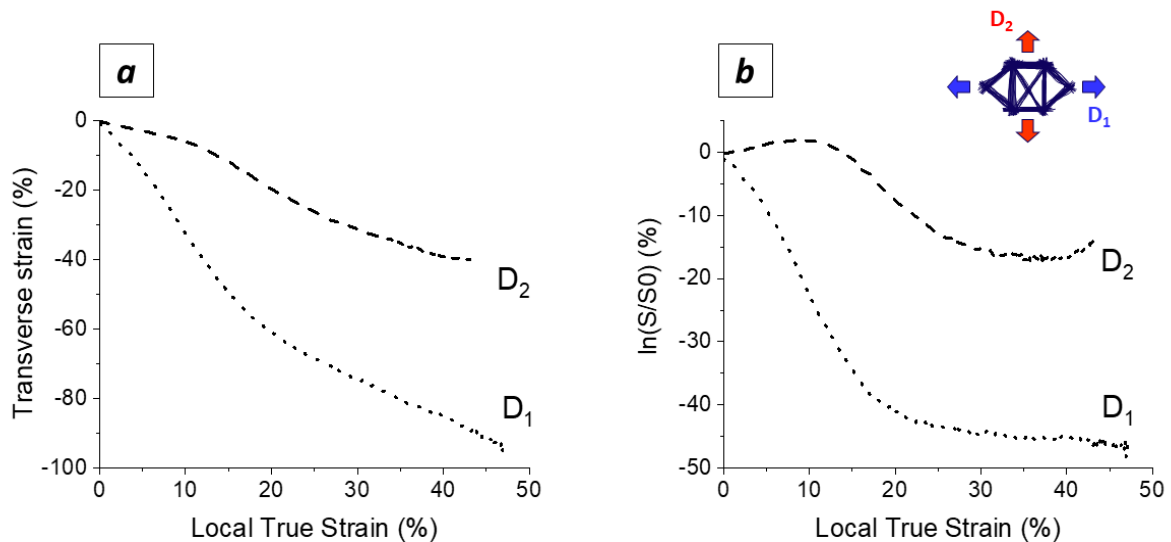


Figure 3-20: Local deformation of a single honeycomb mesh (D_1 and D_2 directions), (a) Transverse strain versus Local True Strain, (b) local relative variation of the surface

Figure 3.20.b shows the local relative variation of the surface $\ln(S/S_0)$ of a single honeycomb cell during stretching. This relative variation is simply calculated from the sum of the local transverse and longitudinal true strains. A reduction of surface in the D_1 direction is observed from 0 to a maximum of -45%. In D_2 direction, the surface of the mesh initially increases weakly up to an axial strain of 17% and then decreases gradually, leading to a relative surface reduction of -15%. The evolution of relative variation of the surface clearly exposes the anisotropic behavior of honeycomb scaffolds. The geometry of the mesh induces a distinct mechanical answer depending on the load directions.

3.3.3. Square scaffolds

Square patterned scaffolds were mechanically tested. This section exposes the main results of nominal stress measurements coupling with local strain investigation.

3.3.3.1. Nominal Stress assessment

Figure 3.21 shows stress-true strain curves of square patterned scaffolds. Nominal stress graph is plotted here with global true strain calculated for the gauge length H of the sample. Local assessment is only exposed later for the transversal and longitudinal strains of squared scaffolds. The shape of the curve is similar to electrospun membranes and to the previously described curves of honeycomb-

3. Characterization of the mechanical behavior of electrospun architected scaffolds

shaped mats. The plot begins by a quasi-linear zone, slope of 1.3 MPa, followed by a plateau until a global true strain value of 110 %.

It was surprisingly found that these squared shaped scaffolds do not exhibit anisotropic properties in two loading directions illustrated in **figure 3.21.b**. Curves representing nominal stresses in longitudinal 0° D₁ and 45° D₂ directions do not differ distinctively. These results were not expecting as scaffolds exhibit morphological anisotropy.

A complex mechanism especially in the center of the meshes, bridges oriented at 45° and fibers crossing the gap might play a non-negligible role in mechanical stress answer of the global material. Influence of central zone of the mesh and the secondary bridges will be analyzed through a numerical approach in the next chapter.

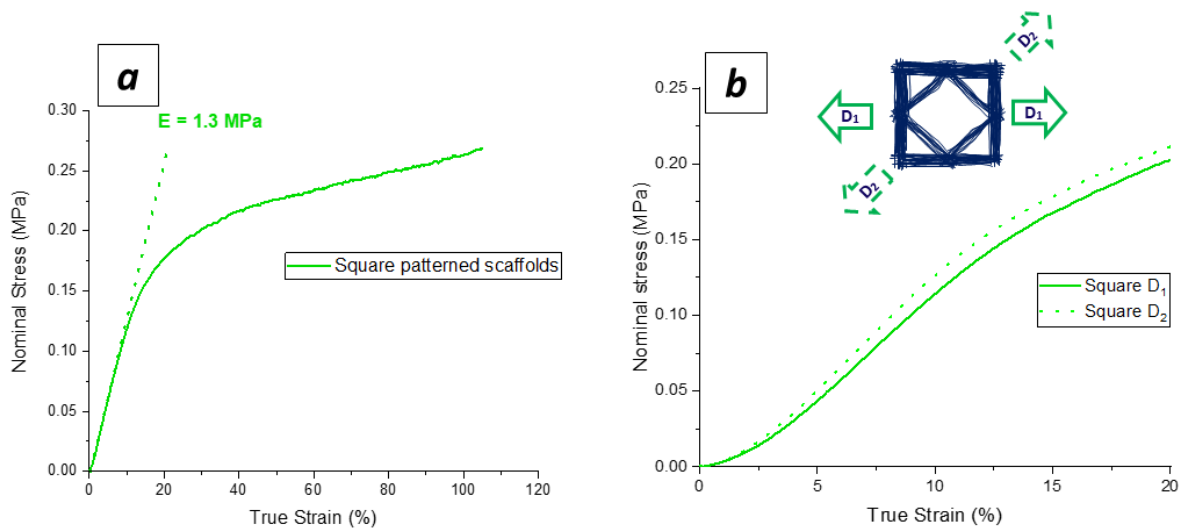


Figure 3-21: (a) Nominal stress vs global True Strain of squared PCL scaffolds (b) Square patterned scaffolds in longitudinal and diagonal directions

Figure 3.22.a shows the respective nominal stress curves of the square and honeycomb scaffolds. Comparison with honeycomb scaffolds can be made but it has to be nuanced by the nominal stress correlation introduced in this study. Indeed, the mass normalization was performed with the hypothesis of a same mechanism deposition and same final porosity of the membranes. With the tridimensional collectors, morphology, fibers density distribution and global porosity are slightly changed (95 % and 97 % of global porosity for square and honeycomb scaffolds respectively).

Nevertheless, patterned scaffolds can be compared by normalizing them by their respective porosity following the next **equation 3.8**:

$$\text{Normalized nominal stress} = \sigma (1 - p) \quad (3.8)$$

Figures 3.22.b shows the normalized nominal stress curves for square, honeycomb D₁ and honeycomb D₂ scaffolds (respectively green, blue and red curves). Square membranes exhibit a similar trend than the honeycomb scaffolds in D₁ direction in terms.

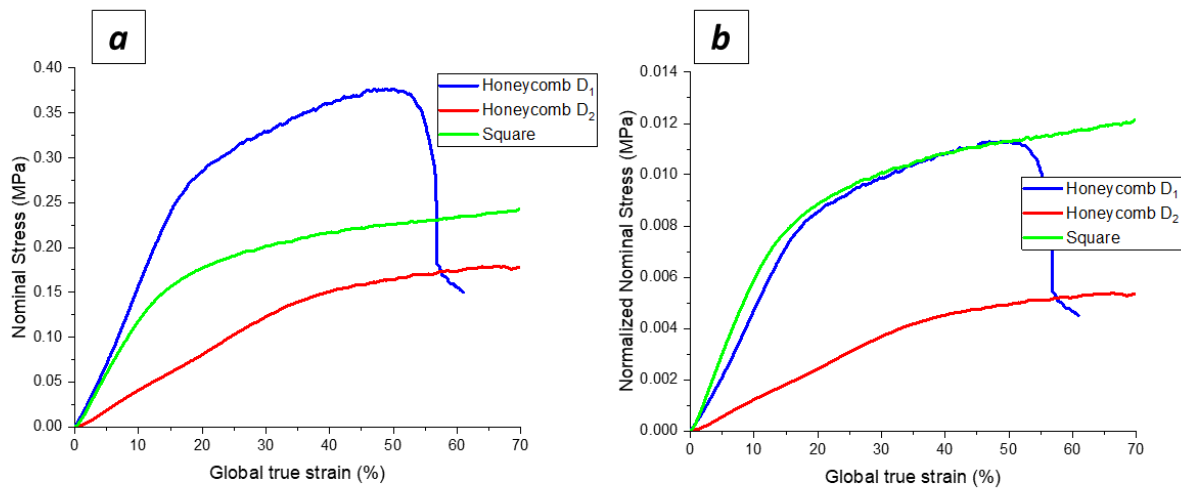


Figure 3-22: a) Nominal stress and b) Normalized nominal stress (equation 3.8) of electrospun patterned scaffolds

3.3.3.2. Local strains investigation

Figure 3.23.a plots local transversal true strain versus local true strain measured by the digital camera. Local strain measurements were carried out only in D₁ direction for square scaffolds. Negative transversal strain reaches an approximate value of -50 % after 60 % of true strain. From 0 to 40 % of true strain, fibrous squared material is contracted following globally a linear compression curve of -1 (dashed line).

Local relative variation of the surface $\ln(S/S_0)$ of a single square mesh during stretching is plotted in **figure 3.23.b**. Square patterned scaffolds observes globally lower values of $\ln(S/S_0)$ (inferior to 4 %) compared to honeycomb scaffolds. A first increase in surface is observed at low true strains (0 to 25%), with a maximal surface variation value of 4 % (10% of true strain). From 25 to 40 %, $\ln(S/S_0)$ becomes negative, which can be correlated to a Poisson's coefficient (ν) superior to 1. Indeed, transverse strain curve in **figure 3.23.a** is below the dashed line corresponding to a $\nu = 1$. Finally, local surface increases again to reach higher value of extension.

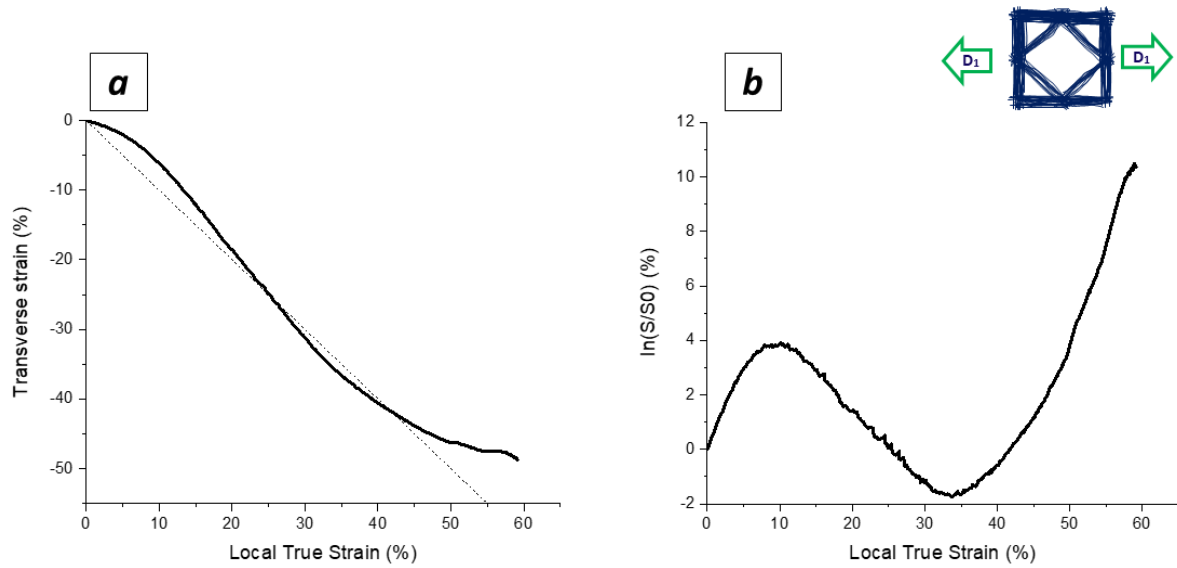


Figure 3-23: Local deformation of a single square mesh (longitudinal direction), (a) Transverse strain versus Local True Strain, (b) local relative variation of the surface

3.3.4. Honeycomb batch B: where is anisotropy?

This last section describes the mechanical behavior of produced honeycomb membranes by electrospinning with another polymer batch B. Exact same procedures in terms of solution preparation, electrospinning parameters and mechanical tensile tests were carried out to fabricate honeycomb patterned scaffolds.

Mechanical results illustrated in **figure 3.24** show surprisingly a loss of anisotropy in honeycomb scaffolds in directions D_1 and D_2 . No clear difference is observed between nominal stress-strain curves in D_1 (blue) and D_2 (red) directions. This change in mechanical behavior is directly related to the new made polymer solution (batch B) and its properties that might influence final honeycomb scaffold morphology.

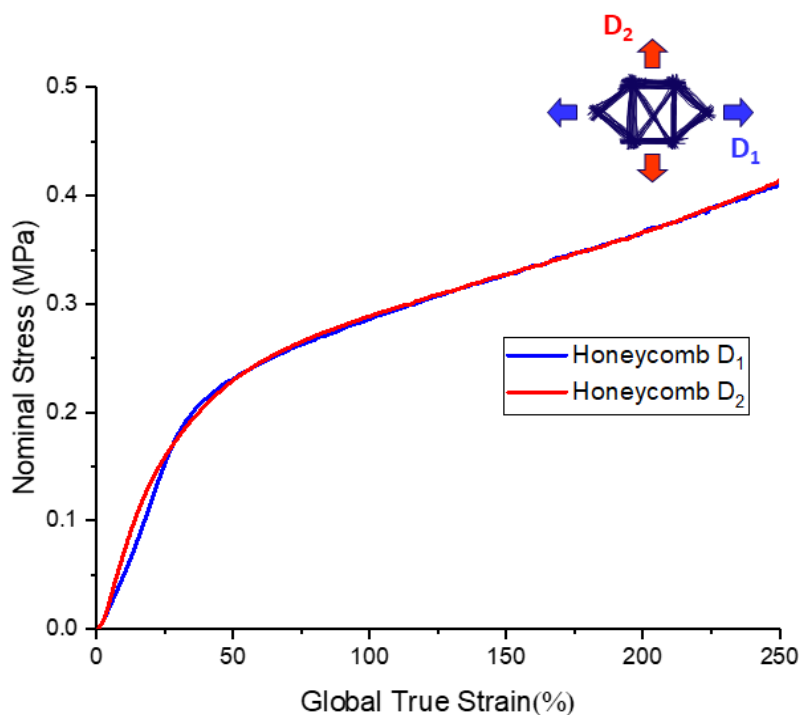


Figure 3-24: Stress-strain curves of Honeycomb scaffolds (batch B) showing no anisotropy in two loading directions D_1 and D_2

Two different PCL polymer batches were used to fabricate electrospun PCL scaffolds. It has been noticed that membranes produced with same concentration solution and environmental parameters had significant different final morphologies. **Figure 3.25** shows honeycomb patterned membranes with PCL polymer providing from batches A and B. Fibers adopt a less-organized architecture in the center of the mesh with bath A. On transmission mode images of case B, more fibers (in black) are observed in the center of the honeycomb scaffolds. Fibers have roughly the same average diameter of $4\mu\text{m}$ in both cases which implies that the process of fiber creation (jet initiation and whipping phase) is similar in batch A and B.

In order to elucidate this difference in structural aspect, measurements of polymer solution viscosity of the two batches were carried out. At a shear rate of 0.1 s^{-1} , a loss of viscosity from $70\text{ Pa}\cdot\text{s}$ (batch B) to $7\text{ Pa}\cdot\text{s}$ (batch A) was observed for PCL solution blended in the DCM/MeOH (4:1) mixture. Physico-chemical properties of PCL polymer solution differ greatly with the two batches. PCL polymer might be affected and damaged with the period of storage, which influences the final polymer solution properties.

The change in viscosity seems to be the main factor that influences fiber deposition on the 3D substrates. With higher viscosity, polymer filaments are more willing to agglomerate on the protrusions. Indeed, their increased rigidity hinders fiber deformation and consequently more energy is required to stretch the fiber jet over a longer distance, so to cross the gap in the mesh center.

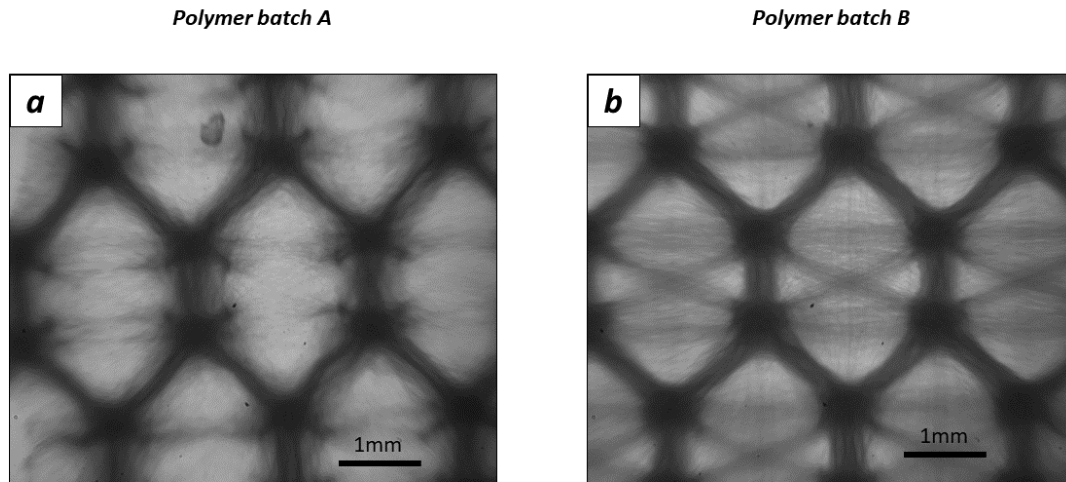


Figure 3-25: Optical images of honeycomb scaffolds electrospun from old PCL batch A (a) and new batch B (b)

Mechanical anisotropy seems to be highly related to the presence of fibers in the center of the honeycomb cell. A more detailed investigation of such mechanical behaviors, particularly the link between material properties of the mesh center and global anisotropy will be detailed in the next numerical chapter.

3.4. Conclusion

This chapter described the mechanical investigation carried out on electrospun structured membranes. Mechanical tests were performed on honeycomb and square patterned scaffolds in two different directions to analyze their anisotropic behavior. Monotonic tensile tests on honeycomb scaffolds proved an anisotropy of 4.2 between longitudinal and transversal directions, strong anisotropy matching the range of soft tissue structural properties. Morphology of the honeycomb mesh induces a local strain behavior dependent on the loading direction. Furthermore, mechanical tests performed on square patterned scaffolds showed an isotropic behavior when samples were pulled at 0 and 45 loading directions. Newly produced honeycomb scaffolds with batch B showed a loss of the previous anisotropic behavior. Fibers collected in the center part of the cell seems to be a key parameter which triggers mechanical properties and anisotropy of the scaffolds.

The template-assisted electrospinning brings a new method to custom scaffolds for regenerative medicine with specific anisotropic mechanical properties. New Aligned and random electrospun fibers which can be considered as main constitutive elements of the patterned scaffolds (fibers aligned in bridge zones and random deposition on peaks) were mechanically investigated. Material properties were thus identified for a further modelling of electrospun structures.

4. Modelling of mechanical behavior of structured scaffolds: a finite element approach

This chapter is dedicated to the investigation of mechanical behavior of the patterned scaffolds through a numerical approach. It presents a finite element model of the patterned scaffolds (honeycomb and square patterns). The objective is to reproduce and analyze numerically tensile mechanical tests of the produced electrospun membranes. The first section details the finite model employed, describing the geometry of the cell and of the patterned scaffolds and identifying mechanical behaviors of the constitutive components. Numerical results are then presented and compared to global and local experimental data previously obtained in chapter 3. Honeycomb scaffolds are first analyzed, followed by square patterned scaffolds.

4.1. Finite element mechanical model

4.1.1. General approach

The objective of the numerical study is to reproduce and analyse experimental tensile tests previously performed on electrospun membranes. Ansys mechanical software was used to develop the finite element simulation.

A full sized mechanical sample ($H_0=30$ mm and $l_0=10$ mm) to model is displayed and disposed in the xy plane as in **figure 4.1.a**. Plane stress state hypothesis was considered in this study meaning that following stress components along z are neglected ($\sigma_{xz} = \sigma_{yz} = \sigma_{zz} = 0$). As the specimen and loading are symmetrical, only a quarter of the full sample is needed to model the monotonic axial test (**figure 4.1.b**).

Specific boundary conditions are applied to the rectangular surface as described in the **figure 4.1.c**. At the left and bottom edges of the structure marked in dashed green lines, displacements respectively along X or Y were defined null ($U_x=0$ for left and $U_y=0$ for bottom edges). A vertical displacement (red dashed line) is applied at the top line of the structure ($U_y>0$) keeping the X position constant ($U_x=0$) to reproduce the gripping of the tensile specimen. Each simulation step was obtained by incrementing a forced displacement of 0.1 mm at the top of the sample (red lign). **Table 4.1** lists the values of global true strains for the corresponding steps.

4. Modelling of mechanical behavior of structured scaffolds: a finite element approach

Step n°	1	2	3	4	5	6	7	8	9	10	...15	...20	...25	...30	...35
Global True Strain (%)	0.66	1.3	2.0	2.6	3.3	3.9	4.6	5.2	5.8	6.5	9.5	12.5	15.4	18.2	21

Table 4-1: Global true strain values of numerical steps

Patterned membranes are composed of a periodic structure of honeycomb or square unit cells. Thus mechanical samples were reconstructed by symetries and duplications of an elementary cell (honeycomb shapes in **figure 4.1.c**).

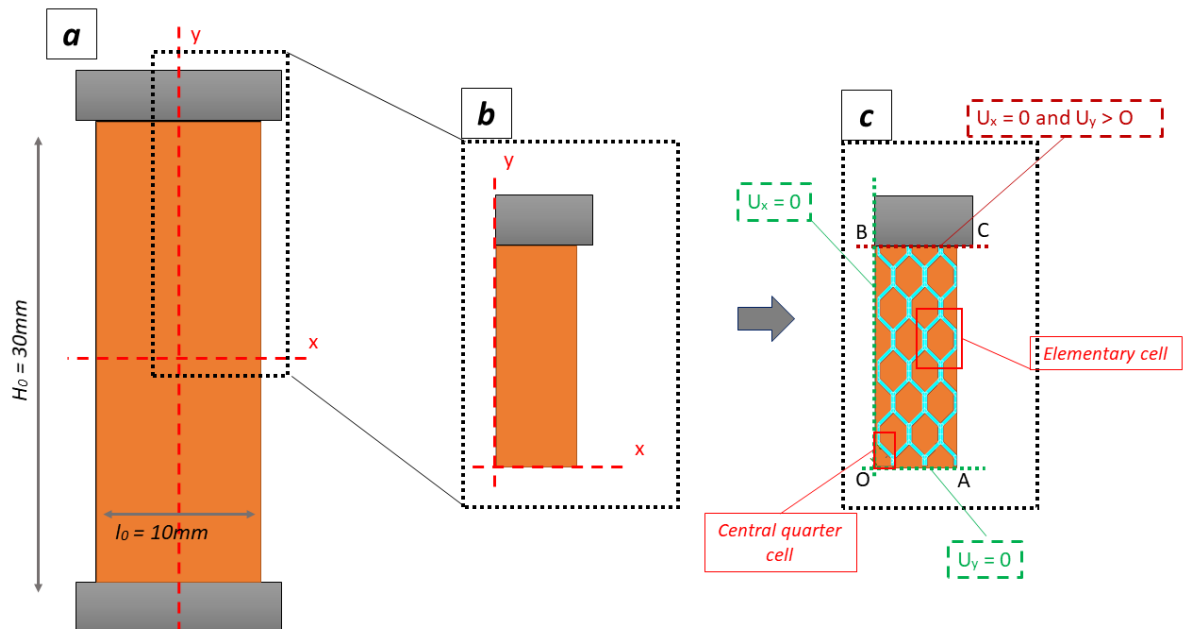


Figure 4-1: Sample mechanical and cells distribution: a) tensile sample, b) quarter of tensile sample, c) patterned sample and boundary conditions

As shown in **figure 4.2**, honeycomb geometrical model was designed from simple rectangular areas. Rounded corners were added to smoothly connect the different areas and avoid discontinuities. **Figure 4.2.b** shows a quarter of a honeycomb cell. Two distinct zones were differentiated, blue and purple areas, referring to two different materials. Zones ② and ③ were associated to aligned fibers-type materials with a preferential fiber orientation of 90° or 45°, whereas zones ① were designated as

randomly deposited fibers-liked materials. Geometry dimensions were carefully selected from optical images. Contours of two constructed honeycomb cells were superposed in order to match the image of honeycomb scaffolds as shown in **figure 4.2.a**. A complete geometrical honeycomb unit cell was obtained by X and Y symmetries of the first conceived areas of **figure 4.2.b** (quarter of cell).

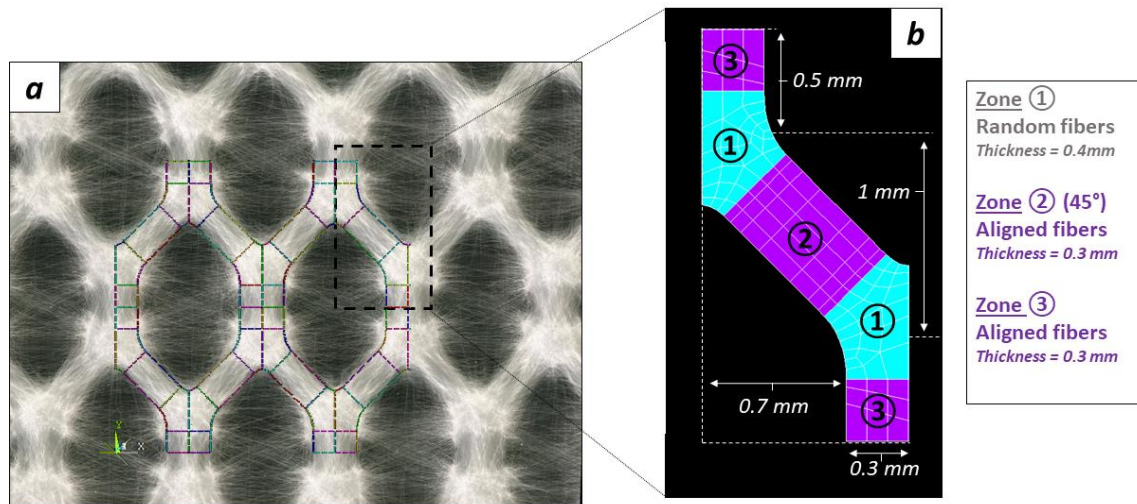


Figure 4-2: Design of the honeycomb cell: (a) elementary designed pattern on optical image of honeycomb scaffold, (b) design of a quarter of the honeycomb cell with allocated areas

4.1.2. Meshing

Meshing was performed using 2D Elements with quadratic interpolation of displacement. Meshed quarter cell is illustrated in **figure 4.2.b** with the dashed white delimitation lines. Mesh is refined in the curved zones of the geometry where most stresses are concentrated. Elements PLANE183 in ANSYS defined by 6 or 8 nodes were employed. Nonlinear geometry mode (NLGEOM) was selected to activate geometric nonlinear analysis.

The finite element modelling is based on a plane stress hypothesis. This allows a simple 2D model. However, thickness of each fabricated area can be independently defined. Thus we introduce a 3D approach by allocating different thicknesses to different zones in agreement with the specific topography of electrospun scaffolds.

According to the 3D profilimeters, cross section and thickness measurements of the fibrous scaffolds in **chapter 2**, specific values of thicknesses were attributed for zones ①, ② and ③. Thickness for zones ① (0.4 mm for honeycomb) were attributed regarding the average apparent thickness measured experimentally (high thickness values of the peaks). Thicknesses of fibrous lower parts were

estimated from profilimeter graphs (**chapter 2**). A value of 0.3 mm was allocated for both fiber bridges (zones ② and ③).

4.1.3. Properties of constitutive materials

Patterned scaffolds can be differentiated into two material components: random and aligned fibers. This section exposes the mechanical model and the selected input material properties required for the numerical simulation. Mechanical properties were selected either from experimental data obtained in **chapter 3** or known materials found in the literature.

General assumption of pure elastic model was selected. In this numerical approach, viscosity and plasticity of electrospun membranes are neglected.

The first constitutive part of patterned scaffolds, associated to zones ① of **figure 4.2** was integrated as a material composed of random fibers. Electrospun random fibers exhibit no distinct macro organization morphology and adopt isotropic mechanical behaviors. In the finite element model, zones ① in blue in the elementary pattern (**figure 4.1**) were defined as isotropic materials. Such materials are characterized by only two parameters, a Young modulus E and a Poisson's ratio ν . Young moduli are then identical in the three orthogonal directions ($E_1=E_2=E_3$), meaning that material will deform in the same manner independently of the loading direction. Young modulus for random fibers was estimated through the previous mechanical test performed on randomly collected electrospun membranes (see **chapter 3**). A value of $E = 5.6$ MPa was measured and selected as Young modulus parameter for the numerical simulation (**figure 4.3**). Poisson's ratio was set at 0.46 according to mechanical results found in the literature on PCL electrospun membranes [178].

Zones ② and ③ were associated to aligned fibers. In a first approach, this second structural material is considered isotropic. Young modulus was determined from the mechanical tests along the direction of the fibers. A strong value of 56MPa was identified as E parameter for the zones ② and ③. As for isotropic random fibers, a value of 0.46 was set as Poisson's coefficient. The influence of anisotropy will be studied in **section 4.2.2**.

Both materials exhibit a quasi linear behavior in a first elastic regime delimited from 0 to 10 % of true strain in **figure 4.3**. In the mechanical model proposed, only small deformation will be investigated as the material does not behave linearly at strains superior to 10 %.

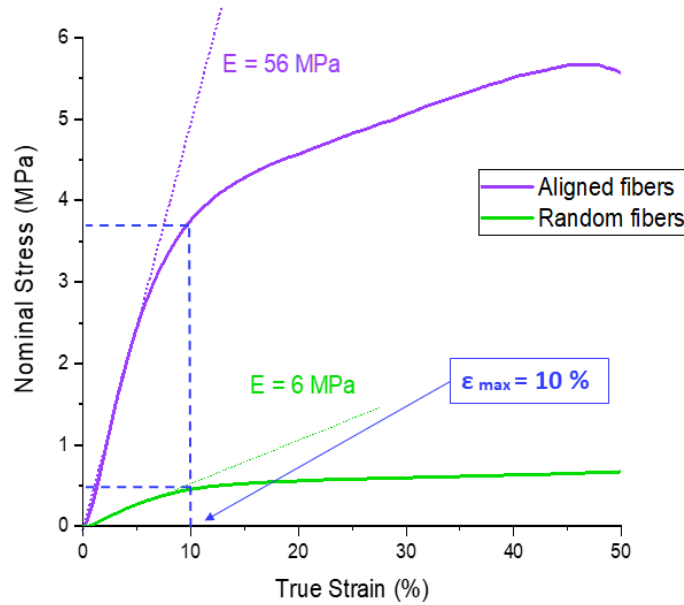


Figure 4-3: Nominal Stress-true strain curves of aligned and random fibers (from experimental part-chapter 3)

4.2. Modelling of Honeycomb scaffolds

The first part of the numerical results is focused on honeycomb scaffolds. A first model assumes that all materials are isotropic. The modeling of the structure is illustrated and compared to mechanical data previously obtained in **chapter 3**. Then, a more complex model, involving orthotropic behaviors in aligned fibrous zones is implemented. Finally, a last part is dedicated to the study of the anisotropy of the honeycomb scaffolds, studying more specifically the deformation of the quarter cell at the center of the tensile sample (**figure 4.1.c**).

4.2.1. Model 1: isotropic materials

4.2.1.1. Global behavior

The geometry, illustrated in **figure 4.2**, was used to create a first numerical model where zones ① are associated to random fibers and zones ② and ③ to aligned fibers. In this first approach, both constitutive materials of the cell are considered isotropic

Numerical results are presented in **figure 4.4**. Nominal tensile stresses were computed for each elongation step, by the sum of forces along BC divided by the initial section $S_0 = \langle e_0 \rangle \cdot \frac{l_0}{2}$ with $\langle e_0 \rangle = 0.4\text{mm}$ and $l_0 = 10\text{mm}$. Blue or red dots refer to two different directions of loading: D_1 and D_2 . Both numerical results are fitting well to the experimental curves (dashed lines). Anisotropy of the

pattern observed in the previous chapter is successfully reproduced with this first model. The particular geometry of the cell seems to trigger a different mechanical answers along loading directions. Slopes calculated with the first increments at small strain indicated a ratio of 3.5. Anisotropic ratio was found slightly smaller with numerical model, compared to the experimental value of 4.2 (**chapter 3**).

Finite element simulations of honeycomb scaffolds are successfully converging until different steps for D_1 and D_2 meshes. Simulation in D_1 direction (blue dots) is stopping at step n°22 corresponding to a global true strain of 13.7 % whereas a longer elongation can be reached in D_2 direction (step n°36: global true strain of 21.5 %).

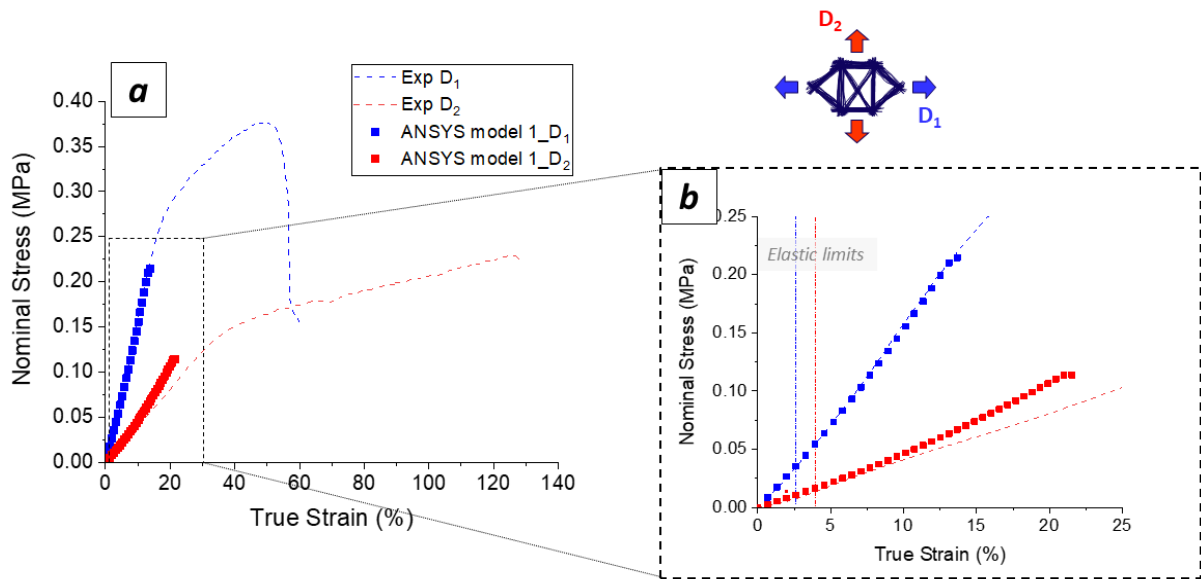


Figure 4-4: Nominal stress vs True Strain of honeycomb scaffolds in D_1 direction (blue) and D_2 direction (red), dashed lines refer to the experimental data (chapter 3) and squared dots to numerical data

4.2.1.2. Analysis of honeycomb sample in D_1 direction

Figure 4.5 represents the Von Mises equivalent strain map of the deformed membrane at a step n°19, corresponding to a global true strain value of 12 %. Structural materials locally undergo much more elevated strains compared to the global true strain. Local true strain reaches a maximum value of 51.6% depicted in red on the color map. **Figures 4.5.b** and **4.5.c** show enlarged images of the upper and bottom parts of the structure. Maximal concentrated zones are located in the isotropic zones ①, random fiber liked materials. More precisely, strains are high in the curved corners of these zones.

Moreover, it can be noticed that higher values of strain are observed on the up-right side of the sample, which corresponds to the extremities of the real mechanical samples, where shear effects would be maximal. In the upper domain, strains are maximal in the right situated corner in isotropic zone ① (green dashed circle in **figure 4.5.b**) due to the fixed position imposed by the top boundary conditions.

These colored maps show that local strain values are lot superior to actual elastic limit defined previously for aligned and random fiber liked materials (around 10 %). The actual model thus is only relevant for the first few steps, corresponding only to a few percent of global true strain. Elastic limits where the linear elastic behavior is locally respected (local strain inferior to 10 %) are plotted for both directions D_1 and D_2 in **figure 4.4.b**. In the rest of the study, we will focus of the first part of the model, plotting deformed maps at lower steps, corresponding to the limit of the elastic domain at a local scale.

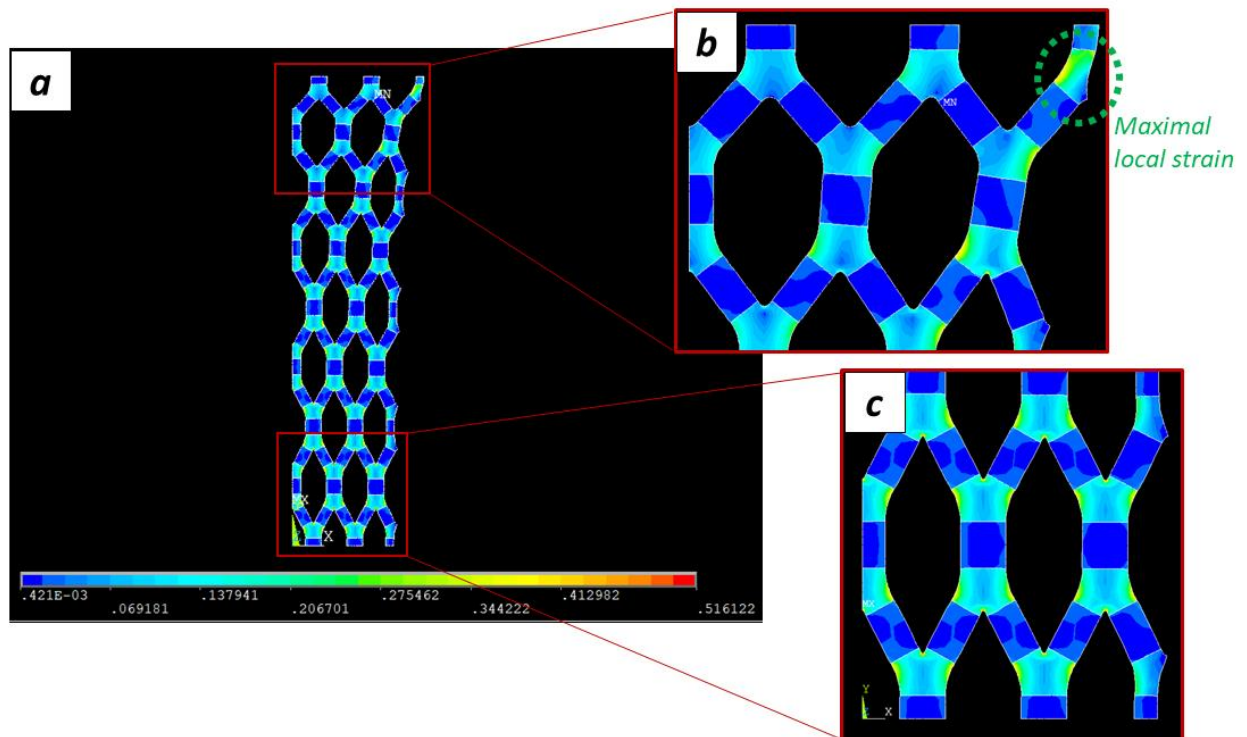


Figure 4-5: Deformed map of honeycomb scaffolds at 12 % of true strain (step n°19): Von Mises equivalent strains (MPa)

To have a better understanding of the local behavior of the honeycomb cell, values of local true strain were investigated at the central quarter cell shown in **figure 4.1.c**. **Figure 4.6.a** defines a path (red dashed line) in this area to illustrate local deformation of materials. Note that the colored map corresponds to a lower value of global strain (step n°4), where the local elastic hypothesis is still valid. Von Mises equivalent strains are plotted in **figure 4.6.b** along the path from 0 to 1.4 curvilinear abscissa for each step varying from 1 (blue) to 20 (red). Curves exhibit two peaks referring to the location of zones ①, showing again that deformation occurs in the zones ① rather than zones ② and ③.

Material is deforming more in the mechanically softer zones ①. Maximum strain values of 52 % and 39 % are reached at the final step n°20 in the peak zones (respectively $S=0$ and $S=0.85$). However, zones ② and ③ always exhibit local strain values lower than 5 % regardless of the imposed displacement.

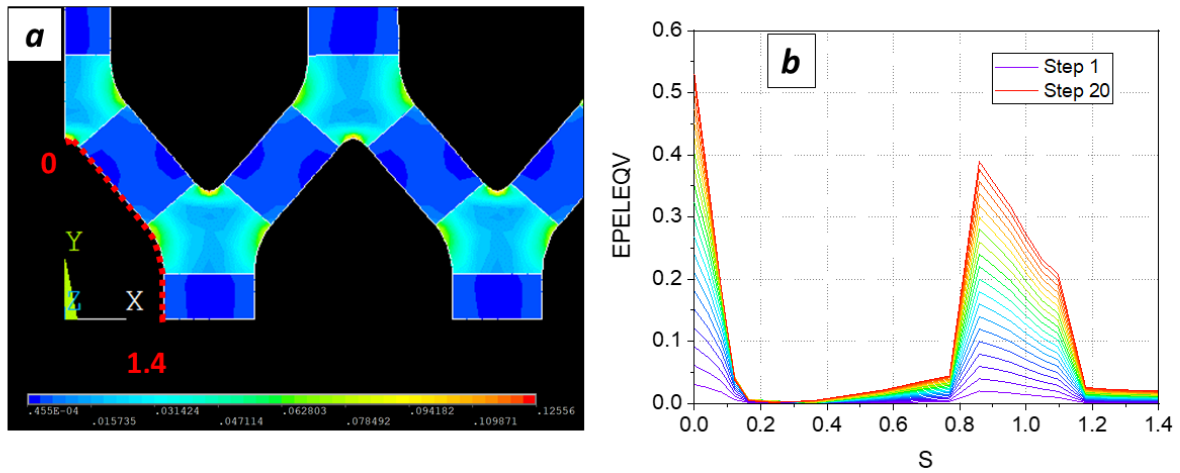


Figure 4-6: a) Deformed map (step $n^{\circ}4$, global true strain of 2.6 %) of honeycomb scaffold, left-bottom part (center of mechanical sample) with created path (red dashed line) b) Von Mises equivalent strains along the plotted path (curvilinear abscissa S from 0 to 1.4) (steps 1 to 20)

Figure 4.7 shows the first steps of the numerical data in which elastic behavior hypothesis is still valid locally (true strain inferior to 10 %). Von Mises equivalent strains are plotted in figure 4.8.b along the same defined path (constructed from the selected nodes in yellow in figure 4.8.a). At the first peak ($S=0$), true strain is superior to 10 % from the step $n^{\circ}4$. Consequently, only the first 3 steps can be rigorously taking into account if we consider than all materials behave purely elastically.

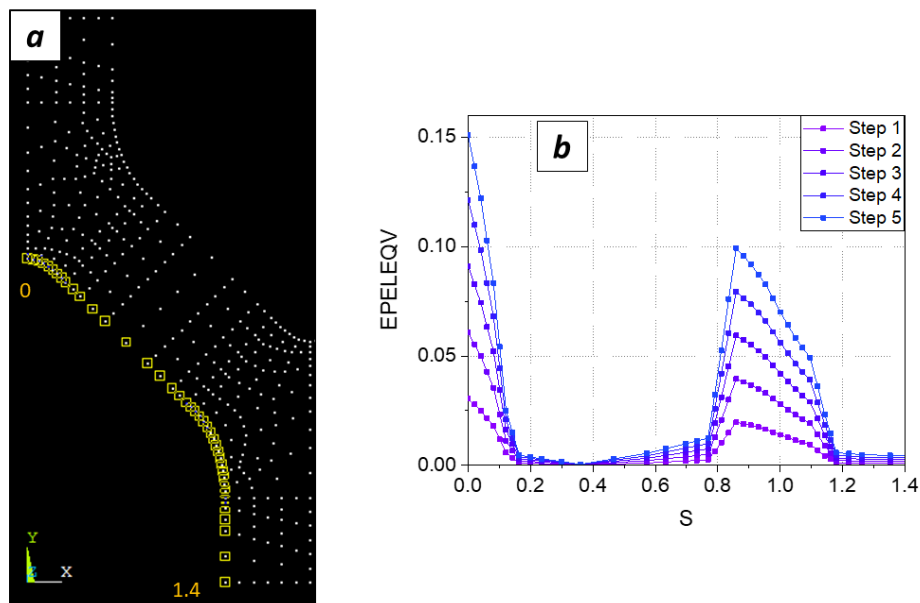


Figure 4-7 : a) Nodes constructed on the initial honeycomb cell (central zone) with the defined path in yellow, b) Von Mises equivalent stresses along the path for 5 first steps of the model

4.2.1.3. Analysis of honeycomb sample in D_2 direction

Figure 4.8 illustrates the deformed patterned membranes in the direction D_2 . Colored map with Von Mises strains is plotted in **figure 4.8.a** at a step n°6, corresponding to a global true strain value of 3.9%. As in the D_1 direction, strains are localized in the branched zones ①. Maximum values of local strains are concentrated in the curved corners as shown in the higher magnification images of the upper and bottom parts of the structure (**figures 4.8.b** and **4.8.c**).

Figure 4.8.d shows the values of Von Mises Strains along the path plotted in **figure 4.8.c**. Curves from step n° 0 to 34 are plotted. Two peaks of the curves correspond to the area of the zones ① ($S=0$ and $S=0.9$). Globally, values are smaller than the D_1 direction at a given step. Within the second zone ① (S varying from 0.8 to 1.2), maximum local true strain in D_1 is 20 % whereas in D_1 direction (step n°34), local true strain reaches 40 % (step n°15). Honeycomb patterned scaffolds undergo less local deformation in D_2 direction, which could explain the fact that the numerical simulation computes at longer global strains.

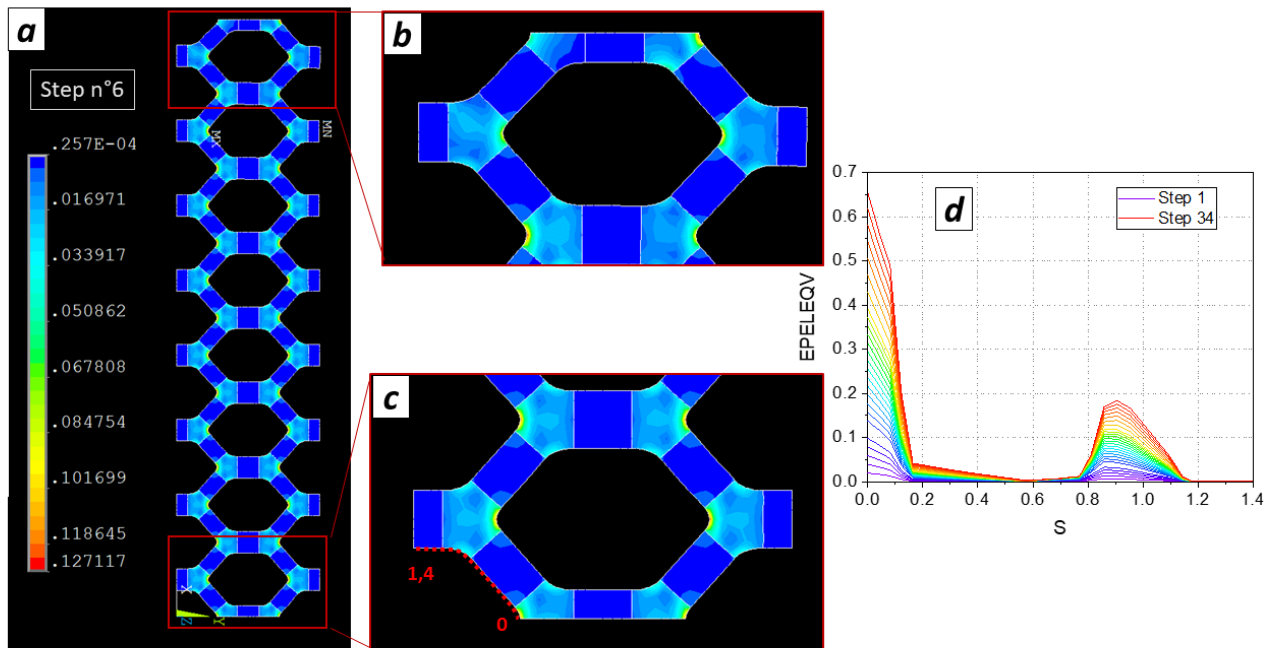


Figure 4-8: Deformed map of honeycomb scaffolds at 3.9 % of global true strain (step n°6): Von Mises equivalent strains (MPa) a) quarter of sample, b) top and c) bottom parts d) Curves of Von Mises equivalent strains along path (steps 1 to 34)

4.2.1.4. Analysis of the local transversal cell deformation

Local strains were calculated from the central cell of the patterned sample, in the case of the numerical model from the quarter of cell situated at the left bottom of the structure (figures 4.6.a or 4.7.a).

Figure 4.9.a represents the local transverse strain calculated from experimental and numerical tensile tests (defined in section 3.1.5). Shapes of the curves are initially fitting for both directions. Nevertheless, numerical data rapidly deviates after a few steps from experimental curves. Initial deformation of the central elementary cell is relatively accurate for the first 5 steps but it is not relevant at large deformation. Elastic limits where the linear elastic behavior is respected locally are plotted for both directions D_1 and D_2 . However, the global tendency (initial slopes and anisotropy between directions D_1 and D_2) is still maintained and truly reproduced.

Same results are obtained for the relative variation of surface calculated during deformation in figure 4.9.b. Numerical data show a clearly opposite behavior in D_1 and D_2 directions. In D_2 direction, the surface is continuously increasing in the numerical model. This rarely observed phenomenon, opposite to a normal membrane contraction, might be due to the specific structural aspect of the honeycomb cell. It can be related to similar behaviors of auxetic materials, which exhibit a negative Poisson's ratio. In our case, transversal strain is still negative but the global surface is expended.

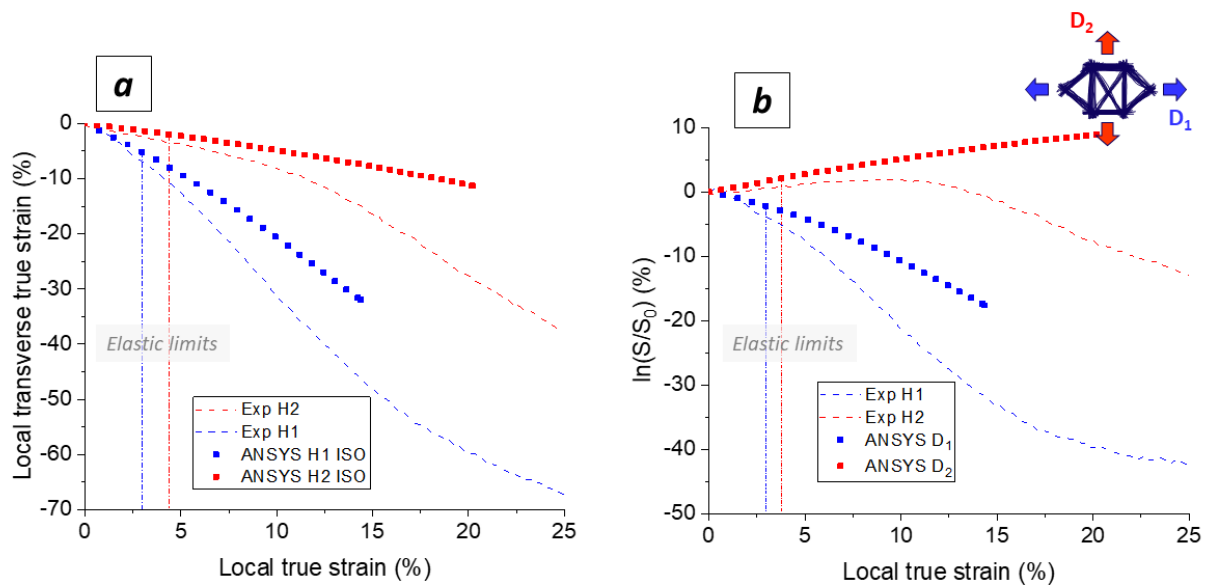


Figure 4-9: Experimental and numerical results of local strain measurements: a) transverse strain evolution b) surface variation vs local true strain

4.2.2. Model 2: orthotropy for aligned fibers zones

This section is dedicated to an extension of the previously described model 1. In this new finite element simulation, zones ② and ③ are now considered as orthotropic materials rather than isotropic. It is well known that aligned fibers respond mechanically in function of the load direction. The new orthotropic model 2 is first introduced and numerical results are later compared to previous computed data (experimental and numerical results).

4.2.2.1. Orthotropic model

Zones ② and ③ are structural components of patterned membranes which are assimilated to unidirectional aligned fibers. In the first approach, an isotropic material was defined in these zones. However, it is obvious that properties of such materials are highly dependent on fiber orientation. Therefore, an extension of the previous model was implemented to take into account the orthotropic behavior of the aligned fibers.

Materials in zones ② and ③ are from now considered as an orthotropic material. Unlike isotropic materials which are defined only by a single Young modulus E and a Poisson's ratio ν , orthotropic materials exhibit 3 different Young modulus (E_1, E_2, E_3) in 3 orthogonal directions and 6 Poisson's ratio ν_{ij} (for $i \neq j$). Young's modulus E_i gives the stiffness of the material when loaded in direction i . Poisson's ratio ν_{ij} gives the contraction in direction j when the extension is applied in direction i .

Orientation of the fibers was defined along the axis 1 as shown in **figure 4.10.a**. It is important to properly specify orientations to construct appropriate orthotropic models. Anisotropy is added in zones ② and ③ by rotating the Cartesian system in order to align axis ① to the direction of the fibers. Arrows in **figure 4.10.b** indicate the orientation of the fibers in orthotropic regions.

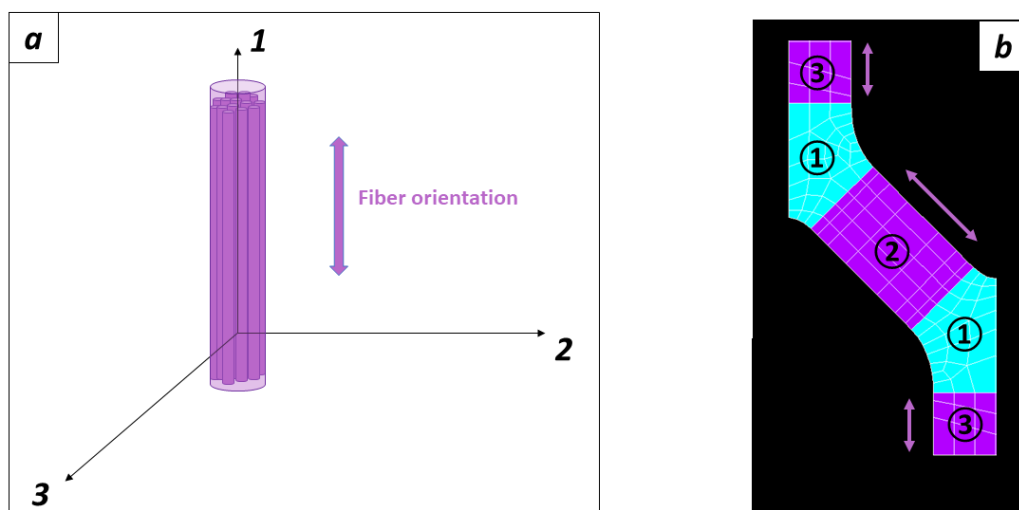


Figure 4-10: a) Quarter of honeycomb cell with fibers orientation (arrows) in zones ② and ③, b) Definition of orthogonal axis 1, 2 and 3 for orthotropic model

Pure elasticity behavior model is again employed in which the following Hooke's law might be used.

$$\sigma = C_{ortho} \varepsilon \quad (4.1)$$

6x6 elasticity tensor C_{ortho} links the stress σ and the strain ε via the **equation 4.1**, where σ and ε have 6 values referring to 11, 22, 33 normal components and 12, 23, 31 shear components.

In the case of orthotropic materials, the elasticity tensor can be defined as following.

$$\begin{bmatrix} \varepsilon_{11} \\ \varepsilon_{22} \\ \varepsilon_{33} \\ 2\varepsilon_{12} \\ 2\varepsilon_{23} \\ 2\varepsilon_{31} \end{bmatrix} = \begin{bmatrix} 1/E_1 & -v_{12}/E_1 & -v_{13}/E_1 & 0 & 0 & 0 \\ -v_{21}/E_2 & 1/E_2 & -v_{23}/E_2 & 0 & 0 & 0 \\ -v_{31}/E_3 & -v_{32}/E_3 & 1/E_3 & 0 & 0 & 0 \\ 0 & 0 & 0 & 1/\mu_{12} & 0 & 0 \\ 0 & 0 & 0 & 0 & 1/\mu_{23} & 0 \\ 0 & 0 & 0 & 0 & 0 & 1/\mu_{31} \end{bmatrix} \begin{bmatrix} \sigma_{11} \\ \sigma_{22} \\ \sigma_{33} \\ \sigma_{12} \\ \sigma_{23} \\ \sigma_{31} \end{bmatrix} \quad (4.2)$$

The system is determined by 9 free parameters:

- 3 different Young moduli E_1, E_2, E_3 , one for each orthogonal direction
- 6 Poisson's ratios v_{ij} , only 3 are independent according to the following **equation 4.3**

$$\frac{v_{ij}}{E_i} = \frac{v_{ji}}{E_j}, \quad \text{for } i \neq j \quad (4.3)$$

- 3 shear moduli μ_{12}, μ_{23} and μ_{31}

Zones ② and ③ are assimilated to a bundle of fibers, connecting two peaks and forming a bridge. Thus, the material can be defined as transversely isotropic. A material is transversely isotropic when two of three orthogonally directions are equally stiff. If the fibers are aligned towards axis 1 direction (i.e. 11), then the material is isotropic in the crossed plane (O_{23}) (values of moduli E_2 and E_3 are equal). For such a material, there are only 5 free parameters to entirely describe the system.

- $E_L = E_1$
- $E_T = E_2 = E_3$
- $v_{TT} = v_{23} = v_{32}$
- $v_{TL} = v_{31} = v_{21}$
- $\mu_{LT} = \mu_{12} = \mu_{31}$

Here, longitudinal (L) direction refers to the fiber axis 1 whereas transversal directions (T) are both 2 and 3 axis. The remaining parameters can be calculated as following.

- $v_{LT} = v_{12} = v_{13} = \frac{v_{LT} * E_L}{E_T}$
- $\mu_{TT} = \mu_{23} = \frac{E_T}{2(1+v_{TT})}$

Table 3.1 details the values of the 5 free parameters required to fully describe the system. Young moduli E_T and E_L were extracted from experimental data on aligned fibers. Young moduli values of 56 MPa and 0.18 MPa were retained in longitudinal L and Transversal T directions respectively (i.e. an anisotropy ratio of 311). Poisson's ratios were estimated from fibrous wood material properties [179], a common orthotropic and transversal isotropic material. Last shear modulus value μ_{LT} was estimated via the Huber's formula (4) [180]. The geometric mean of E_i and E_j is employed here to predict shear moduli of orthotropic materials.

$$\mu_{ij} = \frac{\sqrt{E_i E_j}}{2(1 + \sqrt{\nu_{ij} \nu_{ji}})} \quad (4)$$

E_L (MPa)	E_T (MPa)	ν_{TT}	ν_{LT}	μ_{LT} (MPa)
56	0,18	0.67	0.43	$\frac{\sqrt{E_T E_L}}{2(1 + \sqrt{\nu_{TL} \nu_{LT}})} = 1.55$

Table 4-2: Five free parameters of orthotropic and transversely isotropic material (aligned fibers liked material)

Finally, **table 3.2** summarizes the 9 parameters for the orthotropic material (zones ② and ③) implemented in the finite element simulation. Young moduli and shear moduli are expressed in MPa.

E_1 (MPa)	E_2 (MPa)	E_3 (MPa)	ν_{12}	ν_{23}	ν_{31}	μ_{12} (MPa)	μ_{23} (MPa)	μ_{31} (MPa)
56	0.18	0.18	0.001	0.67	0.43	1.55	1.05	1.55

Table 4-3: Material properties of orthotropic zones

Zones ① were defined as before as isotropic material, with a Young modulus value of 6MPa and a Poisson's coefficient of 0.46.

4.2.2.2. Global behavior

Numerical results of the model n°2 are detailed in this section. Same honeycomb geometry, boundary conditions and finite element meshing were employed with the implementation of orthotropic properties for the zones ② and ③.

Figure 4.11 shows the finite element results obtained with the model n°2. Hollow squared dots illustrate the mechanical answer to an applied loading in D_1 and D_2 directions (respectively blue and red curves). The introduction of orthotropic properties in zones ② and ③ has a global tendency to

lower Nominal Stress. Stress values are decreased by 30 to 40 % compared to a fully isotropic model in both directions. The finite element simulation using new model n°2 does not converge as far as the isotropic model, especially for D_1 direction where simulation stops at a smaller step n°15, corresponding to 9.5 % of global true strain.

Elastic limits (linear behavior at local scale) are plotted for the model 2 in the **figure 4.11**. Deformed maps, later illustrated in the section, exhibit lower values of local strains pushing the elastic validity of the model to further steps in D_1 and D_2 directions (step n°5 and 8).

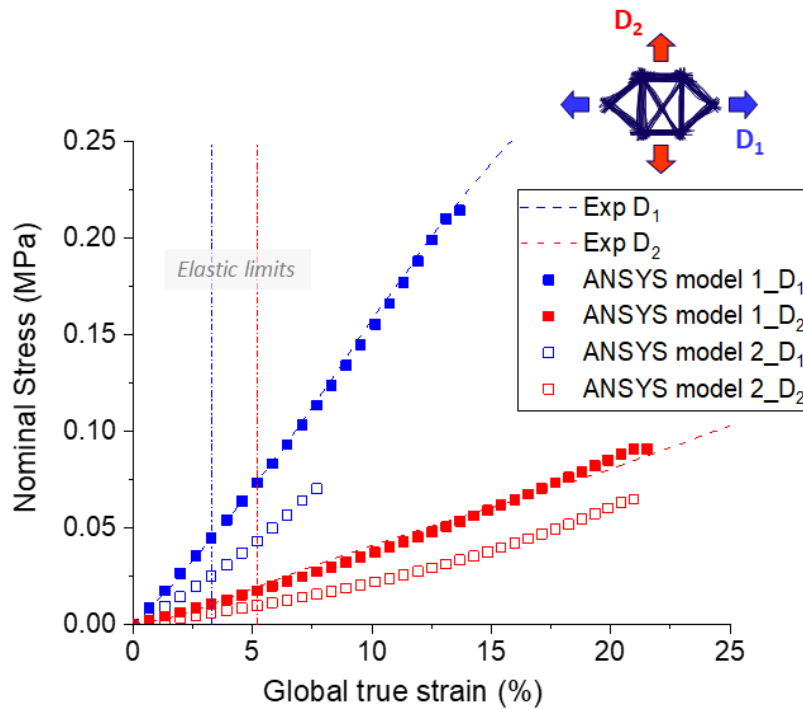


Figure 4-11: Experimental and numerical data of Nominal Stress of honeycomb scaffolds in D_1 and D_2 direction (respectively blue and red curves). Dashed lines: experimental data (chapter 3), square dots isotropic model, empty square dots: orthotropic model.

4.2.2.3. Analysis of honeycomb sample in D_1 direction

Figure 4.12 shows the deformed map (Von Mises strains) of honeycomb scaffolds in D_1 direction at step n°5 (global strain of 3.3 %) with numerical results of model n°2. The highest value of local strain is still located in the right upper part of the mechanical sample (**figure 4.12.b**). Maximum local strain colored in red is located in zone ③ (dashed green circle), induced by the locked position of top nodes layer.

High strains are localized similarly to model 1 along the corner in the zones ①. Strain curves along the defined path on **Figure 4.12.d** show two sharp peaks corresponding to the zone ① corners ($s=0$ and 0.9) of the central unit cell. Values of local strains at these locations (28 % and 22 % for step n°15) are still lower than the maximum value (37 % for step n°15) observed at the upper part. The structure is clearly more deformed locally at the vicinity of the grips.

The new model properties provoke an increase of local strains in the aligned zones ② and ③. These areas exhibit different colors on the maps than in the previous model. Bridges oriented at 45° (zones ②) show higher deformation (green color) as they are not directly loaded in the direction of the fibers. However, bridges aligned to the loading direction are working in longitudinal direction. As the Young modulus for an orthotropic material is stronger in the fiber direction, low deformation occurs revealed by a blue color in zones ③.

As in the model 1, the elastic strain threshold of 10 % is rapidly not respected at a local scale. From step n°5, local true strains have larger values than the elastic strain limit. **Figure 4.12.e** compares the curve at step n°5 of the two models. It can be noticed that at a same global true strain imposed, peaks of the local strain curve are smaller in the case of the anisotropic model 2. The anisotropy introduced by model 2 brings weaker materials in the bridge zones ② and ③. Consequently, these bridge zones are more distorted which reduces the strains in the peak zones ①.

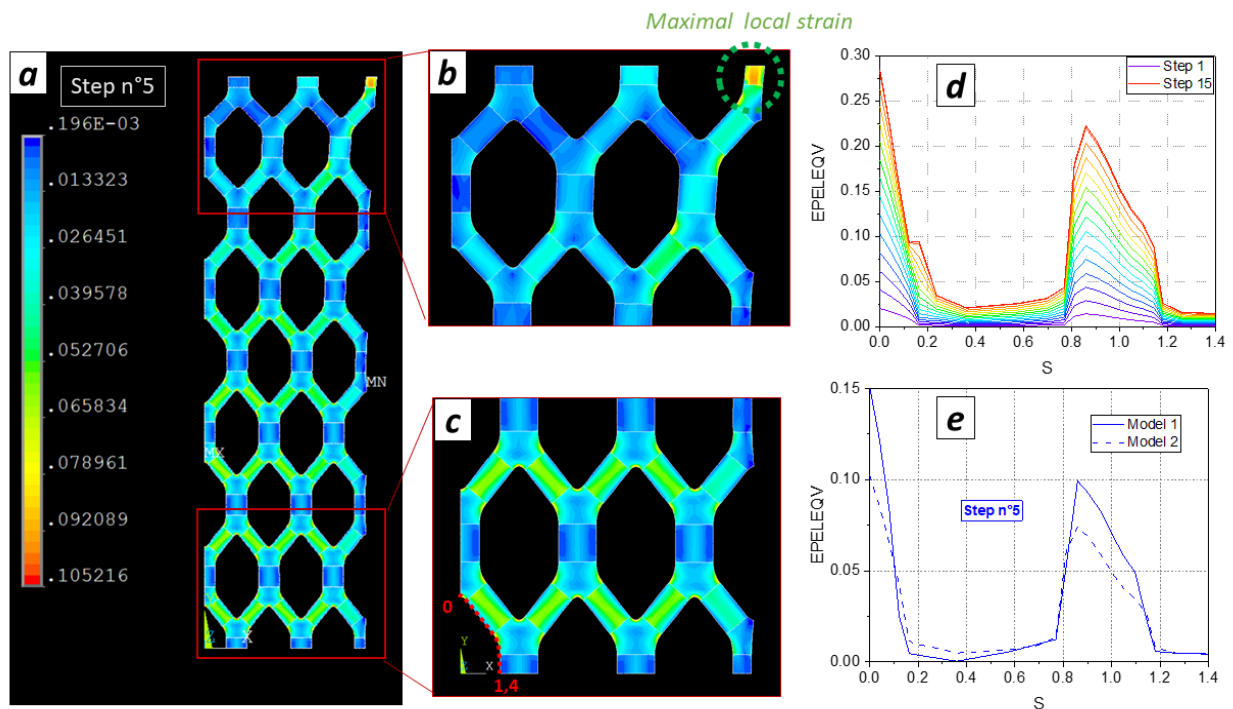


Figure 4-12: Deformed map of honeycomb scaffolds (model n°2) at 3.3 % of true strain (step n°5) in direction D_1 : Von Mises equivalent strains (MPa) a) quarter of sample, b) top and c) bottom parts d) Von Mises equivalent strains along path e) Von Mises strains for model 1 and model 2

4.2.2.4. Analysis of honeycomb sample in D_2 direction

Figure 4.13 reveals the deformation dynamics of honeycomb scaffolds in D_2 direction (model 2) at the step n°8 (global true strain of 5.2 %). Highest value is also situated at the upper part in zone ①. As in D_1 direction, high strains are concentrated in corners of the branched zones ① all over the structure. Aligned fibers of zones ② are more distorted (green color) as loading is not applied in the strong direction of the orthotropic material. In another hand, zones ③ are more elongated as before. Loading direction is oriented along the weak stiffness direction of the orthotropic material. Again overall values of strain are smaller than the ones in D_1 direction.

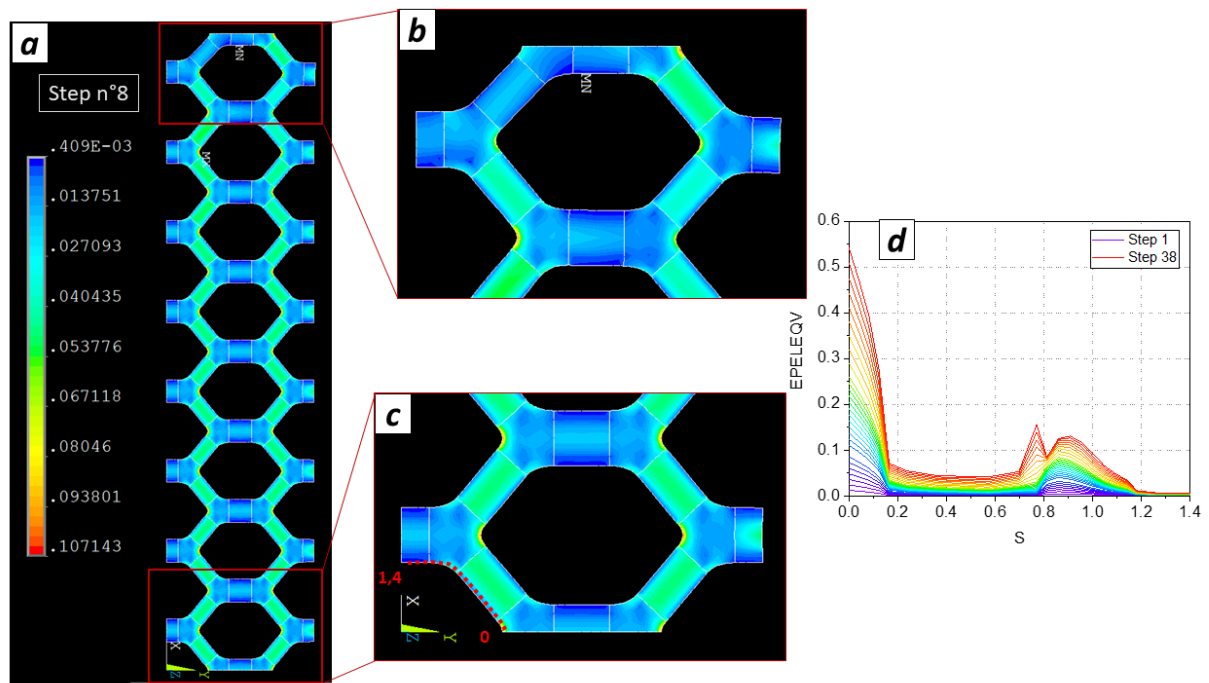


Figure 4-13: Deformed map of honeycomb scaffolds (model n°2) at 5.2 % of global true strain (step n°8) in direction D_2 : Von Mises equivalent strains (MPa) a) quarter of sample, b) top and c) bottom parts d) Von Mises equivalent strains along path

4.2.2.5. Analysis of the local transversal cell deformation

Figure 4.14 exhibits the local measurement of true strain on the model 2. In both directions, no changes are observed between the two finite element models. Initial slopes of transverse strain and surface variation are following the same tendency. Slight improvement can be noticed with model 2 as local transverse strain is increased after a few steps, which brings closer to the dashed experimental curves.

Elastic boundaries are plotted for the model 2 for the step n°5 and n°8 (respectively for D_1 and D_2 directions) showing that assumption of linear elasticity model is rapidly not valid.

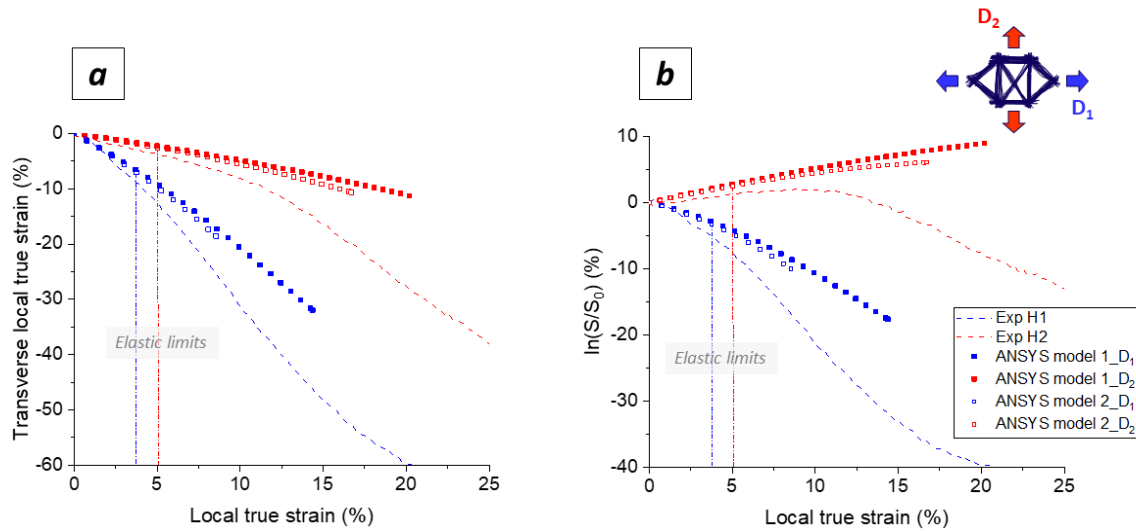


Figure 4-14: Experimental and numerical results of local strain measurements: a) transverse strain evolution b) surface variation vs local true strain. Dashed lines: experimental data (chapter 3), square dots isotropic model, empty square dots: orthotropic model.

4.2.3. Conclusion

Finite elements models 1 and 2 were successfully designed to reproduce the mechanical tensile tests over a full mechanical sample. Both models reproduce the mechanical anisotropy of the patterned material between the two loading directions. Linear elasticity assumption, from which models are built, becomes rapidly not valid as local true strain values are higher than the strain elastic limit set experimentally at 10 % for both random and aligned fibers. Both models are only valid for first few steps to stay entirely in the small strains window. Model 1 is surprisingly fitting well the experimental curves even if zones ① and ② are simply defined with isotropic behavior. Model 2 seems to underestimate the global mechanical strength of the honeycomb structure. It globally decreases the local strains extending the elastic limits. Model 1 was finally selected for the rest of the numerical analysis as model 2 did not bring better forecasts for honeycomb patterned scaffolds.

4.3. Influence of electrospinning process on anisotropic behavior of honeycomb scaffolds

4.3.1. New geometric model of honeycomb scaffolds

Next section is dedicated to a specific study of the anisotropy of the honeycomb scaffolds. This analysis was stimulated by the unexpected mechanical results found with the new polymer batch B (**chapter 3**). The sudden loss in anisotropic behaviors for the newly produced electrospun scaffolds target a new design of the elementary cell. Before, no fibrous material was considered in the central zone of the cell (dark blue zone ④) as described in **figure 4.15.b**). However, it has been observed on SEM images that a few fibers can be actually deposited in this central area of the honeycomb cell (**figures 2.10.3** and **2.10.4**).

A new geometry was then defined with a new zone ④, by filling the gaps of the previous geometry. An isotropic material was considered in a first approach for these new areas with a varied Young modulus E_{centre} , a Poisson's coefficient of 0.46 and a thickness of 0.1 mm. Same parameters of model 1 were preserved for aligned and random fibers zones ①, ② and ③).

Figure 4.15.a shows a deformed map of the new structure at a global true strain of 3.9 % ($E_{centre} = 1\text{MPa}$). Local strains are high in the central zone ④ (easiest material to deform), along the curves corners of the honeycomb branch.

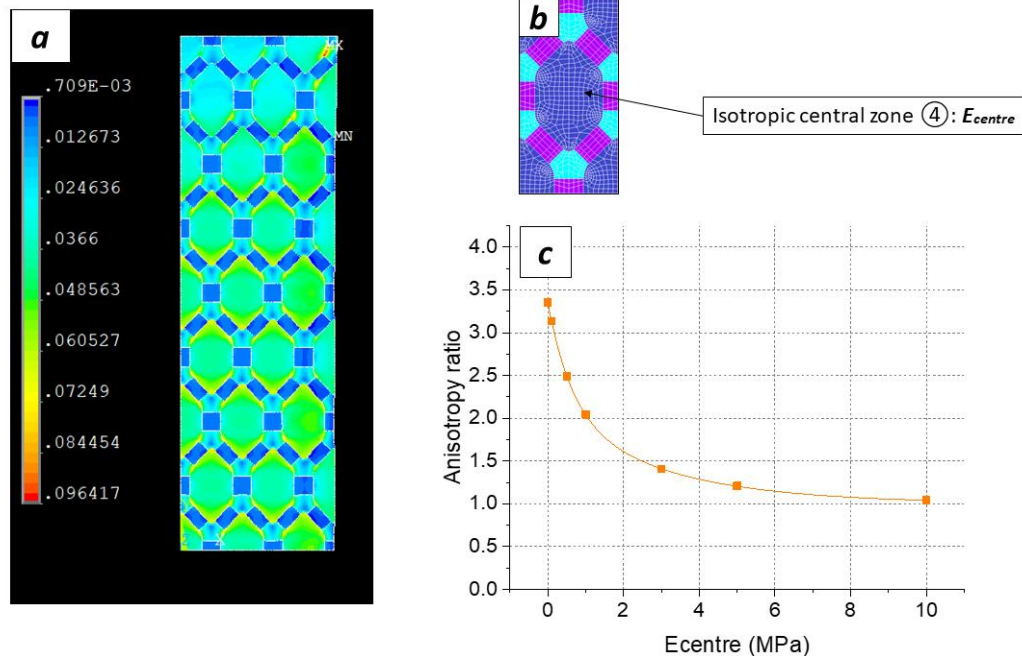


Figure 4-15: Anisotropy study of honeycomb scaffolds: a) deformed map of honeycomb scaffolds with central isotropic material ($E_{centre} = 1\text{MPa}$) at 3.9 % of true strain (color map: Von Mises strains) b) new geometry with variable isotropic material at the mesh center (zones ④) c) anisotropy ratio in function of E_{centre} : Young modulus of the zone ④

Anisotropy was analyzed through the ratio between the two initial slopes of the stress strain curves in direction D_1 and D_2 . Ratios were calculated with different E_{centre} values from 0 to 10 MPa (**figure 4.15.c**). Anisotropy rapidly decreases with increasing value of Young modulus of the zone ④. As soon as a material is considered in this central area (few fibers), anisotropy is reduced. It even disappears at a value of 10 MPa where ratio is equal to 1. This numerical experience proves the importance of the central zone in the mechanical behavior of the honeycomb structure. Results experimentally found with the polymer batch B can be explained by the presence of fibers in the central area. Optical images showed fibers across the central gap of honeycomb cell, few fibers that might suppress the anisotropy behavior of the entire scaffolds.

4.3.2. Experimental validation

After noticing the crucial role of zone ④ by the finite element program, new mechanical tests were performed on honeycomb electrospun membranes (batch B). A post treatment was applied to these isotropic fibrous scaffolds with a localized thermal effect. The objective was to remove/suppress fibers from central zones to retrieve the anisotropic behavior observed with the first batch A. With the help of a soldering iron for electronics, polymer fibers were locally melt to recreate honeycomb membranes with empty central zones. Temperature of the soldering tip was set around 80°C, slightly higher than the melt temperature of PCL: 60°C. **Figure 4.16.a** shows the produced membranes after the heating post treatment. Honeycomb structure is still preserved even if morphology of the fibers is locally changed (melted areas on enlarged **figure 4.16.b**).

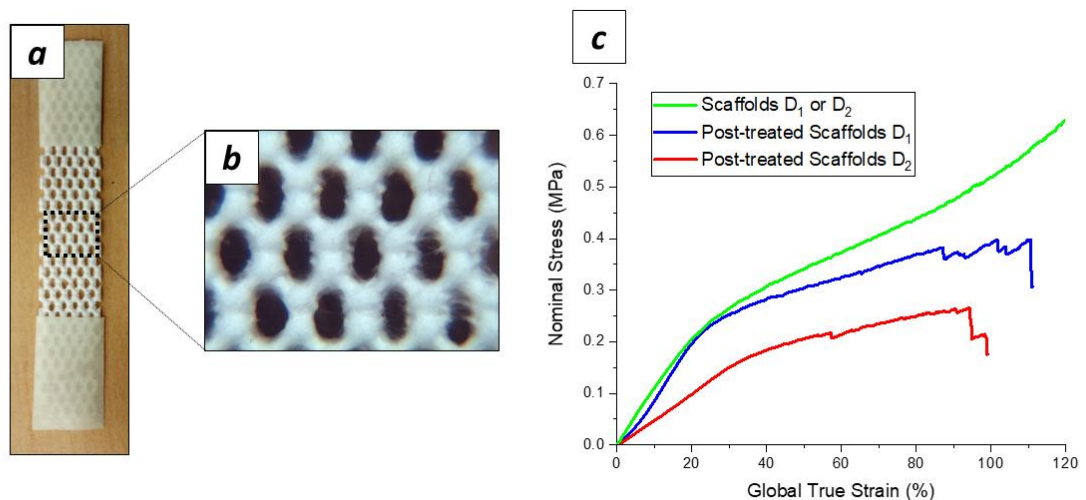


Figure 4-16: a) Pierced honeycomb membranes (thermal post-treatment) b) nominal stress curves of unpierced (green line) and pierced membranes in D_1 and D_2 direction (blue and red lines)

Results are exposed in **figure 4.16.c**. Nominal stress intensity decreases for both post treated membranes (blue and red curves) compared to initial honeycomb membranes (green curve). However,

post treated membranes behave differently regarding the direction of applied loading. An anisotropy of 2 between direction D_1 and D_2 was measured whereas no difference was observed for the initial membranes (green curve). By creating holes in fibrous membranes, the structure is closer to the honeycomb geometry used in the modeling system. The initial anisotropic factor of 4 was not retrieved, probably due to the degradation of the membrane by the heat and the degradation of the fiber network. Nevertheless, a clear dependence of the fibrous central network is highlighted here.

4.3.3. Numerical model with fibers in the central zone

Another numerical model was developed to take into account the anisotropic character of the central zone ④. Indeed, fibers are not randomly deposited in these central areas but organized to connect peaks and form secondary bridges. Smaller areas of aligned fibers were designed in the core zone as illustrated in **figure 4.17**. Geometry of these secondary bridges were constructed in agreement with microscopic images of the scaffolds (**figure 3.25.b**). Material is associated to aligned fibers with the same isotropic properties of the zones ② and ③ (model 1). Thickness of the zones ④ was varied from 0 to 0.1 mm in order to study the role of the central fibers in the mechanical behavior.

Figure 4.17.b shows the variation of the anisotropic ratio in function of the thickness of the central zones ④. As soon as fibers are considered (thickness superior to 0), anisotropy ratio of the structure decreases. Shape of the curve is similar to the one obtained previously with the isotropic central zone (**figure 4.17.c**). If the secondary bridges are reaching a thickness equals to the 0.1mm, anisotropy disappears (honeycomb scaffolds answer mechanically in the same way in direction D_1 and D_2).

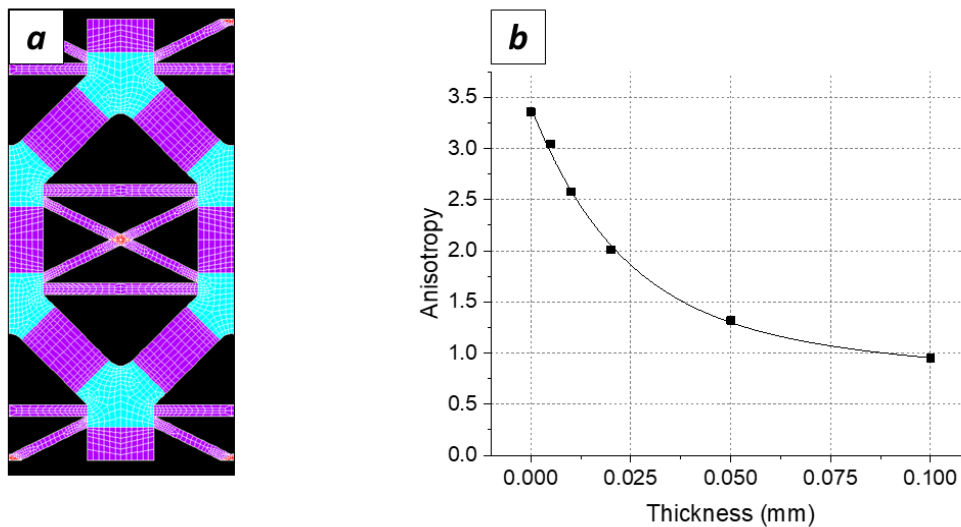


Figure 4-17: a) New geometry model with secondary bridges (zones ④) b) anisotropy ratio is function of implemented thickness of central areas (zones ④)

4.4. Modelling of square scaffolds

4.4.1. Geometric model

The finite element model developed in the previous section is now applied to the square patterned scaffolds. Geometry was designed to shape a square cell in D_1 and D_2 directions with dimensions corresponding to the optical image of square patterns (**figures 4.18.a and 4.19.a**). Following the same procedures, aligned and random fibers zones were demarcated and associated to ①, ②, ③ and ④ zones as shown in **figures 4.18.b and 4.19.b**. Two distinct areas ① and ② were associated to random fibers in the case of square patterned scaffolds. Properties of each constitutive material were taken as in the model 1 built for the honeycomb scaffolds. Only the first model 1 with isotropic behaviors is investigated as anisotropic model 2 did not bring any significant improvements. Thicknesses were attributed to the different zones depending on the 3D topography of the scaffolds. Highest thickness (zones ① and ②) was set in agreement with the measure of apparent thickness (0.6 mm for square scaffolds). Bridges thicknesses were estimated from SEM images and profilimeter scans (0.45mm for zones ③ and 0.1mm for zones ④).

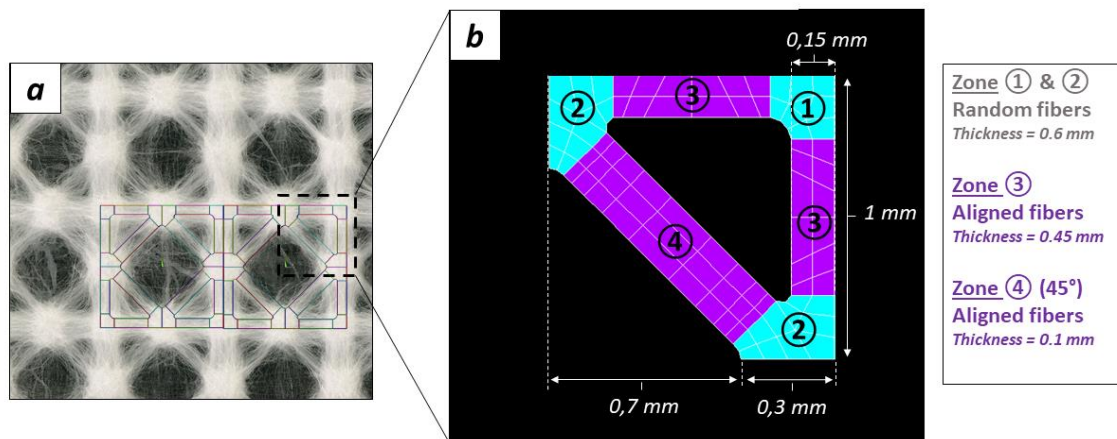


Figure 4-18: Design of the square cell in D_1 direction: (a) elementary designed pattern on optical image of square scaffold, (b) design of a quarter of the square cell with allocated area

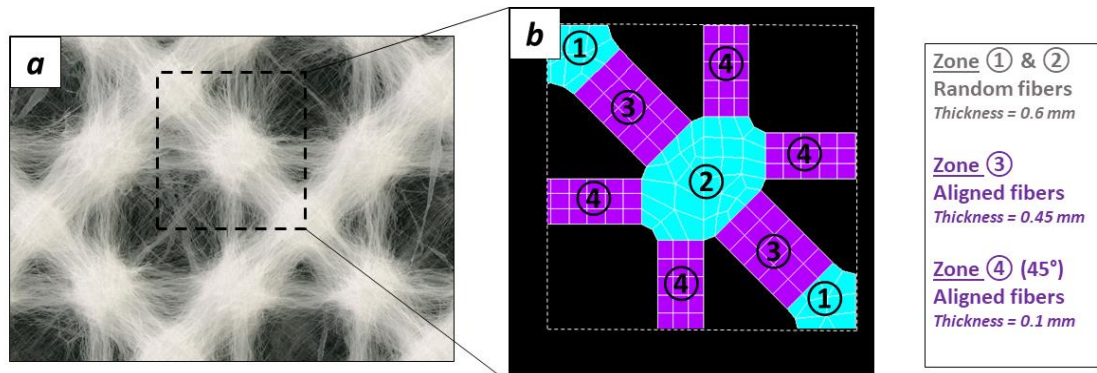


Figure 4-19: Design of the square cell in D_2 direction: (a) elementary designed pattern on optical image of square scaffold, (b) design of a quarter of the square cell with allocated areas

Quarter of sample was constructed from the quarter of the elementary cell to fit the appropriate dimension of mechanical samples used in **chapter 3**. Axial mechanical tests of squared structures were reproduced with the finite element model 1.

4.4.2. Global behavior

Figure 4.20 illustrates numerical results of the finite element model in comparison with experimental data (**chapter 3**). Nominal stresses were computed in both D_1 and D_2 directions (respectively blue and orange curves), referring to loading directions at 0 and 45°. Numerical values of nominal stress are higher than experimental data (dashed line). The finite element program certainly over estimates the mechanical answer of the square patterns.

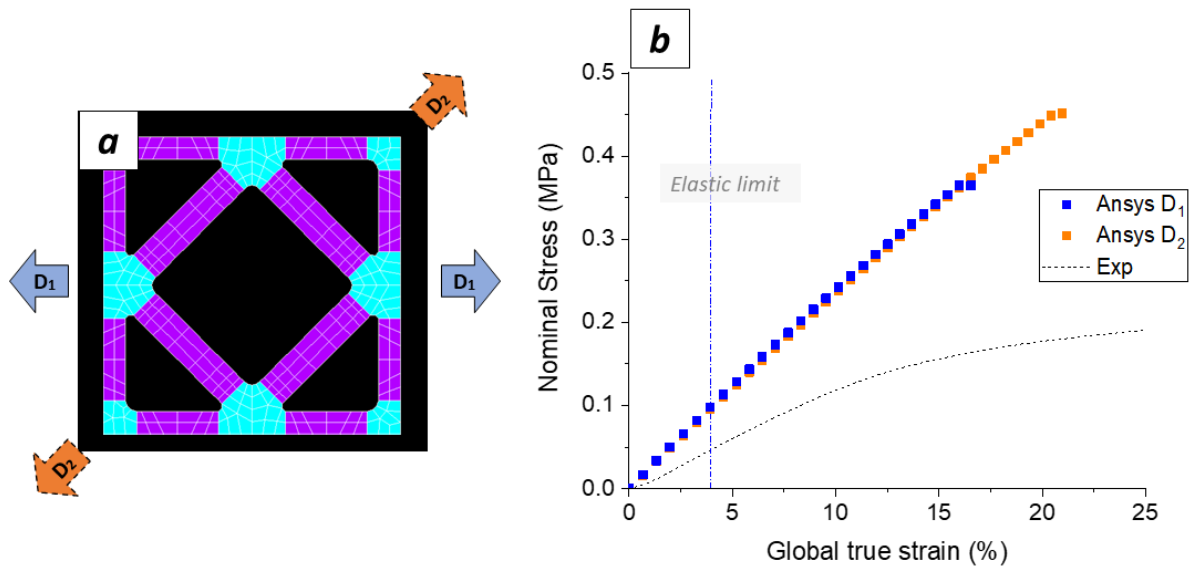


Figure 4-20: Experimental and numerical results of Nominal stress-strain curves of square patterned scaffolds in directions D_1 and D_2 (respectively blue and orange dots)

1.2.2.3. Analysis of honeycomb sample in D_1 direction

Figure 4.21.a shows the deformed map (Von Mises equivalent strains) of square pattern in direction D_1 at a global true strain of 3.9 %. In enlarged colored maps (figures 4.21.b and 4.21.c) it is clear that zones ① and ② are concentrating the highest values of local strain. Corners of the branched peak zones are revealing the maximum distortion (green dashed circle).

Figure 4.21.d represents local strains values along a specific path plotted at the center of mechanical sample (red dashed line on figure 4.21.c). The path follows the inner sides of the elementary cell in a clockwise direction (S values from 0 to 2.1). Curves are plotted for each steps (0 to 36). 3 distinct peaks appear on the graph corresponding to the high distorted zones (corners of zones ① and ②).

Local strains are rapidly larger than 10 %, elastic limit of the constitutive materials. Only the five 6 steps can be considerate for a pure elastic analysis behavior, meaning that the finite element model is relevant only until a global true strain of 3.9 %.

It can be seen that aligned fibers are behaving differently in zones ③ and ④. Fibers aligned perpendicularly (③) are quasi non distorted by the action of the loading force (zones colored in dark blue). However, zones ④, aligned fibers orientated at 45°, have a lighter blue color, evidence of a stronger resistance and effect on the global mechanical behavior of the structure.

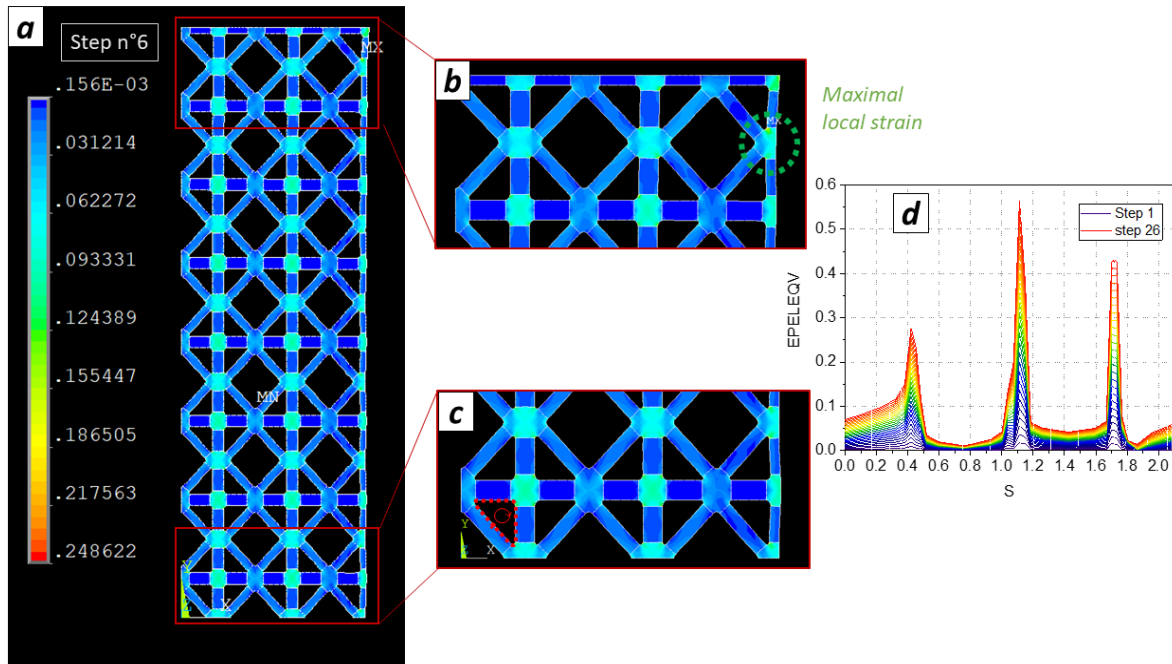


Figure 4-21: a) Deformed map of Square scaffolds at 3.9 % of global true strain (step n°6): Von Mises equivalent strains (MPa), enlarged images of b) top and c) bottom of structure d) Von Mises equivalent strains along plotted path (curvi linear abscissa from 0 to 2.1)

1.2.2.3. Analysis of honeycomb sample in D_2 direction

This importance of these secondary bridges is even more noticeable when we look at the deformation of the structure in the D_2 direction. **Figure 4.22.a** shows local strain distribution (Von Mises equivalent) of the square patterns submitted to a 45° load. Zones ④ have along the all sample high true strain values and make appear distinctly the stress lines across the structure. Maximal distortions are localized again in the corners of the zones ① and ②, which are subjected to the higher stresses in all the membranes.

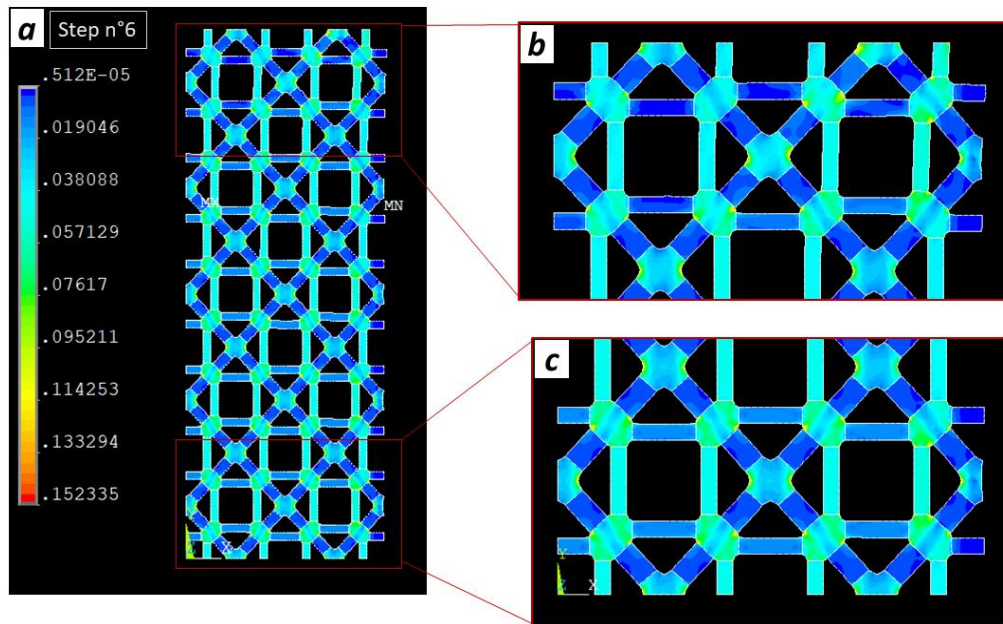


Figure 4-22: a) Deformed map of Square scaffolds at 3.9 % of global true strain (step n°6) in direction D₂: Von Mises equivalent strains (MPa), enlarged images of b) top and c) bottom of structure d) Von Mises equivalent strains along plotted path (curvi linear abscissa from 0 to 2.1)

4.4.3. Global behaviors of square scaffolds without secondary bridges

To investigate further the role of the secondary bridges (zones ④), a new geometry was designed as shown in **figure 4.23.a**. Zones ④ were removed from the pattern in order to observe the mechanical answer of hollow square cell. Numerical results were computed for both D₁ and D₂ directions (**figure 4.23.c**).

As intended, removing the secondary bridges induces a decrease in the calculated nominal stress in both directions. However, a more drastic decline is observed for the 45° direction of loading (orange squared dots). Zones ④ are thus critical components of the square matrix which greatly influences the global mechanical behavior. If only a few fibers are collected in these zones (i.e. weak thickness or Young modulus), squared pattern scaffolds can develop anisotropy and exhibit different load reactions in D₁ and D₂ directions.

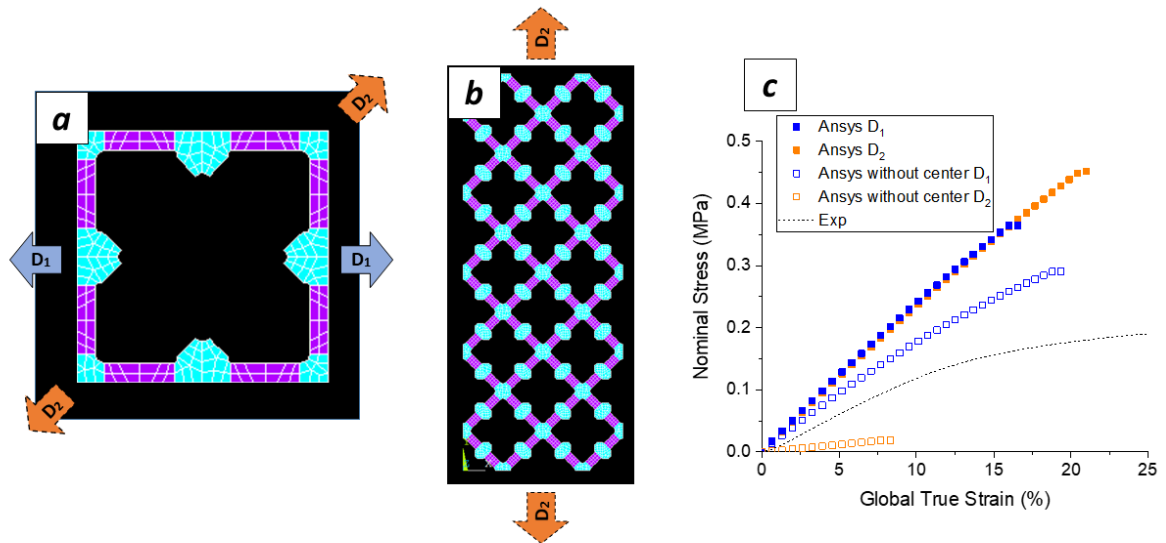


Figure 4-23: a) New square cell geometry without secondary bridges (zones ④), b) quarter sized structure (new geometry) oriented in D_2 loading direction. c) Experimental and numerical results of Nominal stress-strain curves of square patterned scaffolds in directions D_1 and D_2

4.4.4. Analysis of the local transversal deformation of the cell

Figure 4.24.a and b illustrates the local measurement of transverse strains and the surface relative variation in the two directions.

Models with the first geometry (full squared dots) in both directions are fitting well the experimental curves (black dashed lines) of local transverse strain and relative variation of the surface. This is true only for the first steps, around 7 % of local true strain where experimental curves drops while numerical ones continue quasi linearly.

When secondary bridges of the square cell are not considered (hollow squared dots), numerical results are far from experimental data. Interestingly, numerical results are diverging from the experimental values in the opposite way depending of the applied loading direction D_1 or D_2 . Relative variation of the surface becomes negative in direction D_2 in figure 4.24.b, meaning that the structure as a Poisson's coefficient superior to 1. Here again, zones ④ are a marker of anisotropy of these specific square patterned scaffolds.

Square structure without the secondary bridges (zones ④) seems very attractive if anisotropic properties are required. A new design of micro-structured collectors might be interesting to consider as in figure 2.16, especially to recreate a square patterns without zones ④. Numerical simulation is helping to think ahead and gives new insights on potential new patterns of anisotropic membranes without forgetting the experimental difficulties of fiber structuration in electrospinning.

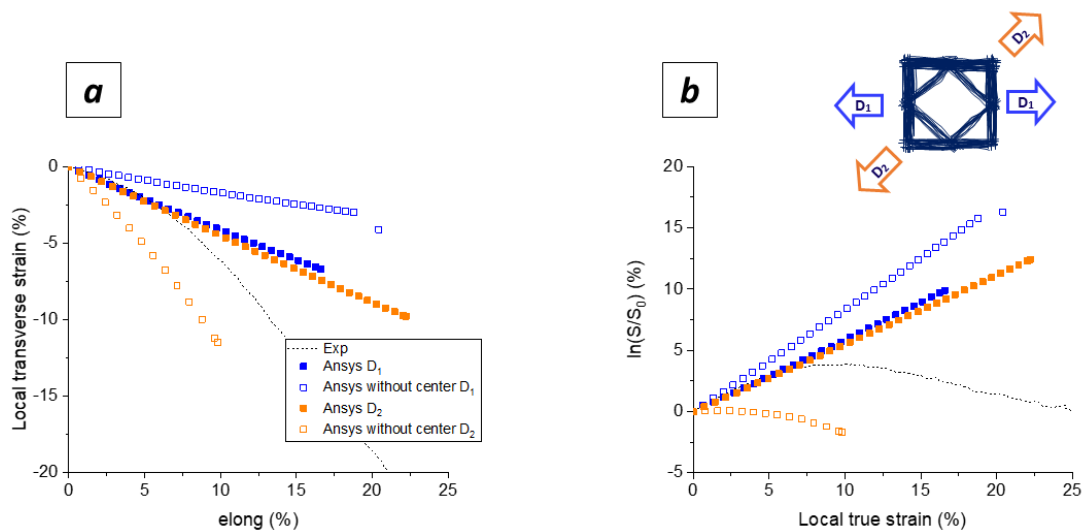


Figure 4-24: Experimental and numerical results of local strain measurements- square patterned scaffolds: a) transverse strain evolution b) surface relative variation vs local true strain.

4.4.5. Conclusion

The finite element model developed and applied to the electrospun square patterned scaffolds did not predict overall mechanical behaviors as accurately as for the honeycomb cell. Numerical results of global nominal stress are not perfectly correlated to the experiments. However, finite element model proves the importance of the inside secondary bridges (zones ④). Mechanical behaviors were found identical in both direction D₁ and D₂ which can be correlated with the non-anisotropy observed experimentally. Empty squared structures (cell without zones ④) behave completely differently and divert from the reference results (local transverse strains and relative variation of the surface dependent of loading directions). Consequently, geometry with inner zones ④ was thus preferred and more appropriate to describe electrospun scaffolds.

4.5. Conclusion numerical simulation

Finite element models were successfully constructed with a simple geometry reconstruction of the scaffold elementary patterns. Constitutive materials of the structure were identified as random and aligned fibers. Model 1, taking into account only isotropic behaviors in all defined zones, fits with good precision mechanical results found experimentally in **chapter 3**. Anisotropy of honeycomb was successfully retrieved between longitudinal and transversal directions. Introduction of a more complex anisotropic properties in the aligned zones did not show any improvement. However, anisotropy was still keep which might as well question of the initial veracity of the input data, especially the relative thickness which directly determined the nominal stress values of the construct. Numerical study with new geometry proves the importance of the central part of the elementary honeycomb patterns.

Fibers and secondary bridges need to be taken into account to describe appropriately the global mechanical behavior of scaffolds.

Finite element simulation on squared patterned scaffolds showed less similarity with experimental data. Even if values of nominal stresses were overestimated with the finite element model, global isotropic behavior of square scaffolds was retrieved for both directions at 0 and 45°.

For both structure types, local strains were found much higher than the imposed global strain which validate the model of linear elasticity only for the first steps of the simulation program (global true strain of 3 to 5 %).

A simple finite element program was proposed in this study, giving a model of reference for patterned scaffolds produced by electrospinning. Several implementations can be improved to the preexisting models. To increase veracity of numerical models, constitutive material behaviors can be defined with more complicate constitutive equations such as hyperelasticity, viscoelasticity or elastoplasticity. Cyclic tests might be then numerically reproduced and compared to hysteresis curves as obtained experimentally in **chapter 3**. Moreover, it is crucial to defined properly the elementary geometry of the scaffolds. To this end, we recommend a deeper optical analysis of the 3D scaffolds. Determining accurately the relative thicknesses of secondary bridges. Accurate porosities in each fibrous zones will as well considerably improve the numerical model. A particular attention needs to be target to the central zones of fibrous scaffolds.

5. General conclusion

Fiber structuration with an electrospinning process was successfully performed with the help of new 3D designed collectors. This study highlights the fabrication of fibrous scaffolds with honeycomb, square or rectangular patterns with a noticeable anisotropy. The method brings a new way to build organized heterogeneous materials for tissue regeneration. Structured membranes offer two distinctive fibrous zones that could create attractive structural environment for cells. Indeed, dense areas would confer required mechanical strength to the global framework. Network of bundles made of aligned fibers can be monitored in order to obtain specific mechanical properties adapted to soft tissues. Besides, low dense zones with apparent lower porosity would provide a favorable environment where cells could penetrate in depth and proliferate.

Mechanical characterization was carried out on honeycomb and square patterned structures in two different loading directions. Anisotropic ratio of elastic modulus of 4.2 was found for honeycomb scaffolds between transversal and longitudinal directions matching to the range of soft tissue structural properties. Furthermore, mechanical tests showed an isotropic behavior in the case of square patterned scaffolds when samples are pulled at 0 and 45 directions. Fibers presence in the center part of the cell seems to be a key parameter triggering mechanical properties and anisotropy behaviors of electrospun scaffolds. Finite element models were successfully constructed with a simple 2D geometry reconstruction of the scaffold elementary patterns. Constitutive materials of the structure were identified as random and aligned fibers. Numerical study with new geometry proves the importance of the central part of the elementary patterns to the nominal stress measurements. Fibers and secondary bridges need to be taken into account to describe appropriately the global mechanical behavior of scaffolds. Mechanical behaviors (anisotropy of honeycomb mesh and isotropy of squared scaffolds) were successfully reproduced.

Nevertheless, the work of this thesis can still be improved and completed in order to bring a new level of knowledge on anisotropic electrospun scaffolds. Here are detailed a few perspectives to develop on electrospun fibers in better scaffolds.

Structured materials were successfully fabricated by electrospinning but stronger knowledge in fiber structuration method is still required to grow thicker architected scaffolds. Fiber organization in depth gets worsen with increasing time of collection. A more meticulous study of electrospinning conditions, with especially better controlled in humidity and temperature might facilitate the regular formation of structures. Porosity of the membranes is a crucial parameter which directly determines the well-being of cells within the scaffolds (good colonization within the whole network). Thus it is important to be able to control local porosities of the different zones of the patterned scaffolds. A more thorough optical analysis of the 3D constructs via micro tomography or confocal microscopy might give valuable data of the local fiber arrangement. More specifically, porosities and accurate local thicknesses would be available for the numerical model developed in **chapter 4**. A particular attention needs to be focused on the change of porosity in depth. Indeed, due to a change of local electric field (creation of

an insulating layer by accumulated fibers), fibers are deposited in a different mode inducing a non-homogeneous porosity through the thickness of the membrane.

As scaffolds are aiming to replace tissues, biological response still needs to be analyzed. Investigation of cell interactions with honeycomb or square patterned scaffolds is a very next important step to follow. Will cells adhere adequately and penetrate inside the membranes? Will they spread all over the different zones or concentrate preferentially in the low dense fiber zones creating preferential niches where cells proliferate? There are numerous important biological properties to validate for the use of these fibrous materials for tissue regeneration applications.

As the finite element model developed in this study relies on very simple elastic behavior theory of constitutive materials, this model has to still be improved. A closer study of the constitutive material of patterned scaffolds, i.e. random and aligned fibers, might bring new results to develop more complex models with hyper elasticity, viscoelasticity or elasto-plastic mechanical behaviors. A study of cyclic loads might bring new outcomes for the design of new patterned scaffolds that meet the high demands for regenerative medicine.

A scale up in the XY plane of the electrospun membranes might be interesting to consider. Extension of collection surface by a motorized collector system can increase fabrication efficiency. Slow and repetitive movements would allow the projection of fibers over a larger surface (considering the development of larger micro-structured collectors). However, new motions of the collector might affect the deposition mechanism of the protrusions, even if the speed of the fiber in electrospinning is considerably higher than the XY speeds, requiring more research on this problematic.

Design of more complex microstructures might be considered to bring different mechanical properties to the scaffolds. Numerical model is here a wonderful tool to create new patterned structures. New specific mechanical properties can be anticipated before launching the fabrication of new micro-structured collectors. A particular attention can be pointed towards the creation of auxetic materials [181]. Such materials possess a negative Poisson's ratio inducing an interesting behavior of transversal spreading when pulling in a longitudinal direction. Anisotropy here of honeycomb structure can be accentuated to trigger different functions depending on the direction of mechanical stimulation.

Electrospinning technique might be applied to other polymers than PCL to improve cell activity or bring new mechanical properties. Fibers of separated polymers or different fiber morphologies can be combined either by simultaneous or alternative electrospinning. One first polymer will be designed to answer the mechanical support of the structure (polymer well-structured with defined fiber bridges). Besides, the second polymer would be sprayed with a "cell-friendly" polymer in order to fill up the gaps (central zones of the patterned scaffolds). By changing adequately the electrospinning parameters (polymer solution, humidity, and temperature), fibers would deposit in a less organized manner, more homogeneously. Then, alternative two electrospinning modes (organized and non-organized) could create both a solid structure and an attractive niche for cells. Numerical simulation can be as well adapted to other polymers or composite fibers, which will expand the use of the finite element model.

6. References

- [1] S. Nemati, S. Kim, Y. M. Shin, and H. Shin, "Current progress in application of polymeric nanofibers to tissue engineering," *Nano Converg.*, vol. 6, no. 1, p. 36, Dec. 2019, doi: 10.1186/s40580-019-0209-y.
- [2] B. Sun *et al.*, "Advances in three-dimensional nanofibrous macrostructures via electrospinning," *Prog. Polym. Sci.*, vol. 39, no. 5, pp. 862–890, May 2014, doi: 10.1016/j.progpolymsci.2013.06.002.
- [3] "World Health Organization," *World Health Organization*. <https://www.who.int/news-room/fact-sheets/detail/burns>.
- [4] F. Messner, Y. Guo, J. W. Etra, and G. Brandacher, "Emerging technologies in organ preservation, tissue engineering and regenerative medicine: a blessing or curse for transplantation?," *Transpl. Int.*, vol. 32, no. 7, pp. 673–685, Jul. 2019, doi: 10.1111/tri.13432.
- [5] K. Dzobo *et al.*, "Advances in Regenerative Medicine and Tissue Engineering: Innovation and Transformation of Medicine," *Stem Cells Int.*, vol. 2018, pp. 1–24, Jul. 2018, doi: 10.1155/2018/2495848.
- [6] R. Ciccocioppo, A. Cantore, D. Chaimov, and G. Orlando, "Regenerative medicine: the red planet for clinicians," *Intern. Emerg. Med.*, vol. 14, no. 6, pp. 911–921, Sep. 2019, doi: 10.1007/s11739-019-02126-z.
- [7] G. S. Hussey, J. L. Dziki, and S. F. Badylak, "Extracellular matrix-based materials for regenerative medicine," *Nat. Rev. Mater.*, vol. 3, no. 7, pp. 159–173, Jul. 2018, doi: 10.1038/s41578-018-0023-x.
- [8] A. Shamsah, S. Cartmell, S. Richardson, and L. Bosworth, "Mimicking the Annulus Fibrosus Using Electrospun Polyester Blended Scaffolds," *Nanomaterials*, vol. 9, no. 4, p. 537, Apr. 2019, doi: 10.3390/nano9040537.
- [9] "Histology Guide, virtual histology laboratory," *Histology Guide: chapter 3 - Connective Tissue*. <http://www.histologyguide.com/slidebox/03-connective-tissue.html>.
- [10] S. Nemati, S. Kim, Y. M. Shin, and H. Shin, "Current progress in application of polymeric nanofibers to tissue engineering," *Nano Converg.*, vol. 6, no. 1, p. 36, Dec. 2019, doi: 10.1186/s40580-019-0209-y.
- [11] Athira K.S., Pallab Sanpui, and Kaushik Chatterjee, "Fabrication of Poly(Caprolactone) Nanofibers by Electrospinning," *Journal of Polymer and Biopolymer Physics Chemistry*, pp. 62–66, 2014.
- [12] M. Janmohammadi and M. S. Nourbakhsh, "Electrospun polycaprolactone scaffolds for tissue engineering: a review," *Int. J. Polym. Mater. Polym. Biomater.*, vol. 68, no. 9, pp. 527–539, Jun. 2019, doi: 10.1080/00914037.2018.1466139.
- [13] A. Cipitria, A. Skelton, T. R. Dargaville, P. D. Dalton, and D. W. Huttmacher, "Design, fabrication and characterization of PCL electrospun scaffolds—a review," *J. Mater. Chem.*, vol. 21, no. 26, p. 9419, 2011, doi: 10.1039/c0jm04502k.
- [14] E. Tziampazis, J. Kohn, and P. V. Moghe, "PEG-variant biomaterials as selectively adhesive protein templates: model surfaces for controlled cell adhesion and migration," *Biomaterials*, vol. 21, no. 5, pp. 511–520, Mar. 2000, doi: 10.1016/S0142-9612(99)00212-4.
- [15] Z. Ma, Z. Mao, and C. Gao, "Surface modification and property analysis of biomedical polymers used for tissue engineering," *Colloids Surf. B Biointerfaces*, vol. 60, no. 2, pp. 137–157, Nov. 2007, doi: 10.1016/j.colsurfb.2007.06.019.
- [16] P. S. Kandelousi, S. M. Rabiee, M. Jahanshahi, and F. Nasiri, "The effect of bioactive glass nanoparticles on polycaprolactone/chitosan scaffold: Melting enthalpy and cell viability," *J. Bioact. Compat. Polym.*, vol. 34, no. 1, pp. 97–111, Jan. 2019, doi: 10.1177/0883911518819109.
- [17] Y. Lin *et al.*, "In vitro behavior of tendon stem/progenitor cells on bioactive electrospun nanofiber membranes for tendon-bone tissue engineering applications," *Int. J. Nanomedicine*, vol. Volume 14, pp. 5831–5848, Jul. 2019, doi: 10.2147/IJN.S210509.

- [18] Y. Wang *et al.*, "Bone remodeling-inspired dual delivery electrospun nanofibers for promoting bone regeneration," *Nanoscale*, vol. 11, no. 1, pp. 60–71, 2019, doi: 10.1039/C8NR07329E.
- [19] S. Metwally *et al.*, "Single-Step Approach to Tailor Surface Chemistry and Potential on Electrospun PCL Fibers for Tissue Engineering Application," *Adv. Mater. Interfaces*, vol. 6, no. 2, p. 1801211, Jan. 2019, doi: 10.1002/admi.201801211.
- [20] M. M. Kareem, T. Hodgkinson, M. S. Sanchez, M. J. Dalby, and K. E. Tanner, "Hybrid core–shell scaffolds for bone tissue engineering," *Biomed. Mater.*, vol. 14, no. 2, p. 025008, Jan. 2019, doi: 10.1088/1748-605X/aafbf1.
- [21] V. R. Hokmabad, S. Davaran, M. Aghazadeh, E. Alizadeh, R. Salehi, and A. Ramazani, "Effect of incorporating *Elaeagnus angustifolia* extract in PCL-PEG-PCL nanofibers for bone tissue engineering," *Front. Chem. Sci. Eng.*, vol. 13, no. 1, pp. 108–119, Mar. 2019, doi: 10.1007/s11705-018-1742-7.
- [22] V. R. Hokmabad, S. Davaran, M. Aghazadeh, R. Rahbarghazi, R. Salehi, and A. Ramazani, "Fabrication and characterization of novel ethyl cellulose-grafted-poly (ϵ -caprolactone)/alginate nanofibrous/macroporous scaffolds incorporated with nano-hydroxyapatite for bone tissue engineering," *J. Biomater. Appl.*, vol. 33, no. 8, pp. 1128–1144, Mar. 2019, doi: 10.1177/0885328218822641.
- [23] M. Sattary, M. Rafienia, M. Kazemi, H. Salehi, and M. Mahmoudzadeh, "Promoting effect of nano hydroxyapatite and vitamin D3 on the osteogenic differentiation of human adipose-derived stem cells in polycaprolactone/gelatin scaffold for bone tissue engineering," *Mater. Sci. Eng. C*, vol. 97, pp. 141–155, Apr. 2019, doi: 10.1016/j.msec.2018.12.030.
- [24] M. Sattary, M. Rafienia, M. T. Khorasani, and H. Salehi, "The effect of collector type on the physical, chemical, and biological properties of polycaprolactone/gelatin/nano-hydroxyapatite electrospun scaffold," *J. Biomed. Mater. Res. B Appl. Biomater.*, vol. 107, no. 4, pp. 933–950, May 2019, doi: 10.1002/jbm.b.34188.
- [25] Y. Li, C. Liao, and S. C. Tjong, "Synthetic Biodegradable Aliphatic Polyester Nanocomposites Reinforced with Nanohydroxyapatite and/or Graphene Oxide for Bone Tissue Engineering Applications," *Nanomaterials*, vol. 9, no. 4, p. 590, Apr. 2019, doi: 10.3390/nano9040590.
- [26] T. Yu, S. E. Gleeson, C. Y. Li, and M. Marcolongo, "Electrospun poly(ϵ -caprolactone) nanofiber shish kebabs mimic mineralized bony surface features," *J. Biomed. Mater. Res. B Appl. Biomater.*, vol. 107, no. 4, pp. 1141–1149, May 2019, doi: 10.1002/jbm.b.34207.
- [27] M. A. Taghavi, S. M. Rabiee, M. Jahanshahi, and F. Nasiri, "Electrospun Poly- ϵ -Caprolactone (PCL)/Dicalcium Phosphate Dihydrate (DCPD) Composite Scaffold for Tissue Engineering Application," *Mol. Biotechnol.*, vol. 61, no. 5, pp. 345–354, May 2019, doi: 10.1007/s12033-019-00168-4.
- [28] D. Olvera, R. Schipani, B. N. Sathy, and D. J. Kelly, "Electrospinning of highly porous yet mechanically functional microfibrillar scaffolds at the human scale for ligament and tendon tissue engineering," *Biomed. Mater.*, vol. 14, no. 3, p. 035016, Apr. 2019, doi: 10.1088/1748-605X/ab0de1.
- [29] Q. Zhu, Z. Ma, H. Li, H. Wang, and Y. He, "Enhancement of rotator cuff tendon–bone healing using combined aligned electrospun fibrous membranes and kartogenin," *RSC Adv.*, vol. 9, no. 27, pp. 15582–15592, 2019, doi: 10.1039/C8RA09849B.
- [30] M. S. Carvalho *et al.*, "Co-culture cell-derived extracellular matrix loaded electrospun microfibrillar scaffolds for bone tissue engineering," *Mater. Sci. Eng. C*, vol. 99, pp. 479–490, Jun. 2019, doi: 10.1016/j.msec.2019.01.127.
- [31] Y. Zhang *et al.*, "Electrospinning Nanofiber-Reinforced Aerogels for the Treatment of Bone Defects," *Adv. Wound Care*, p. wound.2018.0879, Jun. 2019, doi: 10.1089/wound.2018.0879.
- [32] S. Shafiei *et al.*, "Egg shell-derived calcium phosphate/carbon dot nanofibrous scaffolds for bone tissue engineering: Fabrication and characterization," *Mater. Sci. Eng. C*, vol. 100, pp. 564–575, Jul. 2019, doi: 10.1016/j.msec.2019.03.003.

- [33] A. D. Dalgic, D. Atila, A. Karatas, A. Tezcaner, and D. Keskin, "Diatom shell incorporated PHBV/PCL-pullulan co-electrospun scaffold for bone tissue engineering," *Mater. Sci. Eng. C*, vol. 100, pp. 735–746, Jul. 2019, doi: 10.1016/j.msec.2019.03.046.
- [34] S. Gniesmer *et al.*, "In vivo analysis of vascularization and biocompatibility of electrospun polycaprolactone fibre mats in the rat femur chamber," *J. Tissue Eng. Regen. Med.*, p. term.2868, May 2019, doi: 10.1002/term.2868.
- [35] A. Rahmani, S. Hashemi-Najafabadi, M. B. Eslaminejad, F. Bagheri, and F. A. Sayahpour, "The effect of modified electrospun PCL-nHA-nZnO scaffolds on osteogenesis and angiogenesis," *J. Biomed. Mater. Res. A*, vol. 107, no. 9, pp. 2040–2052, Sep. 2019, doi: 10.1002/jbm.a.36717.
- [36] B. Feng *et al.*, "Bioresorbable electrospun gelatin/polycaprolactone nanofibrous membrane as a barrier to prevent cardiac postoperative adhesion," *Acta Biomater.*, vol. 83, pp. 211–220, Jan. 2019, doi: 10.1016/j.actbio.2018.10.022.
- [37] M. O. Aydogdu *et al.*, "Production of the biomimetic small diameter blood vessels for cardiovascular tissue engineering," *Int. J. Polym. Mater. Polym. Biomater.*, vol. 68, no. 5, pp. 243–255, Mar. 2019, doi: 10.1080/00914037.2018.1443930.
- [38] T. B. Wissing *et al.*, "Macrophage-Driven Biomaterial Degradation Depends on Scaffold Microarchitecture," *Front. Bioeng. Biotechnol.*, vol. 7, p. 87, Apr. 2019, doi: 10.3389/fbioe.2019.00087.
- [39] L. Vogt, L. R. Rivera, L. Liverani, A. Piegat, M. El Fray, and A. R. Boccaccini, "Poly(ϵ -caprolactone)/poly(glycerol sebacate) electrospun scaffolds for cardiac tissue engineering using benign solvents," *Mater. Sci. Eng. C*, vol. 103, p. 109712, Oct. 2019, doi: 10.1016/j.msec.2019.04.091.
- [40] Nadia Rahimi Tanha and Mahdi Nouri, "Core-shell Nanofibers of Silk Fibroin/Polycaprolactone-Clindamycin: Study on Nanofibers Structure and Controlled Release Behavior," *Polym. Sci. Ser. A*, vol. 61, no. 1, pp. 85–95, Jan. 2019, doi: 10.1134/S0965545X19010085.
- [41] Ş. M. Eskitoros-Togay, Y. E. Bulbul, S. Tort, F. Demirtaş Korkmaz, F. Acartürk, and N. Dilsiz, "Fabrication of doxycycline-loaded electrospun PCL/PEO membranes for a potential drug delivery system," *Int. J. Pharm.*, vol. 565, pp. 83–94, Jun. 2019, doi: 10.1016/j.ijpharm.2019.04.073.
- [42] A. Fuchs *et al.*, "A new multilayered membrane for tissue engineering of oral hard- and soft tissue by means of melt electrospinning writing and film casting – An in vitro study," *J. Cranio-Maxillofac. Surg.*, vol. 47, no. 4, pp. 695–703, Apr. 2019, doi: 10.1016/j.jcms.2019.01.043.
- [43] F. Sharif *et al.*, "Bioresorbable antibacterial PCL-PLA-nHA composite membranes for oral and maxillofacial defects," *Polym. Compos.*, vol. 40, no. 4, pp. 1564–1575, Apr. 2019, doi: 10.1002/pc.24899.
- [44] Y. Deng *et al.*, "Bioinspired and osteopromotive polydopamine nanoparticle-incorporated fibrous membranes for robust bone regeneration," *NPG Asia Mater.*, vol. 11, no. 1, p. 39, Dec. 2019, doi: 10.1038/s41427-019-0139-5.
- [45] F. S. Hosseini *et al.*, "Efficient osteogenic differentiation of the dental pulp stem cells on β -glycerophosphate loaded polycaprolactone/polyethylene oxide blend nanofibers," *J. Cell. Physiol.*, vol. 234, no. 8, pp. 13951–13958, Aug. 2019, doi: 10.1002/jcp.28078.
- [46] D. Browe and J. Freeman, "Optimizing C2C12 myoblast differentiation using polycaprolactone-poly pyrrole copolymer scaffolds: Optimization of C2C12 myoblast differentiation using PPy-PCL copolymer," *J. Biomed. Mater. Res. A*, vol. 107, no. 1, pp. 220–231, Jan. 2019, doi: 10.1002/jbm.a.36556.
- [47] D. Dippold *et al.*, "Investigation of the batch-to-batch inconsistencies of Collagen in PCL-Collagen nanofibers," *Mater. Sci. Eng. C*, vol. 95, pp. 217–225, Feb. 2019, doi: 10.1016/j.msec.2018.10.057.
- [48] D. Sooriyaarachchi, H. J. Minière, S. Maharubin, and G. Z. Tan, "Hybrid Additive Microfabrication Scaffold Incorporated with Highly Aligned Nanofibers for Musculoskeletal Tissues," *Tissue Eng. Regen. Med.*, vol. 16, no. 1, pp. 29–38, Feb. 2019, doi: 10.1007/s13770-018-0169-z.

- [49] A. Sadeghi, F. Moztaizadeh, and J. Aghazadeh Mohandesi, "Investigating the effect of chitosan on hydrophilicity and bioactivity of conductive electrospun composite scaffold for neural tissue engineering," *Int. J. Biol. Macromol.*, vol. 121, pp. 625–632, Jan. 2019, doi: 10.1016/j.ijbiomac.2018.10.022.
- [50] V. P. Baklaushev *et al.*, "Tissue Engineered Neural Constructs Composed of Neural Precursor Cells, Recombinant Spidroin and PRP for Neural Tissue Regeneration," *Sci. Rep.*, vol. 9, no. 1, p. 3161, Dec. 2019, doi: 10.1038/s41598-019-39341-9.
- [51] E. Altun *et al.*, "Bioinspired scaffold induced regeneration of neural tissue," *Eur. Polym. J.*, vol. 114, pp. 98–108, May 2019, doi: 10.1016/j.eurpolymj.2019.02.008.
- [52] F. F. F. Garrudo *et al.*, "Polyaniline-polycaprolactone blended nanofibers for neural cell culture," *Eur. Polym. J.*, vol. 117, pp. 28–37, Aug. 2019, doi: 10.1016/j.eurpolymj.2019.04.048.
- [53] S. Nekouian, M. Sojoodi, and S. Nadri, "Fabrication of conductive fibrous scaffold for photoreceptor differentiation of mesenchymal stem cell," *J. Cell. Physiol.*, vol. 234, no. 9, pp. 15800–15808, Sep. 2019, doi: 10.1002/jcp.28238.
- [54] K. Jansen *et al.*, "Fabrication of Kidney Proximal Tubule Grafts Using Biofunctionalized Electrospun Polymer Scaffolds," *Macromol. Biosci.*, vol. 19, no. 2, p. 1800412, Feb. 2019, doi: 10.1002/mabi.201800412.
- [55] R. Sobreiro-Almeida, D. R. Fonseca, and N. M. Neves, "Extracellular matrix electrospun membranes for mimicking natural renal filtration barriers," *Mater. Sci. Eng. C*, vol. 103, p. 109866, Oct. 2019, doi: 10.1016/j.msec.2019.109866.
- [56] Z. Pedram Rad, J. Mokhtari, and M. Abbasi, "Preparation and characterization of Calendula officinalis-loaded PCL/gum arabic nanocomposite scaffolds for wound healing applications," *Iran. Polym. J.*, vol. 28, no. 1, pp. 51–63, Jan. 2019, doi: 10.1007/s13726-018-0674-x.
- [57] Z. Pedram Rad, J. Mokhtari, and M. Abbasi, "Calendula officinalis extract/PCL/Zein/Gum arabic nanofibrous bio-composite scaffolds via suspension, two-nozzle and multilayer electrospinning for skin tissue engineering," *Int. J. Biol. Macromol.*, vol. 135, pp. 530–543, Aug. 2019, doi: 10.1016/j.ijbiomac.2019.05.204.
- [58] E. Zahedi, A. Esmaeili, N. Eslahi, M. A. Shokrgozar, and A. Simchi, "Fabrication and Characterization of Core-Shell Electrospun Fibrous Mats Containing Medicinal Herbs for Wound Healing and Skin Tissue Engineering," *Mar. Drugs*, vol. 17, no. 1, p. 27, Jan. 2019, doi: 10.3390/md17010027.
- [59] M. Adeli-Sardou, M. M. Yaghoobi, M. Torkzadeh-Mahani, and M. Dodel, "Controlled release of lawsone from polycaprolactone/gelatin electrospun nano fibers for skin tissue regeneration," *Int. J. Biol. Macromol.*, vol. 124, pp. 478–491, Mar. 2019, doi: 10.1016/j.ijbiomac.2018.11.237.
- [60] M. J. Mirzaei-parsa, H. Ghanbari, B. Alipoor, A. Tavakoli, M. R. H. Najafabadi, and R. Faridi-Majidi, "Nanofiber-acellular dermal matrix as a bilayer scaffold containing mesenchymal stem cell for healing of full-thickness skin wounds," *Cell Tissue Res.*, vol. 375, no. 3, pp. 709–721, Mar. 2019, doi: 10.1007/s00441-018-2927-6.
- [61] W. Xie, X. Fu, Y. D. Wang, G. Wang, and X. Chen, "Fabrication of bioactive glass particles composite porous fibers by combination of electrospinning and phase separation," *Mater. Lett.*, vol. 248, pp. 185–188, Aug. 2019, doi: 10.1016/j.matlet.2019.03.143.
- [62] X. Zhang, L. Wang, L. Han, Y. Wang, B. Dai, and X. Song, "Anchoring resveratrol on surface of electrospun star-shaped PCL-COOH/PLLA fibers," *Int. J. Polym. Mater. Polym. Biomater.*, pp. 1–9, Jun. 2019, doi: 10.1080/00914037.2019.1616199.
- [63] I. Cruz-Maya, V. Guarino, A. Almaguer-Flores, M. A. Alvarez-Perez, A. Varesano, and C. Vineis, "Highly polydisperse keratin rich nanofibers: Scaffold design and *in vitro* characterization," *J. Biomed. Mater. Res. A*, p. jbm.a.36699, Apr. 2019, doi: 10.1002/jbm.a.36699.
- [64] S. Gomes, D. Querido, J. L. Ferreira, J. P. Borges, C. Henriques, and J. C. Silva, "Using water to control electrospun Polycaprolactone fibre morphology for soft tissue engineering," *J. Polym. Res.*, vol. 26, no. 9, p. 222, Sep. 2019, doi: 10.1007/s10965-019-1890-6.
- [65] S. J. Lee *et al.*, "Vascular endothelial growth factor immobilized on mussel-inspired three-dimensional bilayered scaffold for artificial vascular graft application: In vitro and in vivo

- evaluations," *J. Colloid Interface Sci.*, vol. 537, pp. 333–344, Mar. 2019, doi: 10.1016/j.jcis.2018.11.039.
- [66] R. Johnson, Y. Ding, N. Nagiah, E. Monnet, and W. Tan, "Coaxially-structured fibres with tailored material properties for vascular graft implant," *Mater. Sci. Eng. C*, vol. 97, pp. 1–11, Apr. 2019, doi: 10.1016/j.msec.2018.11.036.
- [67] D. C. Ardila, E. Tamimi, T. Doetschman, W. R. Wagner, and J. P. Vande Geest, "Modulating smooth muscle cell response by the release of TGF β 2 from tubular scaffolds for vascular tissue engineering," *J. Controlled Release*, vol. 299, pp. 44–52, Apr. 2019, doi: 10.1016/j.jconrel.2019.02.024.
- [68] J. Joy *et al.*, "Electrospun microporous gelatin–polycaprolactone blend tubular scaffold as a potential vascular biomaterial," *Polym. Int.*, vol. 68, no. 7, pp. 1367–1377, Jul. 2019, doi: 10.1002/pi.5827.
- [69] E. E. van Haften *et al.*, "The degradation and performance of electrospun supramolecular vascular scaffolds examined upon in vitro enzymatic exposure," *Acta Biomater.*, vol. 92, pp. 48–59, Jul. 2019, doi: 10.1016/j.actbio.2019.05.037.
- [70] R. Tejada-Alejandre, J. A. Lammel-Lindemann, H. Lara-Padilla, D. Dean, and C. A. Rodriguez, "Influence of Electrical Field Collector Positioning and Motion Scheme on Electrospun Bifurcated Vascular Graft Membranes," *Materials*, vol. 12, no. 13, p. 2123, Jul. 2019, doi: 10.3390/ma12132123.
- [71] X. Jin *et al.*, "Preparation of Small-Diameter Tissue-Engineered Vascular Grafts Electrospun from Heparin End-Capped PCL and Evaluation in a Rabbit Carotid Artery Replacement Model," *Macromol. Biosci.*, vol. 19, no. 8, p. 1900114, Aug. 2019, doi: 10.1002/mabi.201900114.
- [72] M. A. Alfaro De Prá, R. M. Ribeiro-do-Valle, M. Maraschin, and B. Veleirinho, "Effect of collector design on the morphological properties of polycaprolactone electrospun fibers," *Mater. Lett.*, vol. 193, pp. 154–157, Apr. 2017, doi: 10.1016/j.matlet.2017.01.102.
- [73] X. Dong *et al.*, "An anisotropic three-dimensional electrospun micro/nanofibrous hybrid PLA/PCL scaffold," *RSC Adv.*, vol. 9, no. 17, pp. 9838–9844, 2019, doi: 10.1039/C9RA00846B.
- [74] Formhals, A., "Process and Apparatus for Preparing Artificial Threads," 1975504.
- [75] Jayesh Doshi and Darrell H. Reneker, "Electrospinning Process and Applications of Electrospun Fibers," *Journal of Electrostatics*, pp. 151–160, 1995.
- [76] P. Ke, X.-N. Jiao, X.-H. Ge, W.-M. Xiao, and B. Yu, "From macro to micro: structural biomimetic materials by electrospinning," *RSC Adv.*, vol. 4, no. 75, pp. 39704–39724, 2014, doi: 10.1039/C4RA05098C.
- [77] B. S. Gupta and A. K. Moghe, "Nanofiber structures for medical biotextiles," in *Biotextiles as Medical Implants*, Elsevier, 2013, pp. 48–90.
- [78] C. Wang, Y. Wang, and T. Hashimoto, "Impact of Entanglement Density on Solution Electrospinning: A Phenomenological Model for Fiber Diameter," *Macromolecules*, vol. 49, no. 20, pp. 7985–7996, Oct. 2016, doi: 10.1021/acs.macromol.6b00519.
- [79] J. H. Yu, S. V. Fridrikh, and G. C. Rutledge, "The role of elasticity in the formation of electrospun fibers," *Polymer*, vol. 47, no. 13, pp. 4789–4797, Jun. 2006, doi: 10.1016/j.polymer.2006.04.050.
- [80] S. L. Shenoy, W. D. Bates, H. L. Frisch, and G. E. Wnek, "Role of chain entanglements on fiber formation during electrospinning of polymer solutions: good solvent, non-specific polymer–polymer interaction limit," *Polymer*, vol. 46, no. 10, pp. 3372–3384, Apr. 2005, doi: 10.1016/j.polymer.2005.03.011.
- [81] H. Fong, I. Chun, and D. H. Reneker, "Beaded nanofibers formed during electrospinning," *Polymer*, vol. 40, no. 16, pp. 4585–4592, Jul. 1999, doi: 10.1016/S0032-3861(99)00068-3.
- [82] A. Haider, S. Haider, and I.-K. Kang, "A comprehensive review summarizing the effect of electrospinning parameters and potential applications of nanofibers in biomedical and biotechnology," *Arab. J. Chem.*, vol. 11, no. 8, pp. 1165–1188, Dec. 2018, doi: 10.1016/j.arabjc.2015.11.015.

- [83] X. Zong, K. Kim, D. Fang, S. Ran, B. S. Hsiao, and B. Chu, "Structure and process relationship of electrospun bioabsorbable nanofiber membranes," *Polymer*, vol. 43, no. 16, pp. 4403–4412, Jul. 2002, doi: 10.1016/S0032-3861(02)00275-6.
- [84] J. S. Choi *et al.*, "Effect of organosoluble salts on the nanofibrous structure of electrospun poly(3-hydroxybutyrate-co-3-hydroxyvalerate)," *Int. J. Biol. Macromol.*, vol. 34, no. 4, pp. 249–256, Aug. 2004, doi: 10.1016/j.ijbiomac.2004.06.001.
- [85] S. Megelski, J. S. Stephens, D. B. Chase, and J. F. Rabolt, "Micro- and Nanostructured Surface Morphology on Electrospun Polymer Fibers," *Macromolecules*, vol. 35, no. 22, pp. 8456–8466, Oct. 2002, doi: 10.1021/ma020444a.
- [86] S. Koombhongse, W. Liu, and D. H. Reneker, "Flat polymer ribbons and other shapes by electrospinning," *J. Polym. Sci. Part B Polym. Phys.*, vol. 39, no. 21, pp. 2598–2606, Nov. 2001, doi: 10.1002/polb.10015.
- [87] A. K. Haghi and M. Akbari, "Trends in electrospinning of natural nanofibers," *Phys. Status Solidi A*, vol. 204, no. 6, pp. 1830–1834, Jun. 2007, doi: 10.1002/pssa.200675301.
- [88] E. Boland D., "Electrospinning collagen and elastin: preliminary vascular tissue engineering," *Front. Biosci.*, vol. 9, no. 1–3, p. 1422, 2004, doi: 10.2741/1313.
- [89] "Electrospin Tech website," *Electrospin Tech*. <http://electrospintech.com/knowledge.html>.
- [90] X. Yuan, Y. Zhang, C. Dong, and J. Sheng, "Morphology of ultrafine polysulfone fibers prepared by electrospinning," *Polym. Int.*, vol. 53, no. 11, pp. 1704–1710, Nov. 2004, doi: 10.1002/pi.1538.
- [91] S. Zargham, S. Bazgir, A. Tavakoli, A. S. Rashidi, and R. Damerchely, "The Effect of Flow Rate on Morphology and Deposition Area of Electrospun Nylon 6 Nanofiber," *J. Eng. Fibers Fabr.*, vol. 7, no. 4, p. 155892501200700, Dec. 2012, doi: 10.1177/155892501200700414.
- [92] J. Pelipenko, J. Kristl, B. Janković, S. Baumgartner, and P. Kocbek, "The impact of relative humidity during electrospinning on the morphology and mechanical properties of nanofibers," *Int. J. Pharm.*, vol. 456, no. 1, pp. 125–134, Nov. 2013, doi: 10.1016/j.ijpharm.2013.07.078.
- [93] J.-Y. Park and I.-H. Lee, "Relative Humidity Effect on the Preparation of Porous Electrospun Polystyrene Fibers," *J. Nanosci. Nanotechnol.*, vol. 10, no. 5, pp. 3473–3477, May 2010, doi: 10.1166/jnn.2010.2349.
- [94] H.-S. Bae, A. Haider, K. M. K. Selim, D.-Y. Kang, E.-J. Kim, and I.-K. Kang, "Fabrication of highly porous PMMA electrospun fibers and their application in the removal of phenol and iodine," *J. Polym. Res.*, vol. 20, no. 7, Jul. 2013, doi: 10.1007/s10965-013-0158-9.
- [95] C. L. Casper, J. S. Stephens, N. G. Tassi, D. B. Chase, and J. F. Rabolt, "Controlling Surface Morphology of Electrospun Polystyrene Fibers: Effect of Humidity and Molecular Weight in the Electrospinning Process," *Macromolecules*, vol. 37, no. 2, pp. 573–578, Jan. 2004, doi: 10.1021/ma0351975.
- [96] C. Mit-uppatham, M. Nithitanakul, and P. Supaphol, "Ultrafine Electrospun Polyamide-6 Fibers: Effect of Solution Conditions on Morphology and Average Fiber Diameter," *Macromol. Chem. Phys.*, vol. 205, no. 17, pp. 2327–2338, Nov. 2004, doi: 10.1002/macp.200400225.
- [97] S. De Vrieze, T. Van Camp, A. Nelvig, B. Hagström, P. Westbroek, and K. De Clerck, "The effect of temperature and humidity on electrospinning," *J. Mater. Sci.*, vol. 44, no. 5, pp. 1357–1362, Mar. 2009, doi: 10.1007/s10853-008-3010-6.
- [98] T. J. Sill and H. A. von Recum, "Electrospinning: Applications in drug delivery and tissue engineering," *Biomaterials*, vol. 29, no. 13, pp. 1989–2006, May 2008, doi: 10.1016/j.biomaterials.2008.01.011.
- [99] G. Yan *et al.*, "Self-Assembly of Electrospun Polymer Nanofibers: A General Phenomenon Generating Honeycomb-Patterned Nanofibrous Structures," *Langmuir*, vol. 27, no. 8, pp. 4285–4289, Apr. 2011, doi: 10.1021/la1047936.
- [100] T. Yao, H. Chen, P. Samal, S. Giselbrecht, M. B. Baker, and L. Moroni, "Self-assembly of electrospun nanofibers into gradient honeycomb structures," *Mater. Des.*, vol. 168, p. 107614, Apr. 2019, doi: 10.1016/j.matdes.2019.107614.

- [101] B. Sundaray, V. Subramanian, T. S. Natarajan, R.-Z. Xiang, C.-C. Chang, and W.-S. Fann, "Electrospinning of continuous aligned polymer fibers," *Appl. Phys. Lett.*, vol. 84, no. 7, pp. 1222–1224, Feb. 2004, doi: 10.1063/1.1647685.
- [102] H. Pan, L. Li, L. Hu, and X. Cui, "Continuous aligned polymer fibers produced by a modified electrospinning method," *Polymer*, vol. 47, no. 14, pp. 4901–4904, Jun. 2006, doi: 10.1016/j.polymer.2006.05.012.
- [103] Z.-M. Huang, Y.-Z. Zhang, M. Kotaki, and S. Ramakrishna, "A review on polymer nanofibers by electrospinning and their applications in nanocomposites," *Compos. Sci. Technol.*, vol. 63, no. 15, pp. 2223–2253, Nov. 2003, doi: 10.1016/S0266-3538(03)00178-7.
- [104] P. Katta, M. Alessandro, R. D. Ramsier, and G. G. Chase, "Continuous Electrospinning of Aligned Polymer Nanofibers onto a Wire Drum Collector," *Nano Lett.*, vol. 4, no. 11, pp. 2215–2218, Nov. 2004, doi: 10.1021/nl0486158.
- [105] C. A. Bashur, L. A. Dahlgren, and A. S. Goldstein, "Effect of fiber diameter and orientation on fibroblast morphology and proliferation on electrospun poly(d,l-lactic-co-glycolic acid) meshes," *Biomaterials*, vol. 27, no. 33, pp. 5681–5688, Nov. 2006, doi: 10.1016/j.biomaterials.2006.07.005.
- [106] S. Zhong, W. E. Teo, X. Zhu, R. W. Beuerman, S. Ramakrishna, and L. Y. L. Yung, "An aligned nanofibrous collagen scaffold by electrospinning and its effects on in vitro fibroblast culture," *J. Biomed. Mater. Res. A*, vol. 79A, no. 3, pp. 456–463, Dec. 2006, doi: 10.1002/jbm.a.30870.
- [107] V. Beachley and X. Wen, "Effect of electrospinning parameters on the nanofiber diameter and length," *Mater. Sci. Eng. C*, vol. 29, no. 3, pp. 663–668, Apr. 2009, doi: 10.1016/j.msec.2008.10.037.
- [108] M. Pokorny, K. Niedoba, and V. Velebny, "Transversal electrostatic strength of patterned collector affecting alignment of electrospun nanofibers," *Appl. Phys. Lett.*, vol. 96, no. 19, p. 193111, May 2010, doi: 10.1063/1.3430507.
- [109] D. Li, Y. Wang, and Y. Xia, "Electrospinning of Polymeric and Ceramic Nanofibers as Uniaxially Aligned Arrays," *Nano Lett.*, vol. 3, no. 8, pp. 1167–1171, Aug. 2003, doi: 10.1021/nl0344256.
- [110] V. Beachley and X. Wen, "Effect of electrospinning parameters on the nanofiber diameter and length," *Mater. Sci. Eng. C*, vol. 29, no. 3, pp. 663–668, Apr. 2009, doi: 10.1016/j.msec.2008.10.037.
- [111] Z. Liu *et al.*, "Control of structure and morphology of highly aligned PLLA ultrafine fibers via linear-jet electrospinning," *Polymer*, vol. 54, no. 21, pp. 6045–6051, Oct. 2013, doi: 10.1016/j.polymer.2013.08.051.
- [112] F. Dabirian, S. A. Hosseini Ravandi, and A. R. Pishevar, "The effects of operating parameters on the fabrication of polyacrylonitrile nanofibers in electro-centrifuge spinning," *Fibers Polym.*, vol. 14, no. 9, pp. 1497–1504, Sep. 2013, doi: 10.1007/s12221-013-1497-1.
- [113] C. Vaquette and J. J. Cooper-White, "Increasing electrospun scaffold pore size with tailored collectors for improved cell penetration," *Acta Biomater.*, vol. 7, no. 6, pp. 2544–2557, Jun. 2011, doi: 10.1016/j.actbio.2011.02.036.
- [114] K. Titov and J.-C. Tan, "Facile patterning of electrospun polymer fibers enabled by electrostatic lensing interactions," *APL Mater.*, vol. 4, no. 8, p. 086107, Aug. 2016, doi: 10.1063/1.4960982.
- [115] S. Zhao, Q. Zhou, Y.-Z. Long, G.-H. Sun, and Y. Zhang, "Nanofibrous patterns by direct electrospinning of nanofibers onto topographically structured non-conductive substrates," *Nanoscale*, vol. 5, no. 11, p. 4993, 2013, doi: 10.1039/c3nr00676j.
- [116] S. L. Liu, G. H. Sun, Y. Y. Huang, B. Sun, H. D. Zhang, and Y. Z. Long, "Fabrication and Formation Mechanism of Electrospun Spatially Defined Fibrous Patterning Structures on Conductive and Insulating Substrates," *Key Eng. Mater.*, vol. 609–610, pp. 842–848, Apr. 2014, doi: 10.4028/www.scientific.net/KEM.609-610.842.
- [117] Y. Wu, Z. Dong, S. Wilson, and R. L. Clark, "Template-assisted assembly of electrospun fibers," *Polymer*, vol. 51, no. 14, pp. 3244–3248, Jun. 2010, doi: 10.1016/j.polymer.2010.04.039.

- [118] Y. Wang, H. Li, G. Wang, T. Yin, B. Wang, and Q. Yu, "Electrospinning of Polymer Nanofibers with Ordered Patterns and Architectures," *J. Nanosci. Nanotechnol.*, vol. 10, no. 3, pp. 1699–1706, Mar. 2010, doi: 10.1166/jnn.2010.2149.
- [119] Í. Ortega, A. J. Ryan, P. Deshpande, S. MacNeil, and F. Claeyssens, "Combined microfabrication and electrospinning to produce 3-D architectures for corneal repair," *Acta Biomater.*, vol. 9, no. 3, pp. 5511–5520, Mar. 2013, doi: 10.1016/j.actbio.2012.10.039.
- [120] Y. Qiao *et al.*, "An ordered electrospun polycaprolactone–collagen–silk fibroin scaffold for hepatocyte culture," *J. Mater. Sci.*, vol. 53, no. 3, pp. 1623–1633, Feb. 2018, doi: 10.1007/s10853-017-1670-9.
- [121] K. Zhang, X. Wang, D. Jing, Y. Yang, and M. Zhu, "Bionic electrospun ultrafine fibrous poly(L-lactic acid) scaffolds with a multi-scale structure," *Biomed. Mater.*, vol. 4, no. 3, p. 035004, Jun. 2009, doi: 10.1088/1748-6041/4/3/035004.
- [122] D. Zhang and J. Chang, "Patterning of Electrospun Fibers Using Electroconductive Templates," *Adv. Mater.*, vol. 19, no. 21, pp. 3664–3667, Nov. 2007, doi: 10.1002/adma.200700896.
- [123] Y. Liu, R. Liu, X. Wang, Shumin Guo, and G. Zheng, "Electrospun Three-Dimensional Nanofibrous Structure via Probe Arrays Inducing," *Micromachines*, p. 427, Aug. 24, 2018.
- [124] D. Zhang and J. Chang, "Electrospinning of Three-Dimensional Nanofibrous Tubes with Controllable Architectures," *Nanoletters*, pp. 3283–3287, 2008.
- [125] S. Nedjari, G. Schlatter, and A. Hébraud, "Thick electrospun honeycomb scaffolds with controlled pore size," *Mater. Lett.*, vol. 142, pp. 180–183, Mar. 2015, doi: 10.1016/j.matlet.2014.11.118.
- [126] C. R. Wittmer, A. Hébraud, S. Nedjari, and G. Schlatter, "Well-organized 3D nanofibrous composite constructs using cooperative effects between electrospinning and electro spraying," *Polymer*, vol. 55, no. 22, pp. 5781–5787, Oct. 2014, doi: 10.1016/j.polymer.2014.08.044.
- [127] S. Chew, Y. Wen, Y. Dzenis, and K. Leong, "The Role of Electrospinning in the Emerging Field of Nanomedicine," *Curr. Pharm. Des.*, vol. 12, no. 36, pp. 4751–4770, Dec. 2006, doi: 10.2174/138161206779026326.
- [128] M. Ottenio, D. Tran, A. Ní Annaidh, M. D. Gilchrist, and K. Bruyère, "Strain rate and anisotropy effects on the tensile failure characteristics of human skin," *J. Mech. Behav. Biomed. Mater.*, vol. 41, pp. 241–250, Jan. 2015, doi: 10.1016/j.jmbbm.2014.10.006.
- [129] A. Ní Annaidh, K. Bruyère, M. Destrade, M. D. Gilchrist, and M. Otténio, "Characterization of the anisotropic mechanical properties of excised human skin," *J. Mech. Behav. Biomed. Mater.*, vol. 5, no. 1, pp. 139–148, Jan. 2012, doi: 10.1016/j.jmbbm.2011.08.016.
- [130] H. Joodaki and M. B. Panzer, "Skin mechanical properties and modeling: A review," *Proc. Inst. Mech. Eng. [H]*, vol. 232, no. 4, pp. 323–343, Apr. 2018, doi: 10.1177/0954411918759801.
- [131] C. T. McKee, J. A. Last, P. Russell, and C. J. Murphy, "Indentation Versus Tensile Measurements of Young's Modulus for Soft Biological Tissues," *Tissue Eng. Part B Rev.*, vol. 17, no. 3, pp. 155–164, Jun. 2011, doi: 10.1089/ten.teb.2010.0520.
- [132] A. Trotta and A. Ní Annaidh, "Mechanical characterisation of human and porcine scalp tissue at dynamic strain rates," *J. Mech. Behav. Biomed. Mater.*, vol. 100, p. 103381, Dec. 2019, doi: 10.1016/j.jmbbm.2019.103381.
- [133] K. Mubyana, R. A. Koppes, K. L. Lee, J. A. Cooper, and D. T. Corr, "The influence of specimen thickness and alignment on the material and failure properties of electrospun polycaprolactone nanofiber mats," *J. Biomed. Mater. Res. A*, vol. 104, no. 11, pp. 2794–2800, Nov. 2016, doi: 10.1002/jbm.a.35821.
- [134] H. Yuan, H. Shi, X. Qiu, and Y. Chen, "Mechanical property and biological performance of electrospun silk fibroin-polycaprolactone scaffolds with aligned fibers," *J. Biomater. Sci. Polym. Ed.*, vol. 27, no. 3, pp. 263–275, Feb. 2016, doi: 10.1080/09205063.2015.1120475.
- [135] S. R. Baker, S. Banerjee, K. Bonin, and M. Guthold, "Determining the mechanical properties of electrospun poly- ϵ -caprolactone (PCL) nanofibers using AFM and a novel fiber anchoring technique," *Mater. Sci. Eng. C*, vol. 59, pp. 203–212, Feb. 2016, doi: 10.1016/j.msec.2015.09.102.

- [136] Y. Kang, P. Chen, X. Shi, G. Zhang, and C. Wang, "Multilevel structural stereocomplex polylactic acid/collagen membranes by pattern electrospinning for tissue engineering," *Polymer*, vol. 156, pp. 250–260, Nov. 2018, doi: 10.1016/j.polymer.2018.10.009.
- [137] N. M. Neves, R. Campos, A. Pedro, J. Cunha, F. Macedo, and R. L. Reis, "Patterning of polymer nanofiber meshes by electrospinning for biomedical applications," *Int. J. Nanomedicine*, p. 16.
- [138] C. Vaquette and J. J. Cooper-White, "Increasing electrospun scaffold pore size with tailored collectors for improved cell penetration," *Acta Biomater.*, vol. 7, no. 6, pp. 2544–2557, Jun. 2011, doi: 10.1016/j.actbio.2011.02.036.
- [139] Y. Kang, P. Chen, X. Shi, G. Zhang, and C. Wang, "Multilevel structural stereocomplex polylactic acid/collagen membranes by pattern electrospinning for tissue engineering," *Polymer*, vol. 156, pp. 250–260, Nov. 2018, doi: 10.1016/j.polymer.2018.10.009.
- [140] Y. Wang *et al.*, "Electrospun nanofiber meshes with tailored architectures and patterns as potential tissue-engineering scaffolds," *Biofabrication*, vol. 1, 2009, doi: 10.1088/1758-5082/1/1/015001.
- [141] D. Yan *et al.*, "Plasma treatment of random and aligned electrospun PCL nanofibers," *J. Med. Biol. Eng.*, vol. 33, no. 2, pp. 171–178, 2013, doi: 10.5405/jmbe.1072.
- [142] R. C. Thomson, M. J. Yaszemski, J. M. Powers, and A. G. Mikos, "Fabrication of biodegradable polymer scaffolds to engineer trabecular bone," *J. Biomater. Sci. Polym. Ed.*, vol. 7, no. 1, pp. 23–38, Jan. 1996, doi: 10.1163/156856295X00805.
- [143] H. Sawalha, K. Schroën, and R. Boom, "Mechanical properties and porosity of polylactide for biomedical applications," *J. Appl. Polym. Sci.*, vol. 107, no. 1, pp. 82–93, Jan. 2008, doi: 10.1002/app.27116.
- [144] A. Lancuški, S. Fort, and F. Bossard, "Electrospun Azido-PCL Nanofibers for Enhanced Surface Functionalization by Click Chemistry," *ACS Appl. Mater. Interfaces*, vol. 4, no. 12, pp. 6499–6504, Dec. 2012, doi: 10.1021/am301458y.
- [145] A. Lancuški, F. Bossard, and S. Fort, "Carbohydrate-Decorated PCL Fibers for Specific Protein Adhesion," *Biomacromolecules*, vol. 14, no. 6, pp. 1877–1884, Jun. 2013, doi: 10.1021/bm400263d.
- [146] C. Vaquette and J. J. Cooper-White, "Increasing electrospun scaffold pore size with tailored collectors for improved cell penetration," *Acta Biomater.*, vol. 7, no. 6, pp. 2544–2557, Jun. 2011, doi: 10.1016/j.actbio.2011.02.036.
- [147] H. Yu *et al.*, "Novel porous three-dimensional nanofibrous scaffolds for accelerating wound healing," *Chem. Eng. J.*, vol. 369, pp. 253–262, Aug. 2019, doi: 10.1016/j.cej.2019.03.091.
- [148] J. Hodge and C. Quint, "The improvement of cell infiltration in an electrospun scaffold with multiple synthetic biodegradable polymers using sacrificial PEO microparticles," *J. Biomed. Mater. Res. A*, vol. 107, no. 9, pp. 1954–1964, Sep. 2019, doi: 10.1002/jbm.a.36706.
- [149] Y. Liu *et al.*, "Comparison of polyglycolic acid, polycaprolactone, and collagen as scaffolds for the production of tissue engineered intestine," *J. Biomed. Mater. Res. B Appl. Biomater.*, vol. 107, no. 3, pp. 750–760, Apr. 2019, doi: 10.1002/jbm.b.34169.
- [150] C. Liu *et al.*, "Controllable Aligned Nanofiber Hybrid Yarns with Enhanced Bioproperties for Tissue Engineering," *Macromol. Mater. Eng.*, vol. 304, no. 7, p. 1900089, Jul. 2019, doi: 10.1002/mame.201900089.
- [151] D. Yan, "Plasma Treatment of Random and Aligned Electrospun PCL Nanofibers," *J. Med. Biol. Eng.*, vol. 33, no. 2, p. 171, 2013, doi: 10.5405/jmbe.1072.
- [152] M. M. Munir, H. Widiyandari, F. Iskandar, and K. Okuyama, "Patterned indium tin oxide nanofiber films and their electrical and optical performance," *Nanotechnology*, vol. 19, no. 37, p. 375601, Sep. 2008, doi: 10.1088/0957-4484/19/37/375601.
- [153] N. Shah Hosseini, B. Simon, T. Messaoud, N. Khenoussi, L. Schacher, and D. Adolphe, "Quantitative approaches of nanofibers organization for biomedical patterned nanofibrous scaffold by image analysis: Quantitative approaches of nanofibers organization for biomedical patterned nanofibrous scaffold by image analysis," *J. Biomed. Mater. Res. A*, vol. 106, no. 11, pp. 2963–2972, Nov. 2018, doi: 10.1002/jbm.a.36485.

- [154] E. S. Jamadi, L. Ghasemi-Mobarakeh, M. Morshed, M. Sadeghi, M. P. Prabhakaran, and S. Ramakrishna, "Synthesis of polyester urethane urea and fabrication of elastomeric nanofibrous scaffolds for myocardial regeneration," *Mater. Sci. Eng. C*, vol. 63, pp. 106–116, Jun. 2016, doi: 10.1016/j.msec.2016.02.051.
- [155] V. Sethuraman, K. Makornkaewkeyoon, A. Khalf, and S. V. Madihally, "Influence of scaffold forming techniques on stress relaxation behavior of polycaprolactone scaffolds," *J. Appl. Polym. Sci.*, p. n/a-n/a, Jun. 2013, doi: 10.1002/app.39599.
- [156] S. Ramazani and M. Karimi, "Study the molecular structure of poly(ϵ -caprolactone)/graphene oxide and graphene nanocomposite nanofibers," *J. Mech. Behav. Biomed. Mater.*, vol. 61, pp. 484–492, Aug. 2016, doi: 10.1016/j.jmbbm.2016.04.020.
- [157] N. Katsube, J. Lannutti, R. R. Duling, and R. B. Dupaix, "Mechanical Characterization of Electrospun Polycaprolactone (PCL): A Potential Scaffold for Tissue Engineering," *J. Biomech. Eng.*, vol. 130, p. 13, 2008.
- [158] J. J. L. Lee, A. Andriyana, B. C. Ang, B. Huneau, and E. Verron, "Electrospun PMMA polymer blend nanofibrous membrane: electrospinnability, surface morphology and mechanical response," *Mater. Res. Express*, vol. 5, no. 6, p. 065311, Jun. 2018, doi: 10.1088/2053-1591/aac87b.
- [159] Q.-Z. Chen, S. E. Harding, N. N. Ali, A. R. Lyon, and A. R. Boccaccini, "Biomaterials in cardiac tissue engineering: Ten years of research survey," *Mater. Sci. Eng. R Rep.*, vol. 59, no. 1–6, pp. 1–37, Feb. 2008, doi: 10.1016/j.mser.2007.08.001.
- [160] S. Lv, "Designed biomaterials to mimic the mechanical properties of muscles," vol. 465, p. 5, 2010.
- [161] B. Xu, W. D. Cook, C. Zhu, and Q. Chen, "Aligned core/shell electrospinning of poly(glycerol sebacate)/poly(L-lactic acid) with tuneable structural and mechanical properties: Aligned core/shell electrospinning of PGS/PLLA," *Polym. Int.*, vol. 65, no. 4, pp. 423–429, Apr. 2016, doi: 10.1002/pi.5071.
- [162] T. Vieira, J. Carvalho Silva, A. M. Botelho do Rego, J. P. Borges, and C. Henriques, "Electrospun biodegradable chitosan based-poly(urethane urea) scaffolds for soft tissue engineering," *Mater. Sci. Eng. C*, vol. 103, p. 109819, Oct. 2019, doi: 10.1016/j.msec.2019.109819.
- [163] C. Masri, G. Chagnon, D. Favier, H. Sartelet, and E. Girard, "Experimental characterization and constitutive modeling of the biomechanical behavior of male human urethral tissues validated by histological observations," *Biomech. Model. Mechanobiol.*, vol. 17, no. 4, pp. 939–950, Aug. 2018, doi: 10.1007/s10237-018-1003-1.
- [164] C. Alvim Valente *et al.*, "Design and optimization of biocompatible polycaprolactone/poly(L-lactic-co-glycolic acid) scaffolds with and without microgrooves for tissue engineering applications," *J. Biomed. Mater. Res. A*, vol. 106, no. 6, pp. 1522–1534, Jun. 2018, doi: 10.1002/jbm.a.36355.
- [165] K. Ragaert, L. Cardon, I. D. Baere, and J. Degrieck, "Bulk mechanical properties of thermoplastic poly- ϵ -caprolactone.," p. 6.
- [166] D. S. Rosa, I. C. Neto, M. R. Calil, A. G. Pedroso, C. P. Fonseca, and S. Neves, "Evaluation of the thermal and mechanical properties of poly(ϵ -caprolactone), low-density polyethylene, and their blends," *J. Appl. Polym. Sci.*, vol. 91, no. 6, pp. 3909–3914, Mar. 2004, doi: 10.1002/app.13596.
- [167] J. B. Rose *et al.*, "In vitro evaluation of electrospun blends of gelatin and PCL for application as a partial thickness corneal graft," *J. Biomed. Mater. Res. A*, vol. 107, no. 4, pp. 828–838, Apr. 2019, doi: 10.1002/jbm.a.36598.
- [168] M. A. Nazeer, E. Yilgor, and I. Yilgor, "Electrospun polycaprolactone/silk fibroin nanofibrous bioactive scaffolds for tissue engineering applications," *Polymer*, vol. 168, pp. 86–94, Apr. 2019, doi: 10.1016/j.polymer.2019.02.023.
- [169] M. Fadaie, E. Mirzaei, B. Geramizadeh, and Z. Asvar, "Incorporation of nanofibrillated chitosan into electrospun PCL nanofibers makes scaffolds with enhanced mechanical and biological properties," *Carbohydr. Polym.*, vol. 199, pp. 628–640, Nov. 2018, doi: 10.1016/j.carbpol.2018.07.061.

- [170] Y. Wang, W. Cui, J. Chou, S. Wen, Y. Sun, and H. Zhang, "Electrospun nanosilicates-based organic/inorganic nanofibers for potential bone tissue engineering," *Colloids Surf. B Biointerfaces*, vol. 172, pp. 90–97, Dec. 2018, doi: 10.1016/j.colsurfb.2018.08.032.
- [171] Li, Hu, and Hu, "Use of Aligned Microscale Sacrificial Fibers in Creating Biomimetic, Anisotropic Poly(glycerol sebacate) Scaffolds," *Polymers*, vol. 11, no. 9, p. 1492, Sep. 2019, doi: 10.3390/polym11091492.
- [172] D. S. Puperi *et al.*, "Electrospun Polyurethane and Hydrogel Composite Scaffolds as Biomechanical Mimics for Aortic Valve Tissue Engineering," *ACS Biomater. Sci. Eng.*, vol. 2, no. 9, pp. 1546–1558, Sep. 2016, doi: 10.1021/acsbiomaterials.6b00309.
- [173] A. P. Kishan, A. B. Robbins, S. F. Mohiuddin, M. Jiang, M. R. Moreno, and E. M. Cosgriff-Hernandez, "Fabrication of macromolecular gradients in aligned fiber scaffolds using a combination of in-line blending and air-gap electrospinning," *Acta Biomater.*, vol. 56, pp. 118–128, Jul. 2017, doi: 10.1016/j.actbio.2016.12.041.
- [174] S. Sinha-Ray, A. L. Yarin, and B. Pourdeyhimi, "Meltblown fiber mats and their tensile strength," *Polymer*, vol. 55, no. 16, pp. 4241–4247, Aug. 2014, doi: 10.1016/j.polymer.2014.05.025.
- [175] A. Ridruejo, C. González, and J. LLorca, "Micromechanisms of deformation and fracture of polypropylene nonwoven fabrics," *Int. J. Solids Struct.*, vol. 48, no. 1, pp. 153–162, Jan. 2011, doi: 10.1016/j.ijsolstr.2010.09.013.
- [176] Yazhou Wang, Guixue Wang, and Quingsong Yu, "Electrospun nanofiber meshes with tailored architectures and patterns as potential tissue-engineering scaffolds," *Biofabrication*, p. 2_3, 2009.
- [177] J. F. M. Manschot and A. J. M. Brakkee, "The measurement and modelling of the mechanical properties of human skin in vivo-II. The model," *J Biomech.*, vol. 19, no. 7, pp. 517–521, 1986.
- [178] S. K. Bhullar *et al.*, "Design and fabrication of auxetic PCL nanofiber membranes for biomedical applications," *Mater. Sci. Eng. C*, vol. 81, pp. 334–340, Dec. 2017, doi: 10.1016/j.msec.2017.08.022.
- [179] P. J. Campredon, "Contribution à l'étude des propriétés élastiques des bois," p. 38.
- [180] Y. Li and J. Barbič, "Stable Orthotropic Materials," p. 6.
- [181] S. Domaschke, A. Morel, G. Fortunato, and A. E. Ehret, "Random auxetics from buckling fibre networks," *Nat. Commun.*, vol. 10, no. 1, p. 4863, Dec. 2019, doi: 10.1038/s41467-019-12757-7.

7. List of figures

Figure 1-1: Natural tissue structures: a) Heart Muscle collagen Fibers, b) lumbar-intervertebral disk (outer and inner regions of Annulus Fibrosus) [8], c) histology slide of loose connective tissue [9]	5
Figure 1-2: a) SEM image of PCL electrospun fibers (average fiber diameter = 466 nm) [11] b) Chemical structure of Poly(ϵ -caprolactone).....	6
Figure 1-3: Publications on electrospinning from 1995 to April 2020 - Web Of Knowledge.	9
Figure 1-4: Gartner’s hype cycle of Electrospinning according to Pr. Andreas Greiner lecturer at the 6 th international conference on electrospinning - Shanghai – 2019.	10
Figure 1-5: Electrospinning set up – Taylor cone formation and whipping phase. [76]	11
Figure 1-6: Viscosity vs concentration polymer solution – [I] dilute regime ($c < c^*$), [II] semi-dilute regime, untangled ($c^* < c < c_e$), [III] semi-dilute regime, entangled ($c > c_e$), [IV] Needle clogging (highly viscous).....	13
Figure 1-7: Polyvinylpyrrolidone droplets observed at the tip of the needle in an electrospinning experiment. Zoom onto the Taylor cone formation mechanism: Surface tension of the polymer solution competing with the effects of charges on the polymeric droplets to initiate the polymer jet. [82]	14
Figure 1-8: a) & b) SEM images of electrospun polystyrene fibers. The difference of evaporation rates of the two solvents (DCM/THF) triggers a phase separation resulting in a surface pore formation [85] c) Flat ribbon fibers of Polystyrene with irregular wrinkling [86]	15
Figure 1-9: Voltage Effects on electrospinning and fiber diameter [89]	16
Figure 1-10: Formation of various jets with increasing flow rate [91]	17
Figure 1-11: a) Self assembled dimpled fibers (Yan et al.) [99] b) Schematic showing the self – assembling mechanism of the wet electrospun fibers c) Self-assembled honeycomb fibers with pore gradient (Moroni et al) [100].....	20
Figure 1-12: Electrospinning with rotating mandrel (a) and a wire drum (b) [104].....	21
Figure 1-13: Aligned fibers with Si electrodes separated by an air gap (Li et al) [109].....	22
Figure 1-14: Centrifugal electrospinning [111].....	23
Figure 1-15 - Structured PCL fibers electrospun on wire and round collectors, Vaquette et al. [113] (a) round collector, (b-c) round scaffolds, (d) wire collector (e-f) wire scaffolds.....	24
Figure 1-16: Electric field simulations with a) aluminum foil and b) metal grid (Zho et al) [115].....	25
Figure 1-17: Optical images of electrospun membrane (a) over the corresponding part of the collector designed on a printed circuit chip (b) [117]	25
Figure 1-18: a-b) Fibers collected on probe collectors [118], c) fibers electrospun on a rounded-niche collector [119]	26
Figure 1-19: 3D nanofibrous structures printed on probe arrays with non-uniform probe heights. (a,b) Convex; (c) triangle wave; (d) inverted cone; (e,f) complex curved surface. [123]	27
Figure 1-20: Influence of Voltage (a), Feeding rate (b) and conductivity (c) of the solution over the structuration. (Zhang et al) [124]	27
Figure 1-21: Electrospinning of PCL fibers onto 3D honeycomb templates: a) honeycomb collectors, b) mechanism theory of fiber deposition on conductive honeycomb templates, c) SEM image of structured PCL fibers (Nedjari et al) [125].....	28

Figure 2-1: Electrospinning set up with (a) rotating collector and (b) micro-structured collector.....	36
Figure 2-2: PCL fibers electrospun with a polymer concentration of 16wt% in DCM/MeOH (4/1) (500x (a) and 2000x magnification (b))	37
Figure 2-3: Rotating collectors: a) disk 1 (length = 2cm) and b) disk 2 (length = 25cm)	38
Figure 2-4: a) Aligned fibers collected on a metallic rotating mandrel (few seconds at 1900 rpm), b) Influence of collector size over fiber alignment (disk 1 & 2 at 1900 rpm)	39
Figure 2-5: PCL aligned fibers a) 1300 and b) 1900 rpm, c) influence of mandrel velocity on average fiber diameter, d) distribution of orientation	40
Figure 2-6: Cross section of an aligned PCL membranes (1900rpm, small disk n°1) with X500 a) and X2000 b) magnifications	41
Figure 2-7: a) Micro-structured collector with honeycomb pattern b) Cut fibrous membrane collected on honeycomb type collector	42
Figure 2-8- Micro structured collectors: a) honeycomb b) square, c) rectangular-1 and d) rectangular-2	43
Figure 2-9: a) Electrospun membrane produced on honeycomb pattern b) Honeycomb structure of fibrous scaffolds.....	44
Figure 2-10: SEM images of honeycomb scaffolds with fiber orientation and Average Fiber Diameter measurements: ① high fiber density zone (collector peaks), ② & ③ fiber bridges, ④ & ⑤ center of the honeycomb mesh.....	45
Figure 2-11: a) Optical profilometer scan of 3D honeycomb scaffolds, b) SEM image and c) profile graph of the membrane cross section	47
Figure 2-12: a) Electrospun membrane produced on square pattern b) Honeycomb structure of fibrous scaffolds.....	48
Figure 2-13 – i) SEM images of square scaffolds with ii) fiber orientation and iii) Average Fiber Diameter measurements: ① & ② high fiber density zones (collector peaks), ③ & ④ fiber bridges, ⑤ center of the mesh	50
Figure 2-14: a) Optical profilometer scan of 3D square scaffolds, b) SEM image and c) profile graph of the membrane cross section.....	51
Figure 2-15 – Other architected scaffolds produced with micros-structured collectors by electrospinning a) rectangular-1 pattern b) rectangular-2 pattern and c) honeycomb-square pattern	52
Figure 3-1: Cross section of aligned electrospun fibers cutting (a) under liquid azote (b) at ambient environment	54
Figure 3-2: SEM images of (a) square patterned scaffolds obtained by laser jet cutting device (b) melted surface of PCL polymer fibers.	54
Figure 3-3: (a) Mechanical samples extracted from cross-shaped electrospun membranes (b) mechanical sample with paper tape (c) fibrous sample held in the grips of the rheometer	55
Figure 3-4: Elementary patterns of square (a) and honeycomb (b) scaffolds with loading directions D_1 and D_2	56
Figure 3-5 – Apparatus for axial tensile tests: (a) Rheometer ARES G2 with camera control (b) MTS exceed tensile machine.....	57
Figure 3-6: Sequence of images obtained during elongation (line a) with characteristic points detection (line b).....	57

Figure 3-7: Tracking of characteristic points of honeycomb (a) and square (b) scaffolds meshes..... 58

Figure 3-8 – Thickness measurement of square patterned membrane with a compressive force test (MARS rheometer): (a) Axial force applied vs gap e between geometry and flat support, (b) and (c) square patterned membranes compressed on MARS rheometer. 59

Figure 3-9: Nominal stress of square patterned membranes a) before and b) after mass normalization 60

Figure 3-10: Global and local true axial strains of square (a) and honeycomb (b)-(c) patterned scaffolds 61

Figure 3-11: (a) Stress vs strain of PCL square scaffolds with various widths (8-20 mm or 4-10 elementary patterns), images of square patterned scaffolds ($l_0=16\text{mm}$) before (a) and under (b) applied strain of 25 %, d) Stress vs strain of honeycomb scaffolds with various widths (6 to 14 mm)..... 63

Figure 3-12: Relaxation of PCL electrospun scaffolds. Strains maintained at (a) 5 % and (b) 130 % of global true strain. Nominal stress is normalized by its highest value at $t=0$ s) 64

Figure 3-13: (a) Description of single cyclic test divided in 3 steps (b) Hysteresis curve of the first two cycles 65

Figure 3-14: Hysteresis curves of 20 cycles of square and honneycombs (D_1 and D_2) patterned scaffolds 66

Figure 3-15: Recovery ratio (a) and Resilience (b) of square, honeycombs (D_1 and D_2) patterned scaffolds..... 67

Figure 3-16: Nominal stress of raw PCL, aligned and random electrospun fibers..... 69

Figure 3-17: Nominal stress of aligned fibers (a) in longitudinal and transversal directions until 5 % of global true strain, (b) zoom in transversal direction 70

Figure 3-18: Nominal stress vs global True Strain of honeycomb PCL scaffolds. Pictures of tensile test in D_1 and D_2 directions at 0, 40 and 50 % of global true strain 71

Figure 3-19: Nominal stress of honeycomb scaffolds in function of global (dashed line) or local true strains (solid line). Pictures of D_1 and D_2 scaffolds at different global true strains..... 72

Figure 3-20: Local deformation of a single honeycomb mesh (D_1 and D_2 directions), (a) Transverse strain versus Local True Strain, (b) local relative variation of the surface 73

Figure 3-21: (a) Nominal stress vs global True Strain of squared PCL scaffolds (b) Square patterned scaffolds in longitudinal and diagonal directions..... 74

Figure 3-22: a) Nominal stress and b) Normalized nominal stress (equation 3.8) of electrospun patterned scaffolds..... 75

Figure 3-23: Local deformation of a single square mesh (longitudinal direction), (a) Transverse strain versus Local True Strain, (b) local relative variation of the surface 76

Figure 3-24: Stress-strain curves of Honeycomb scaffolds (batch B) showing no anisotropy in two loading directions D_1 and D_2 77

Figure 3-25: Optical images of honeycomb scaffolds electrospun from old PCL batch A (a) and new batch B (b) 78

Figure 4-1: Sample mechanical and cells distribution: a) tensile sample, b) quarter of tensile sample, c) patterned sample and boundary conditions 80

Figure 4-2: Design of the honeycomb cell: (a) elementary designed pattern on optical image of honeycomb scaffold, (b) design of a quarter of the honeycomb cell with allocated areas..... 81

Figure 4-3: Nominal Stress- true strain curves of aligned and random fibers (from experimental part-chapter 3) 83

Figure 4-4: Nominal stress vs True Strain of honeycomb scaffolds in D_1 direction (blue) and D_2 direction (red), dashed lines refer to the experimental data (chapter 3) and squared dots to numerical data.. 84

Figure 4-5: Deformed map of honeycomb scaffolds at 12 % of true strain (step n°19): Von Mises equivalent strains (MPa) 85

Figure 4-6: a) Deformed map (step n°4, global true strain of 2.6 %) of honeycomb scaffold, left-bottom part (center of mechanical sample) with created path (red dashed line) b) Von Mises equivalent strains along the plotted path (curvilinear abscissa S from 0 to 1.4) (steps 1 to 20) 86

Figure 4-7 : a) Nodes constructed on the initial honeycomb cell (central zone) with the defined path in yellow, b) Von Mises equivalent stresses along the path for 5 first steps of the model 86

Figure 4-8: Deformed map of honeycomb scaffolds at 3.9 % of global true strain (step n°6): Von Mises equivalent strains (MPa) a) quarter of sample, b) top and c) bottom parts d) Curves of Von Mises equivalent strains along path (steps 1 to 34) 87

Figure 4-9: Experimental and numerical results of local strain measurements: a) transverse strain evolution b) surface variation vs local true strain 88

Figure 4-10: a) Quarter of honeycomb cell with fibers orientation (arrows) in zones ② and ③, b) Definition of orthogonal axis 1, 2 and 3 for orthotropic model 89

Figure 4-11: Experimental and numerical data of Nominal Stress of honeycomb scaffolds in D_1 and D_2 direction (respectively blue and red curves). Dashed lines: experimental data (chapter 3), square dots isotropic model, empty square dots: orthotropic model. 92

Figure 4-12: Deformed map of honeycomb scaffolds (model n°2) at 3.3 % of true strain (step n°5) in direction D_1 : Von Mises equivalent strains (MPa) a) quarter of sample, b) top and c) bottom parts d) Von Mises equivalent strains along path e) Von Mises strains for model 1 and model 2 93

Figure 4-13: Deformed map of honeycomb scaffolds (model n°2) at 5.2 % of global true strain (step n°8) in direction D_2 : Von Mises equivalent strains (MPa) a) quarter of sample, b) top and c) bottom parts d) Von Mises equivalent strains along path 94

Figure 4-14: Experimental and numerical results of local strain measurements: a) transverse strain evolution b) surface variation vs local true strain. Dashed lines: experimental data (chapter 3), square dots isotropic model, empty square dots: orthotropic model 95

Figure 4-15: Anisotropy study of honeycomb scaffolds: a) deformed map of honeycomb scaffolds with central isotropic material ($E_{\text{centre}} = 1\text{MPa}$) at 3.9 % of true strain (color map: Von Mises strains) b) new geometry with variable isotropic material at the mesh center (zones ④) c) anisotropy ratio in function of E_{centre} : Young modulus of the zone ④ 96

Figure 4-16: a) Pierced honeycomb membranes (thermal post-treatment) b) nominal stress curves of unpierced (green line) and pierced membranes in D_1 and D_2 direction (blue and red lines) 97

Figure 4-17: a) New geometry model with secondary bridges (zones ④) b) anisotropy ratio is function of implemented thickness of central areas (zones ④) 98

Figure 4-18: Design of the square cell in D_1 direction: (a) elementary designed pattern on optical image of square scaffold, (b) design of a quarter of the square cell with allocated area 99

Figure 4-19: Design of the square cell in D_2 direction: (a) elementary designed pattern on optical image of square scaffold, (b) design of a quarter of the square cell with allocated areas 100

Figure 4-20: Experimental and numerical results of Nominal stress-strain curves of square patterned scaffolds in directions D_1 and D_2 (respectively blue and orange dots) 101

Figure 4-21: a) Deformed map of Square scaffolds at 3.9 % of global true strain (step n°6): Von Mises equivalent strains (MPa), enlarged images of b) top and c) bottom of structure d) Von Mises equivalent strains along plotted path (curvi linear abscissa from 0 to 2.1) 102

Figure 4-22: a) Deformed map of Square scaffolds at 3.9 % of global true strain (step n°6) in direction D_2 : Von Mises equivalent strains (MPa), enlarged images of b) top and c) bottom of structure d) Von Mises equivalent strains along plotted path (curvi linear abscissa from 0 to 2.1) 103

Figure 4-23: a) New square cell geometry without secondary bridges (zones ④), b) quarter sized structure (new geometry) oriented in D_2 loading direction. C) Experimental and numerical results of Nominal stress-strain curves of square patterned scaffolds in directions D_1 and D_2 104

Figure 4-24: *Experimental and numerical results of local strain measurements- square patterned scaffolds: a) transverse strain evolution b) surface relative variation vs local true strain.* 105

8. List of tables

Table 1-1: Main publications on electrospun PCL scaffolds for tissue engineering applications published in 2019.....	9
Table 1-2: Effects of electrospinning parameters on fiber morphology (inspired from Sill et al.) [98]	18
Table 1-3: Young moduli of human tissues measuring by tensile stretching [131], [132].....	29
Table 1-4: Mechanical properties of structured electrospun scaffolds [137]–[141]	33
<i>Table 3-1: Expressions of global true strain and local axial true strains for square, honeycomb D_1 and honeycomb D_2 scaffolds.....</i>	<i>61</i>
<i>Table 3-2: Relaxation times of electrospun patterned membranes</i>	<i>64</i>
Table 4-1: Global true strain values of numerical steps.....	80
Table 4-2: Five free parameters of orthotropic and transversely isotropic material (aligned fibers liked material)	91
Table 4-3: Material properties of orthotropic zones	91